2007

# Application and modeling of TiO2-supported gold nanoparticles for CO preferential oxidation in excess hydrogen

Benjamin Alan Grayson
*University of South Florida*

Application and Modeling of TiO$_2$-Supported Gold Nanoparticles for the Preferential

Oxidation of Carbon Monoxide in Excess Hydrogen

by

Benjamin Alan Grayson

A dissertation submitted in partial fulfillment
of the requirements for the degree of
Doctor of Philosophy
Department of Chemical Engineering
College of Engineering
University of South Florida

Major Professor:  John T. Wolan, Ph.D.
Stephen E. Saddow, Ph.D.
Elias Stefanakos, Ph.D., P.E.
Aydin K. Sunol, Ph.D.
George S. Nolas, Ph.D.

Date of Approval:
June 4, 2007

Keywords:  Supported Au/TiO$_2$, Kinetic Modeling, Catalysis, World Gold Council, FTIR

ACKNOWLEDGEMENTS

To all of my advisors, colleagues, friends and family, thank you for your support. I could not have done this without you.

TABLE OF CONTENTS

LIST OF TABLES

LIST OF FIGURES

APPLICATION AND MODELING OF $TiO_2$-SUPPORTED GOLD NANOPARTICLES FOR THE PREFERENTIAL OXIDATION OF CARBON MONOXIDE IN EXCESS HYDROGEN

Benjamin Alan Grayson

ABSTRACT

This work begins with a brief overview of heterogeneous, characterization techniques, and current hypotheses about gold mechanisms. This is followed by the initial characterization of custom two-phase-method gold nanoparticles provided by the Interfacial Phenomena and Polymeric Materials research group at USF, the anatase $TiO_2$ support and reference $Au/TiO_2$ catalyst provided by the World Gold Council.

In order to verify the ability of the two-phase-method GNP catalyst provided to oxidize CO in excess hydrogen, it was necessary to develop an effluent testing protocol. The first experiments involved 24 hour runs to observe catalyst deactivation. Concerns over cycling effects observed in the absorbance integral calculations lead to the introduction of a reference gas. Corrections were made to the carbon monoxide absorbance integral calculations which allowed the direct comparison of results. These corrections included baseline adjustments for each species and $N_2$ purging to eliminate background $CO_2$ and $H_2O$ contamination. After these improvements, the two phase method GNP catalyst CO oxidation ability was investigated. Unfortunately, the supplied two phase method gold catalyst has been unresponsive for CO oxidation applications. One hypothesis for the problems is that the surfactants used to keep the gold nanoparticles from aggregating are preventing carbon monoxide transport to the surface of the particle. Another theory is that the gold may not be adhering to the surface of the $TiO_2$ creating a cohesive metal/support interaction.

The kinetics of CO preferential oxidation (PROX) catalyzed by the World Gold Council's nano-Au/TiO$_2$ was studied to evaluate elementary and nonelementary empirical rate expressions. Information is readily available for CO fractional conversion for this catalyst below 0$^o$C. However, a comprehensive CO PROX kinetic model in which three reactions (CO oxidation, H$_2$ oxidation and the water gas shift reaction) occur simultaneously is lacking. The reaction was carried out in a vertical packed bed micro-reactor testing unit; temperature was varied between 25 and 125$^o$C, and a range of feed rates were tested. In-situ Fourier transform infrared spectroscopy (FTIR) reaction data was analyzed; pre-exponential and activation energies are calculated for each kinetic model. Empirical rate expressions based on power law models were used to fit the experimental data. The reversible water gas shift reaction was found to play an important role when fitting the experimental data precisely and explained the selectivity decrease at higher reaction temperatures. The empirical kinetic model presented will be useful to simulate PROX operation parameters for many applications.

# 1 INTRODUCTION AND THEORY

## 1.1 Introduction to Catalysis

In a chemical reaction, there are five basic parameters one can control: temperature, pressure, concentration of species, contact time and pattern.[1] While early attempts at improving reaction rates and conversions were successful by relying on high temperature and high pressure processes, these conditions are energy intensive, corrosive, and result in undesirable side products.[1] These issue ushered in the development of catalytic systems. To date, approximately 90% of all industrial processes are catalyzed in some fashion. The extensive use of selective catalysts along with improvements in fluid flow characteristics have led to lower operating temperatures, lower operating pressures, higher efficiencies and cost reduction. The majority of these selective catalysts falling into two broad categories: heterogeneous and homogeneous.[1] The difference being that heterogeneous reactions occur between at least two different phases while homogeneous reactions all occur in the same phase. This work will primarily focus on the heterogeneous reactions occurring between a gas phase influent and a solid phase nano-catalyst.

One of the most basic definitions of a catalyst is "a material that enhances the rate and selectivity of a chemical reaction and in the process is cyclically regenerated."[1] This is a valid definition; however, it fails to describe the subtleties of the catalytic process. Figure 1.1 attempts to graphically explain some of the details of an elementary heterogeneous reaction. One of the processes by which a catalyst increases the reaction rate is through the lowering of the activation energy (or energy barrier) to the formation of products. The typical mechanism for heterogeneous catalysis starts with incoming reacting compounds adsorbing onto the surface of a solid catalyst (Figure 1.2 and Figure 1.3).[1] This process must be energetically profitable for both species or it will not occur.

Figure 1.1 demonstrates that the chemisorbed species do lower their energy states when adsorbing onto the surface. These adsorbed species are then rapidly and selectively transformed into adsorbed products (Figure 1.4 and Figure 1.5).[1] Although one can see that the energy barrier for this catalyzed reaction is substantially lowered, one subtlety expressed in Figure 1.1 is that the apex of the catalyzed energy barrier is before the apex of the uncatalyzed reaction. If the reaction path can be assumed to be an approximation of the time needed for the reaction to occur, this difference in reaction time can result in a catalyzed reaction occurring several orders of magnitude quicker. The products then desorb from the surface returning the solid catalyst back to its original state to recycle the process (Figure 1.6 and Figure 1.7).[1] These interactions provide a chemical "shortcut" in which reactants are converted to products more rapidly and at much milder conditions than if no surface interactions occurred.[1] Additionally, catalysts can perform many other tasks. Just a few are listed below.[2]

- Help initiate reactions
- Stabilize the intermediates of a reaction
- Hold reactants in close proximity or in the correct orientation
- Block side reactions
- Stretch bonds or make bonds easier to break
- Donate or accept electrons
- Act as an efficient means for energy transfer

1.2  Catalytic Applications of Gold

The first indication that gold might be a useful catalyst came through the work of Haruta et al. when he discovered in the late 1980s that gold becomes considerably stickier when spread in tiny dots on certain metal and oxide compounds.[3] Since then, his research has led to a renewed interest in gold applications previously unexplored. Many groups now report numerous applications for gold nanoparticles with the optimum gold particle sizes ranging from 2-50 nm depending on the application.[4-6] Several examples for which gold nanoparticles demonstrate catalytic activity are listed below.[7]

- Oxidation of CO and hydrocarbons

- Water gas shift (WGS)

- Reduction of NO with propene, CO or $H_2$

- Reactions with halogenated compounds

- Removal of CO from hydrogen streams

- Hydrochlorination of ethyne

- Selective oxidation, e.g. epoxidation of olefins

- Selective hydrogenation

- Hydrogenation of CO and $CO_2$

This work will be focusing on the extreme ability of gold nanoparticles to oxidize carbon monoxide at low temperatures and determine any potential applications for proton exchange membrane fuel cells (PEMFCs).
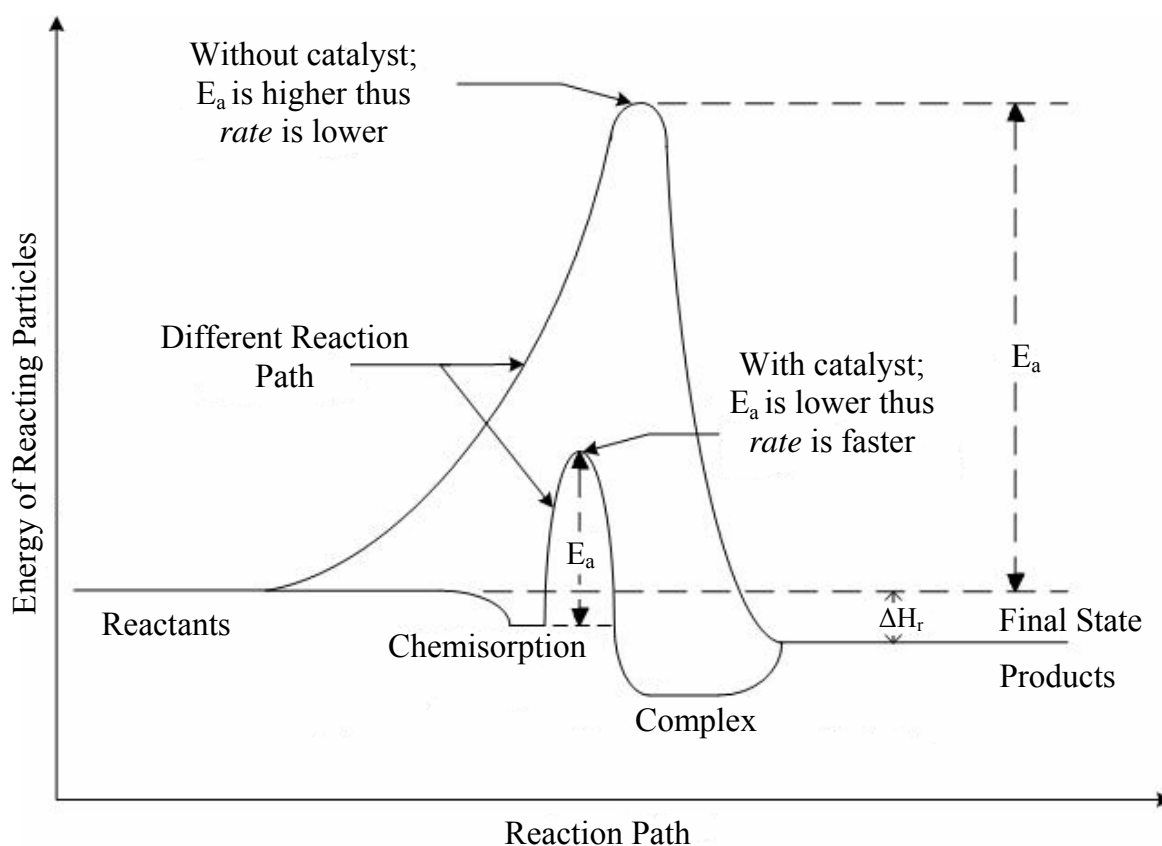


Figure 1.1 Catalytic and noncatalytic potential energies versus reaction coordinates for an elementary reaction.
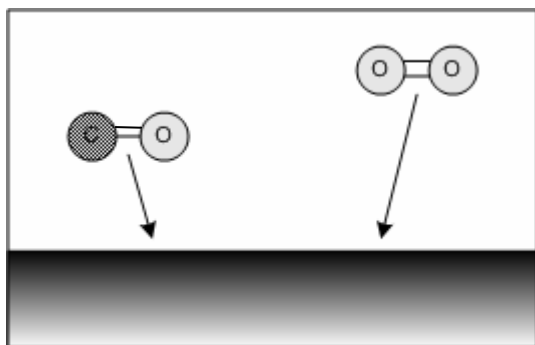
Figure 1.2  Carbon monoxide and Oxygen diffusing to the catalyst surface.
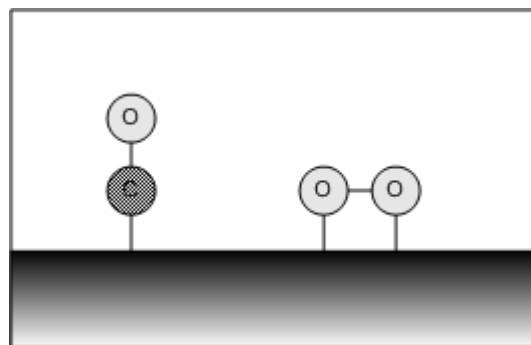


Figure 1.3  Both molecules adsorb to the surface.
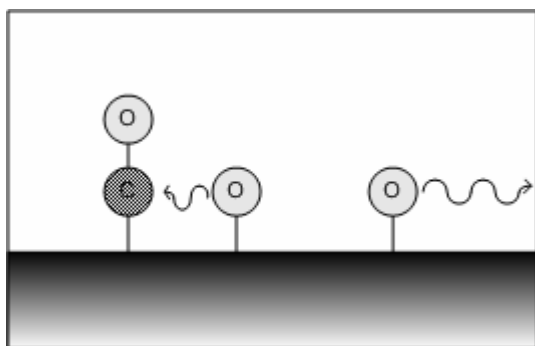


Figure 1.4  Oxygen radicals diffuse quickly along the surface.
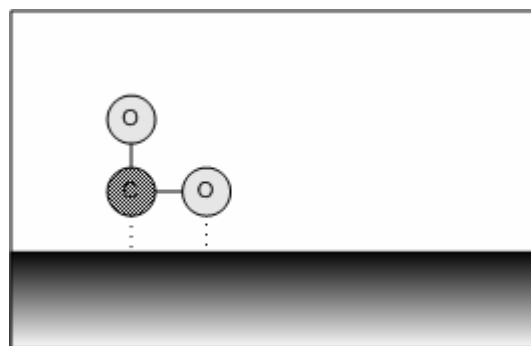


Figure 1.5  Carbon monoxide and the oxygen radical react to form carbon dioxide.
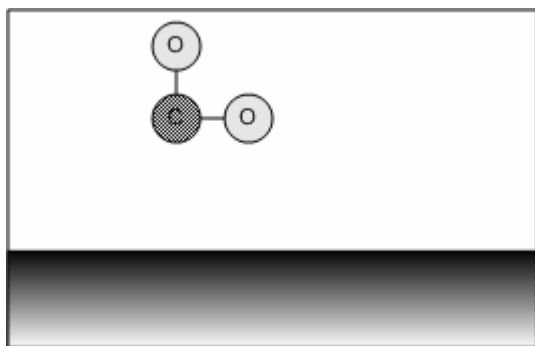


Figure 1.6  After the reaction, the carbon dioxide molecule desorbs.
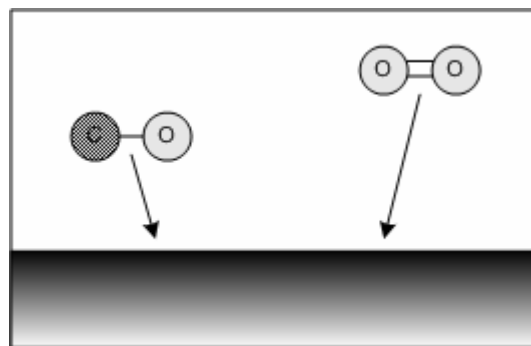


Figure 1.7  The catalyst surface returns to its original active state enabling the process continue.

In many fuel cell systems, the influent hydrogen is produced through hydrocarbon reformation, and as a result of the reforming process, a small amount of carbon monoxide is typically present in the product stream.[8]  This is a major concern in the direct hydrogen

PEMFC industry due to the prevalence of platinum based catalysts and the potential of poisoning due to CO. The Department of Energy is focusing on improvements regarding the tolerance of PEM membrane assemblies but reducing the CO influent concentration would be preferred.[9] The Department of Energy 2011 technical target for CO tolerance of stationary PEM fuel stack systems (5-250 kW) operating on reformate to be 500 ppm at steady state and 1000 ppm transient; the current status (c. 2005) is 50 ppm at steady state and 100 ppm transient.[9] Several solutions to the problem include the development of alternative catalyst systems more tolerant to CO poisoning, increasing the operating temperature to increase the catalyst kinetics, and introducing catalyst additives to oxidize the CO.[8] A breakdown of the typical formulation components of CO selective oxidation catalysts are shown in Figure 1.8. Increasing the operating temperature is beneficial because fuel cells which operate at higher temperatures, i.e. above $200^{\circ}C$, are better equipped to deal with the CO issue, because CO does not readily adsorb to the anode at these elevated temperatures; however, hydrogen based PEM fuel cells normally operate at $80^{\circ}C$ though DOE's target for $H_2$-PEMFCs by 2010 is to operate at $120^{\circ}C$.[7] The temperature limitations of PEM fuels are due to the necessity of Nafion$^{TM}$ to remain hydrated (~40% relative humidity) in order to maintain proton conductivity.[10] Within the Nafion$^{TM}$ film exist nanometer size pores lined with sulfonic acid groups ($SO_3^-H^+$, and in the presence of water, these groups form hydronium ions that can only transport in the liquid phase.[10] It is found that Nafion$^{TM}$ exhibits proton conductivity similar to liquid electrolytes but only when hydrated with water.[10] When the PEM operating temperature exceeds $100^{\circ}C$, the Nafion$^{TM}$ begins to dehydrate and the proton conductivity drops.
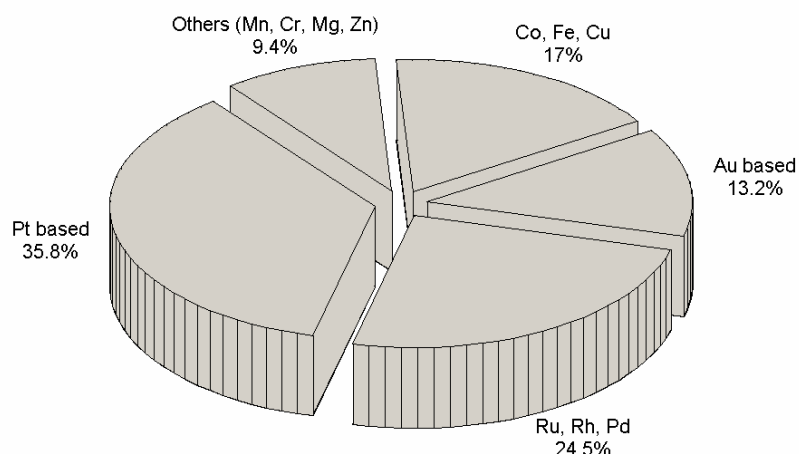
Figure 1.8  Typical formulation of CO selective oxidation catalysts.[8]

1.3    Synthesis Techniques of Au Nanoparticles and the Necessity of a Reference

Various methods have been employed to synthesize supported gold nanoparticle (GNP) catalysts including deposition-precipitation, impregnation, sol-gel techniques, coprecipitation, incipient wetness, metal organic-chemical vapor deposition, and dip-coating.[11]  Although there are literally dozens of methods of preparation, essentially all of these techniques can be reduced to three major procedures.[12]  In the first procedure, a gold metal precursor is mixed with a support to give a system that, after controlled calcination, produces gold/support catalysts.[12]  The metal nanoparticle's size is controlled by the calcination temperature and experimental results have shown that lower temperatures seem to favor the formation of smaller particles.[12]  Secondly, a gold precursor is deposited or grafted onto the surface of the support, which has been pre-formed from the gas or from the liquid phase, and subsequently thermally decomposed to give the gold/support catalysts.[12]  Lastly, the gold nanoparticles are pre-produced in a given solution where they are stabilized by soluble polymers or by kinetic conditions, and subsequently left to be adsorbed by the surface of the desired support particles.[12]

Preparation procedures developed by laboratories vary greatly and the effects of aging, stirring, washing, order in which reactants are added, temperature, concentration of reactants, and calcining conditions all appear to be important parameters to monitor.[4]

6

With this in mind, the World Gold Council (WGC) in 2002 commissioned four gold reference catalysts enabling researchers to benchmark their own catalyst systems against a common reference. These consist of three proprietary reference catalysts of nano-gold on metal oxide supports made by Süd Chemie, Japan under the supervision of Haruta et al., with characterization at AIST, Japan.[7,13] A fourth reference catalyst of gold on carbon is produced by Rossi et al. of the University of Milan.[7,13] Descriptions of the four catalysts are listed below. The choice of supports for each catalyst application is very important and will be discussed in Section 1.5.2.

World Gold Council Reference Gold Catalysts[7]

- A - 1.5 wt% $Au/TiO_2$ (P-25) as powder by deposition precipitation
- B - 0.3 wt% $Au/Fe_2O_3/Al_2O_3$ as beads by deposition precipitation
- C - 5 wt% $Au/Fe_2O_3$ as powder by co-precipitation
- D - 10 wt% Au/C (Cabot XC72R) as powder using gold sol.

1.4 Reactor Setup

The FTIR/reactor setup is shown in Figure 1.9 and Figure 1.10. All reactions were performed in a quartz tubular reactor, 24 inches in length, 4 mm ID which constricts to 2 mm ID at the midpoint, inside of a Lindberg/Blue split tubular furnace. One hundred milligrams of nano-Au/TiO2 was packed loosely between high temperature quartz wool to prevent the powder from escaping. Two ball valves placed before and after the reactor tube allows for the influent stream to bypass the catalyst bed completely to comprise a reference unreacted sample. The input stream is modeled after a typical single stack PEMFC inlet feed stream with CO contamination. Three mass flow controllers (MFCs) lead to a mixing tube to assure a consistent inlet gas concentration. The setup allows for injection points before and after the test bed in order to analyze the inlet and effluent of the process in the gas chromatograph. Also, a bypass is incorporated to send just the feed stream through to the effluent. After exiting the reactor system, the effluent is fed directly to the inline Fourier transform infrared spectrometer gas cell for real time compositional analysis.
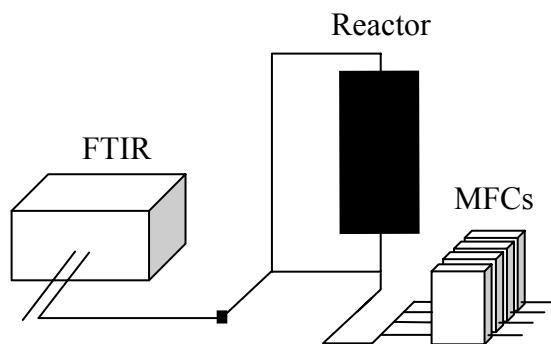
Figure 1.9  FTIR/Microreactor setup.
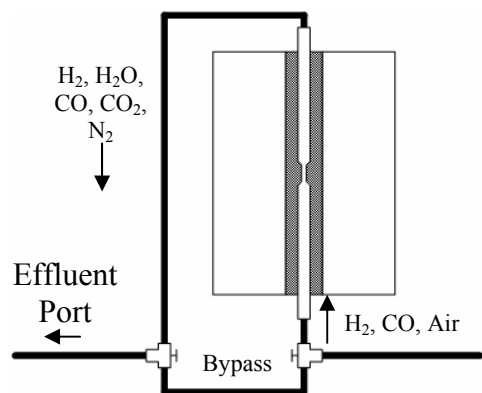


Figure 1.10  Microreactor setup.

## 1.5    Characterization Techniques

The main characterization techniques for these experiments will be X-ray photoelectron spectroscopy, X-ray diffraction, Fourier transform infrared spectroscopy, and gas chromatography.   A brief overview of each technique and its application to this work follows.

### 1.5.1   X-ray Photoelectron Spectroscopy (XPS)

XPS spectra collected will attempt to determine the oxidation states of the Au nanoparticles and identify the catalyst's elemental surface atomic concentrations to examine changes during calcination and after reaction.  All XPS analyses were conducted in a Perkin-Elmer PHI 560 ESCA/SAM System (base pressure - 5 x $10^{-10}$ Torr) equipped with a PHI 04-500 Dual Anode X-ray source and a 25-270AR cylindrical mirror analyzer.   All spectra were measured in normal emission using Mg $K_{\alpha}$ radiation. The spectrometer was calibrated to yield the standard Au $4f_{7/2}$ and Cu $2p_{3/2}$ lines at 84.00 eV and 932.66 eV, respectively.  XPS will be used to determine elemental and chemical state information of near-surface species.

X-ray Photoelectron Spectroscopy is a relatively non-destructive technique that exposes the sample to ultra high vacuum pressures with base pressures of 1 x $10^{-10}$ Torr, increases the temperature by approximately 10-20$^{\circ}$C, and exposes the sample to soft X-rays between approximately 1000-1500 eV.  These conditions are considered nondestructive

8

for most materials and systems with few exceptions. Due to the ultrahigh vacuum (UHV) requirements, samples that are run in the XPS system must have relatively low vapor pressures; hence, they must be solids. Typical examples of solids analyzed are metals, glasses, semiconductors, and low vapor pressure ceramics. Ideally all samples should be free of fingerprints, oils, and other surface contamination. Furthermore, XPS is a beneficial technique when destructive techniques must be avoided [14]. The sensitivity of the technique is about 0.1~1.0 atomic percent. The approximate sampling depth is material dependent but averages about 3 nanometers, and the energy resolution is about 0.3 to 4 eV [15]. One drawback of working with XPS is the time required to run a sample. A sample placed in the vacuum chamber requires several hours in order to pump down before analysis. Qualitative analysis can be performed in 5 to 10 minutes. Quantitative analysis requires 1 hour to several hours depending on the information desired [16].

### 1.5.2   X-ray Diffraction (XRD)

The XRD will be used to determine the crystalline state of the $TiO_2$ dioxide before and after calcination. These results will verify any changes in crystal structure due to typical calcination temperatures.

X-ray diffraction is a versatile, non-destructive analytical technique for identification and quantitative determination of the various crystalline forms of compounds present in powdered and solid samples.[17] XRD starts with a generated X-ray focused onto a sample. When the X-ray beam hits an atom, the electrons around that atom oscillate with the same frequency as the incoming beam. X-rays are then generated; however, most of the waves destructively combine and result in no resultant energy leaving the sample. In a relatively few specific directions within a crystalline solid, the X-rays will combine constructively and produce a diffracted X-ray out of the sample. Using Bragg's Law and the relationships for interplanar spacing, one can predict the diffraction angles in which X-rays should constructively combine.[17,18] Identification is usually achieved by comparing the X-ray diffraction pattern, or diffractogram, obtained from an unknown sample with a database containing reference patterns. X-ray diffraction (XRD) was

performed using a Panalytical X'Pert Diffractometer, tension 45 kV, current 40 mA, and Cu K$_\alpha$ radiation.

### 1.5.3 Fourier Transform Infrared Spectroscopy (FTIR)

All experiments were performed using a Bio-Rad Excalibur Series FTS 3000 system. From the FTIR analysis of the effluent data, individual component conversions can be calculated at each temperature and gas flow rate. The gas cell specifications are given in Table 1.1. The detector used for all experiments is mercury cadmium telluride (MCT).

Table 1.1  FTIR gas cell specifications.

| | |
|---|---|
| Model Number: | 2.4-PA          (Ultra-mini Cell) |
| Pathlength: | 2.4 meters |
| Body material: | Borosilicate glass |
| Mirror coating: | Protected gold |
| Body dimensions: | Length, 11.5 cm.; I.D., 3.3 cm. |
| Volume: | 0.1 liter |
| Transfer mirrors: | Two plane mirrors on mounts for finger grip adjustment. |
| Valves: | Two stainless steel plug valves |

Fourier Transform Infrared spectroscopy examines the effects of electromagnetic radiation on solids, liquids, and gases.[17,18] When the infrared radiation passes through the samples, characteristic frequencies are absorbed that cause molecular vibrations to occur. The transmitted light which passes to the detector allows for the determination of composition through the calculation of transmittance and absorbance spectra.[17,18] Transmittance is defined as the ratio of intensity of transmitted radiation through the sample versus the intensity of incident radiation, i.e. the background transmittance with no sample.[17,18]  Absorbance is defined as the logarithm, base 10, of the inverse transmittance and is proportional to molar concentration.[17,18] Absorption band intensities, widths, and areas are all dependent on both temperature and pressure.[19] Recommendations in the Digilab manual suggest running gas samples at atmospheric pressure to minimize pressure broadening and allowed to reach thermal equilibrium before collecting spectral data.[19] Another problem with gas cells is selective adsorption of species onto the cell walls which can alter quantitative results.[19] Flushing the system several times prior to running is necessary to clean the lines and erase cell "memory".[19]

The main component of the FTIR spectrometer is an interferometer which splits and recombines a beam of light such that the recombined beam produces a wavelength-dependent interference pattern or an interferogram.[20]  When radiation with more than a single wavelength hits the interferometer, the output signal is the sum of all the cosine waves of the entering radiation.[20]  Even though the interferogram contains the basic information on frequencies and intensities characteristic of a spectrum in the time domain, the output is in a form that is not easily understood.[20]  Typically, a spectrum is converted from the time dependent interferogram to the frequency domain by computing the cosine Fourier transform of the signal.[20]

Calculations of absorbance use the Beer-Lambert law which is shown in Eqns. 1.1-2, which states that there is a logarithmic dependence of the light transmitted through a substance and its concentration.[21]

Transmittance $T = I/I_o$  (1.1)

Absorbance $A = \log(1/T) = \log(I_o/I) = ecL$  (1.2)

$I_o$ = Intensity of incident radiation, I = Intensity of transmitted radiation, e = molar extinction coefficient, c = concentration (mole/liter), L = sample pathlength (cm)

### 1.5.3.1   Aabspec In-situ FTIR Micro-reactor

A specialized cell mounted within the FTIR allows for additional IR analysis of solid samples and allows one to discriminate between surface gold sites according to their oxidation state.[22]  Since IR absorbance area is linearly proportional to the concentration of the species, one can calculate the integral of the absorbance and correlate that integral to the concentration of the species.[18]

The Aabspec cell structure (      Figure 1.11) consists of three parts: the body containing access ports for reactive gases, a sample probe containing a heating system, and a matched end plate designed specifically for each probe.[23]  This allows for the three

11

modes of operation, as shown in Figure 1.12, Figure 1.13, and Figure 1.14: transmission

mode, specular reflectance mode, and large angle infrared reflectance (LARI) mode.[23]
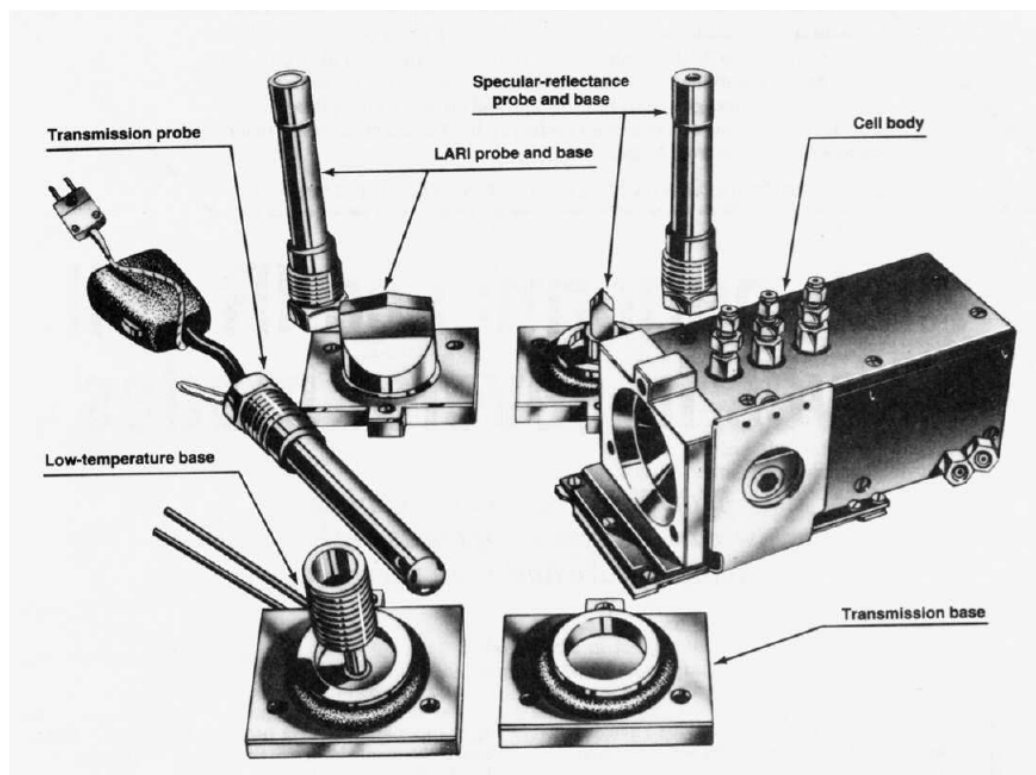


Figure 1.11  Aabspec microreactor for in situ FTIR analysis of solid samples.[23]
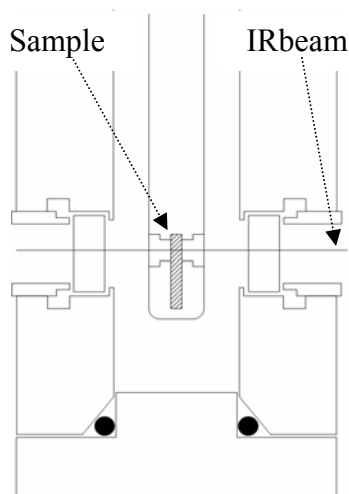


Figure 1.12  In transmission mode, the cell looks like a standard unit modified for high temperature high pressure IR analysis.
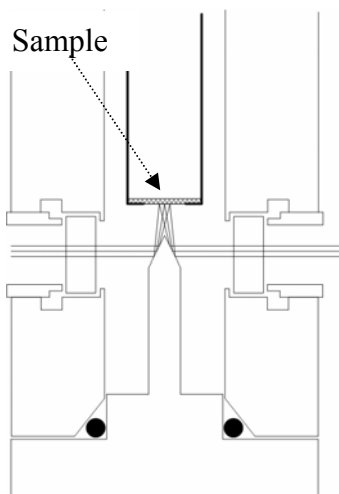
Figure 1.13  For specular reflectance IR determinations, the angle of incidence is nearly normal.
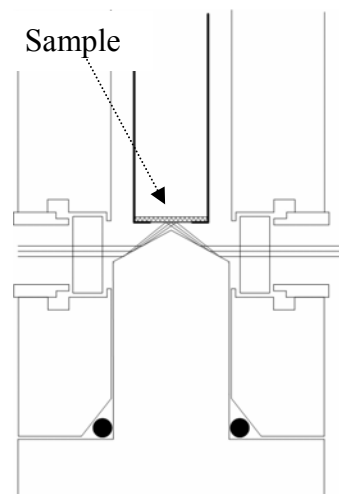
Figure 1.14  For large angle reflectance IR, the incidence angle is near grazing.

12

In transmission mode, the sample is mounted perpendicular to the optical axis of the infrared beam and the beam passes directly through the sample mount.[23] The matched endplate is unnecessary and is used only to close the end of the cell body.[23] However, some applications allow for liquid cooling through the endplate for low temperature studies.[23] In specular reflectance mode, the IR beam strikes the sample nearly perpendicular to the surface of the sample with a typical angle of incidence near 10 degrees.[23] A gold mirror mounted on the end plate reflects the entering beam so that it continues along the optical axis. In LARI mode, the IR beam strikes at a glancing angle of approximately 20 degrees.[23] Once again, gold mirrors on the end plates reflect the IR beam to continue its optical axis path.[23] The LARI mode samples can be mounted vertically or horizontally.[23] Horizontal mounting allows for samples which may melt during analysis at elevated temperatures, liquid samples, or powders.[23]

1.5.4   Gas Chromatography (GC)

All experiments were performed with an Agilent Technologies 6890N network GC system with Chemstations software. Standard GC operating conditions are shown in Table 1.2. The GC will be used to verify the effluent concentrations from the oxidation reaction along with the FTIR.[24] Gas chromatography uses a thin capillary column to separate injected samples into its primary components through adsorption onto the column walls or onto the packing materials in the column.[24] The velocity of the species progressing through the column is a function of the strength of adsorption, which in turn depends on the type of molecule and on the column materials which in turn forces each of the species to exit at different times.[24] The outlet gases on then detected and the signal strength and time are noted to identify molecules and concentration.[24]

Table 1.2  GC operating parameters.

| GC Operating Parameters | |
|---|---|
| Oven: | 30$^{\circ}$C for 10 minutes |
| Front Inlet: | Mode: Split |
| | Initial Temperature 200$^{\circ}$C |
| | Pressure: 20 psi |
| | Split Ratio: 14.568:1 |
| | Split Flow: 67.1 mL/min |
| | Total Flow: 74.2 mL/min |
| | Gas Type: Helium |
| Column: | Capillary Column |
| | Model Number: Varian CP7534 |
| | Plot Fused Molsieve Column |
| | Nominal Length: 30 m |
| | Nominal Diameter: 320 μm |
| | Nominal Film Thickness: 10 μm |
| | Mode: Constant Pressure |
| | Pressure: 20 psi |
| | Nominal Initial Flow: 4.6 mL/min |
| | Average Velocity: 62 cm/sec |
| Detector (TCD) | Temperature: 250$^{\circ}$C |
| | Reference Flow: 20 mL/min |
| | Mode: Constant column + makeup flow |
| | Combined flow: 7.0 mL/min |
| | Makeup flow: On |
| | Makeup Gas Type: Helium |
| | Filament: On |
| | Negative Polarity: Off |

Temperature must be closely monitored as both molecular adsorption and the rate of progression along the column are temperature dependent.[24]  Although lower temperatures produce the greatest level of separation, the progression time to the outlet of the column is greatly increased and can be prohibitive.  Temperature programs which modify the oven temperature try to compromise between various species to be analyzed between lower temperatures to separate and higher temperatures that promote shorter analysis times.[24]  Ideally, hydrogen would be carrier gas used for most GC experiments because it provides the best component separation.[24]  However, helium is the most common choice due it being nonflammable, shares similar properties to hydrogen, and is compatible with most detectors.[24]  The two most common types of detectors for GC are thermal

conductivity detectors (TCD) and flame ionization detectors (FID).[24] Thermal conductivity detectors are useful in that they can detect any component other than the carrier gas injected.[24] Flame ionization detectors are primary used to detect hydrocarbons.[24]

### 1.5.5 Thermogravimetric Analysis

Thermogravimetric Analysis (TGA) is a thermal analysis technique used to measure changes in the weight (mass) of a sample as a function of temperature and/or time. Examples of uses are the determination of polymer degradation temperatures, absorbed moisture content, and inorganic filler in composite materials.[25] Analysis of the samples starts by placing a tared sample into a microbalance assembly located in a high temperature furnace. After determining the initial weight at room temperature, the sample is subsequently heated while the weight is constantly monitored. A weight profile is then generated for amount or percent weight loss at any given temperature.[25] The TGA will be used to determine the temperatures at which each component of the Brust gold catalyst evaporates. This information is useful when determining at which temperature the catalyst becomes stable and if any adjustments to the calcination temperature are necessary.

### 1.6 Discussion of Possible Reaction Mechanisms and the Reactive Species of Gold

### 1.6.1 Introduction

There are many factors to consider when one begins to work with catalytic materials. First of all, the process of picking a catalyst to promote a reaction is not well understood, therefore extensive trial and error is part of optimization.[26] In addition, reproducing the chemical composition of a catalyst does not guarantee the reproduction of the catalytic activity.[26] Also, the crystalline structure of the catalyst are just as if not more important than the composition[26] As discussed in Chapter 1.1, catalysts reduce the energy barriers to form products; however, they cannot shift the equilibrium of a reaction which are governed by thermodynamics alone.[26] All of these factors are necessary to note when beginning catalysis work.

Accordingly, the difficulty of finding a mechanism which fully characterizes the catalyst system is that the favored mechanism must fit the data is such a way that all other mechanism possibilities can be rejected.[26] For each rate controlling mechanism, there are usually three to seven parameters which must be fitted, verified, and precisely reproduced.[26] Thus, it is difficult if not impossible to justify precisely a correct mechanism for a particular process.[26] This means that the inherently that most proposed analytical mechanisms can only claim to be "approximate" calculations of each system under specific conditions.[26] With the fundamental understanding that a proposed mechanism can only be approximated, one should try to find the simplest equation which adequately describes their system.[26] When analyzing the PROX reaction catalyzed by GNPs/TiO$_2$, the three most important reactions are the oxidation of carbon monoxide, the oxidation of hydrogen, and the water gas shift reaction (Eqns. 1.3, 1.4, 1.5) and attempts to model these reactions are discussed in Chapter 4.

$$CO + \frac{1}{2}O_2 \rightarrow CO_2 \qquad\qquad \Delta H^o{}_{298} = \text{-283 kJ/mol} \qquad\qquad (1.3)$$

$$H_2 + \frac{1}{2}O_2 \rightarrow H_2O \qquad\qquad \Delta H^o{}_{298} = \text{-242 kJ/mol} \qquad\qquad (1.4)$$

$$H_2O + CO \leftrightarrow CO_2 + H_2 \qquad\qquad \Delta H^o{}_{298} = \text{-41.1 kJ/mol} \qquad\qquad (1.5)$$

### 1.6.2 Theories for the Reaction Mechanism of CO Oxidation on Supported Gold Nanoparticles

Some of the reasons put forth for the ability of nano-gold to be an active catalyst are the interactions between the metal and support, the coordinative unsaturation of the surface atoms, and quantum size effects.[27] So, in order to fully comprehend the entire system, it is necessary to begin with an examination of particle size effects and the interactions of molecules with the Au nanoparticles and the support.[28]

Models for these GNP/support interactions can be categorized into three basic types: perimeter, surface, and intermediate as presented in Figure 1.15.[29] Surface models

propose that the oxygen molecules dissociate directly on the surface of the gold particles with the supporting material having little to no effect on the reaction mechanism.[29] Intermediate and perimeter models imply that the only active areas of the system are the metal-support interfaces.[29] The main difference in these two models is whether or not the CO molecule interacts with a $O_2$ molecule or a O· radical.[29]   As shown in both of these models, it is important to note that the interface density on the surface would drastically increase with decreasing particle size thus increasing the active sites for CO oxidation.[30] The increase in catalytic activity with decreasing particle size is consistent with reported observations, and intermediate and perimeter models are the more likely mechanism for reducible metal oxide supported GNP catalysts.[30]
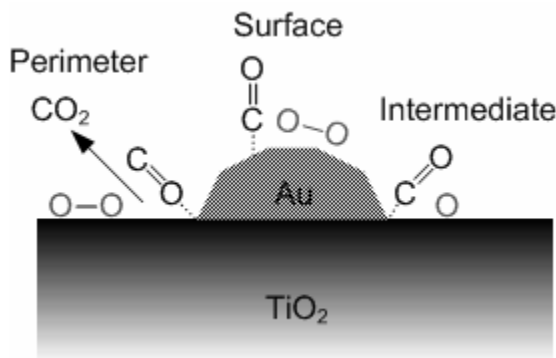


Figure 1.15  Possible reaction mechanisms for the oxidation of carbon monoxide in a Au/TiO$_2$ system.[29,31]

Along with the possibility of providing a oxygen source to the Au-CO oxidation reaction, the support introduces a defect structure which aids in the formation and stabilization of small gold particles and promotes active edge sites.[32] Mavrikakis et al. found that carbon monoxide (CO) was able to bind to the off-axis faces of gold where the presence of steps may be the most significant contributing factor to the attraction.[27] Density functional theory calculations indicate that CO may only chemisorb on the low-coordinated Au atoms such as those found in the steps and kinks on the edges of the atom, and not on the regular (111) terraces.[27] Therefore, smaller particle sizes may greatly increase the "steps and kinks" density within the catalyst.[27]

17

The choices for nano-Au support materials can be divided into two broad categories: irreducible and reducible supports. A few catalyst supports that have been investigated include oxides of cobalt, magnesium, iron, aluminum, ceria, nickel, titanium, and tin with the most commonly used supports for gold catalysts being titania, zirconia, silica, and alumina.[11] It has been found that there is a significant division between the activities of irreducible oxide supports, such as $Al_2O_3$, and reducible transition metals oxides, such as $TiO_2$. When the reducible metals are coupled with gold, the catalytic activity of the system can be up to one order of magnitude higher than the same Au on irreducible supports.[30] In addition, reducible supports are more tolerant to increased gold particle size while still maintaining a reasonable level of activity.[30] A study comparing $Au/TiO_2$, $Au/Fe_2O_3$, $Au/Co_3O_4$ found that $Au/TiO_2$ was the most active catalyst system and will be the primary support for all of these experiments.[7]

One of the most current hypotheses for the gold reaction mechanism (Eqns. 1.6-8) for CO oxidation is shown in Figure 1.16 proposed by Thompson et al.[33] This is a representation of the early stages of the oxidation of carbon monoxide at the periphery of an active gold particle. At the left, a carbon monoxide molecule is chemisorbed onto a low coordination number gold atom, and an hydroxyl ion has moved from the support to an $Au^{III}$ ion, creating an anion vacancy.[33] At the right they have reacted to form a carboxylate group, and an oxygen molecule occupies the anion vacancy as $O_2^-$.[33] This then oxidizes the carboxylate group by abstracting a hydrogen atom, forming carbon dioxide, and the resulting hydroperoxide ion $HO_2^-$ then oxidizes a further carboxylate species forming another carbon dioxide and restoring two hydroxyl ions to the support surface. This completes the catalytic cycle. There was no attempt by Thompson to suggest the charges carried by the reacting species. Also, there is no experimental evidence as to whether the oxygen derives from the gas or the support.[33]

$$CO + OH \rightarrow COOH \tag{1.6}$$
$$COOH + O_2 \rightarrow CO_2 + HO_2 \tag{1.7}$$
$$COOH + HO_2 \rightarrow CO_2 + 2OH \tag{1.8}$$
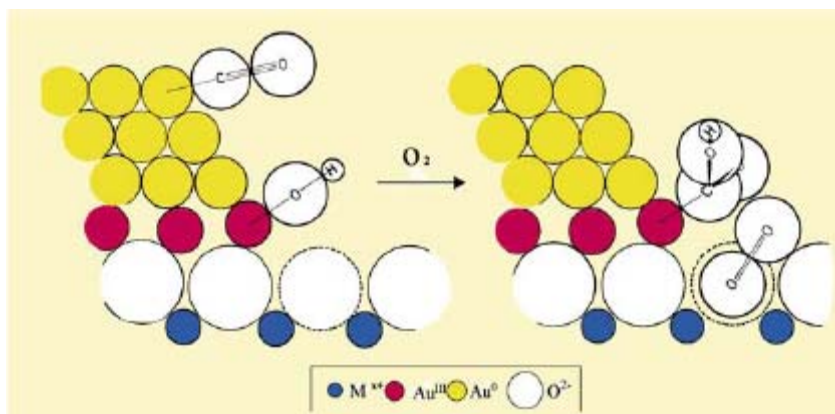
Figure 1.16 Representation of a possible mechanism for the oxidation of carbon monoxide using gold on an oxide support.[33]

### 1.6.3 Catalytic Species of Gold

Another point of contention among researchers is whether the active species of nano-gold is metallic gold, an oxidized gold species, or a sub-oxide. Some researchers believe that oxidized gold species, stabilized by an interaction with the support, are more active than $Au^0$ alone.[34] Other researchers conclude that the active species of Au for CO oxidation is $Au^{1+}$ with CO incorporating dual roles as both a reactant and a reducing agent for gold converting $Au^{1+}$ to $Au^0$.[31,35] Haruta believes that it is unlikely that an oxidized gold species is a candidate due to the fact that some of the most active catalysts are created by calcination in air at 573 K where the gold hydroxide and organic precursors are transformed into metallic species.[31] Goodman et al. suggested that the primary source of the catalytic activity of gold was non-metallic nanoparticle clusters.[31,36] It has been proposed that high temperature reduction/low temperature calcination results in higher catalytic activities for Au/TiO$_2$ systems and implies that fully reduced metallic gold along with a small percentage of gold oxide to be catalytically the most active.[37]

However, an important fact to consider when approaching nanometer diameters of gold particles is that the melting point can decrease significantly compared to the bulk properties as shown in Figure 1.17. The particles will melt and agglomerate thus increasing the particle diameters and decreasing the catalyst activity.[12]

19
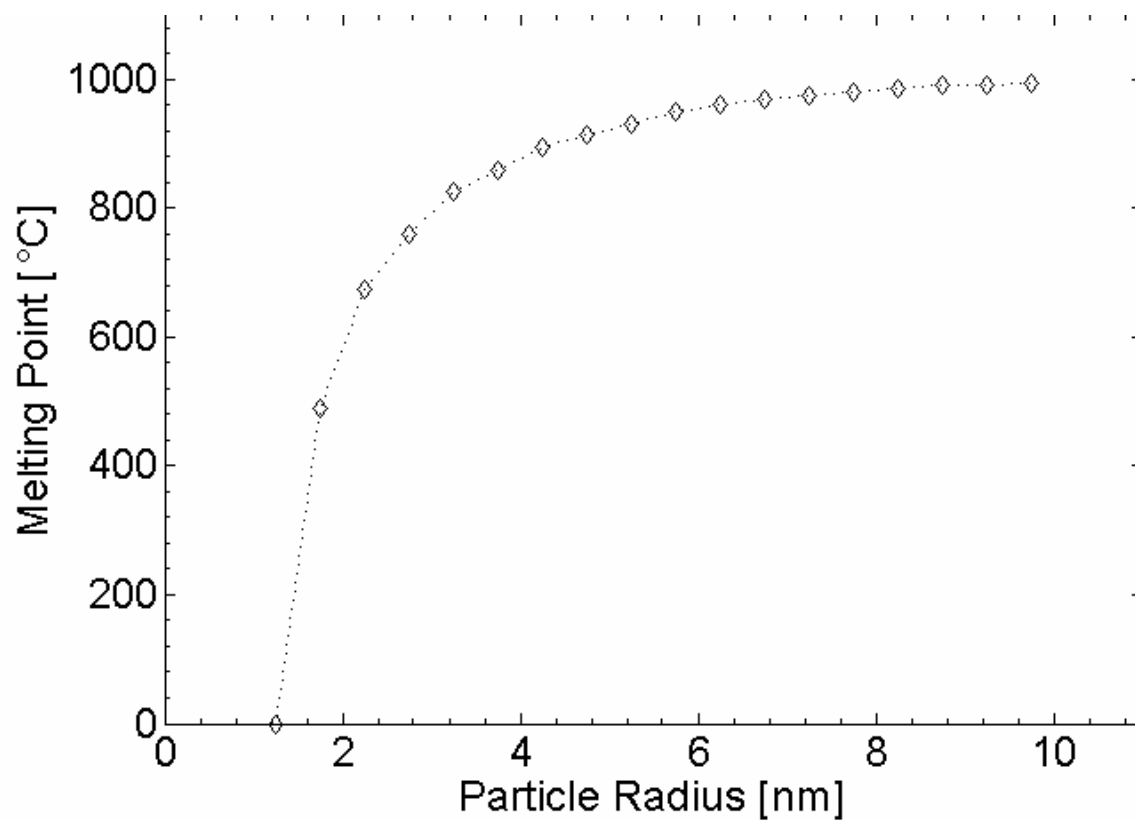
Figure 1.17  Relationship between particle size and melting point of gold nanoparticles.[12]

## 2 INITIAL CHARACTERIZATION

### 2.1 Introduction

This chapter describes the initial characterization of custom two-phase-method gold nano-particles fabricated by the Interfacial Phenomena and Polymeric Materials research group, the $TiO_2$ support through all experiments, and the reference $Au/TiO_2$ sample purchased from the World Gold Council. After describing both the fabrication procedure of the two-phase-method gold nanoparticles and the $TiO_2$ supported Au catalyst, oxidation state is verified via XPS and the morphology of each is examined with SEM micrographs. The crystallography of the support is confirmed via XRD. Initial examination of the adsorption of CO to the $TiO_2$ support is presented. Lastly, the preliminary characterization of the GNPs purchased from the World Gold Council via XPS and SEM which contrasts the similarities and differences between the purchased reference and the custom two-phase-method gold nanoparticles fabricated. Kinetic information will be described in detail for both catalysts in Chapters 3 and 4.

### 2.2 Two-Phase-Method Nano-Au/TiO₂ Catalyst

#### 2.2.1 Fabrication and Pre-Treatment of the Two-Phase-Method GNPs

The experimental gold nanoparticles (GNPs) were synthesized in an organic medium following the method reported by Brust et al.[38,39] The fabrication procedure of the two-phase-method GNP solution, as described by Dayling Chaparro[38-40], begins with a 38 mM aqueous solution of hydrogen tetrachloroaurate ($HAuCl_4$) added slowly to a 13 mM solution of tetraoctylammonium bromide (TOAB) in toluene. The TOAB is used to stabilize the nanoparticles in solution. The solution was then stirred for 1.5 hr to allow the metal salt to be transferred to the organic phase. To reduce the $Au^{3+}$ ions to metallic gold ($Au^0$), a freshly prepared aqueous solution of 0.13 M sodium borohydride ($NaBH_4$) was added drop wise to the mixture while stirring. The solution turned ruby red after the

gold reduction which indicates the formation of nanoparticles of gold. After stirring overnight, the organic layer was separated from the aqueous layer and washed with water, 0.1 M HCl, and 0.1 M NaOH respectively. The rinsing procedure was repeated three times and a final wash with DI water was performed. The organic layer containing the GNPs/TOAB was allowed to dry with anhydrous sodium sulfate ($NaSO_4$) for 1 hr. Finally, after recovery of the GNPs in toluene, the solution was transferred to an amber bottle and refrigerated.

As illustrated in Figure 2.1, after the formation of the GNPs, TOAB completely surrounds the Au particle clusters maintaining their diameters. While this is designed to prevent agglomeration, it may also be a hindrance to gas transport to the particle surface if not fully removed prior to reaction.
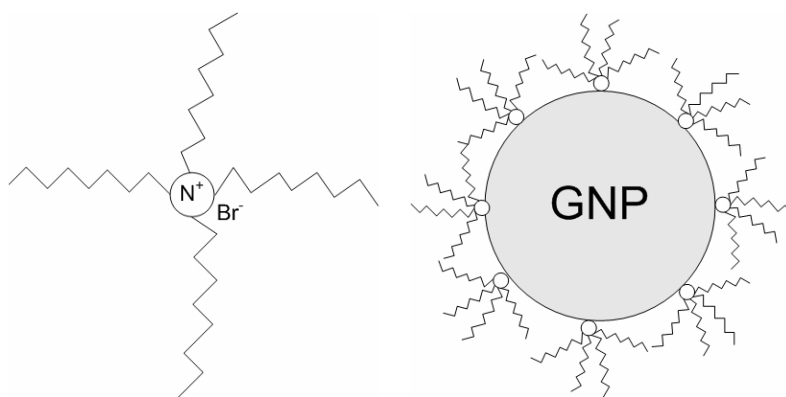


Figure 2.1  Tetraoctylammonium bromide molecule (TOAB) $[CH_3(CH_2)_7]_4NBr$ binds to the gold particles to prevent aggregation.[41]

The Au-nanoparticles, suspended in solution (4 mg GNPs/16 mL Toluene), were then combined with titanium dioxide ($TiO_2$) via incipient wetness techniques. To begin the procedure, the entire Au solution was blended with anatase $TiO_2$ ((4 mg GNPs/16 mL Toluene):100 mg $TiO_2$) to form a 4% Au mixture. Then, the solution was continuously stirred at room temperature for 1 hour prior to heating at 150$^o$C. The Au-solution evaporated leaving a pinkish-red powder. The entire sample was then loaded into the tubular reactor as explained in Chapter 1.4.3. Beginning at room temperature, the sample was ramped 30$^o$C/min to 500$^o$C in air (100 sccm, 1 atm) and held at 500$^o$C for 3 hours, as

illustrated in Figure 2.2. Then it was allowed to cool back to room temperature in ambient atmosphere. The sample was then reduced in a hydrogen atmosphere (100 sccm, 1 atm) at 400°C for 3 hours, and then allowed to cool. The final pre-treatment step was to slightly oxidize the sample for 2 hours in air (100 sccm, 1 atm) at 200°C. This preparation procedure is based on pre-treatment techniques used by Haruta and Choudhary.[31,37] The calcination step is used to remove any excess volatile compounds and promote Au/TiO$_2$ contact; however, a side effect of the calcination process is gold agglomeration.[31] Studies have shown that the high temperature reduction (400°C in H$_2$) induces some catalytic activity towards CO oxidation in the TiO$_2$ and reduces the gold to its metallic state.[37] The low temperature oxidation promotes the formation of a small amount of oxide and sub-oxide species in the gold.[37] Several proposed mechanisms suggest that one of the active species of gold is the sub-oxide formed during this step as discussed in Chapter 1.5.2.[33]
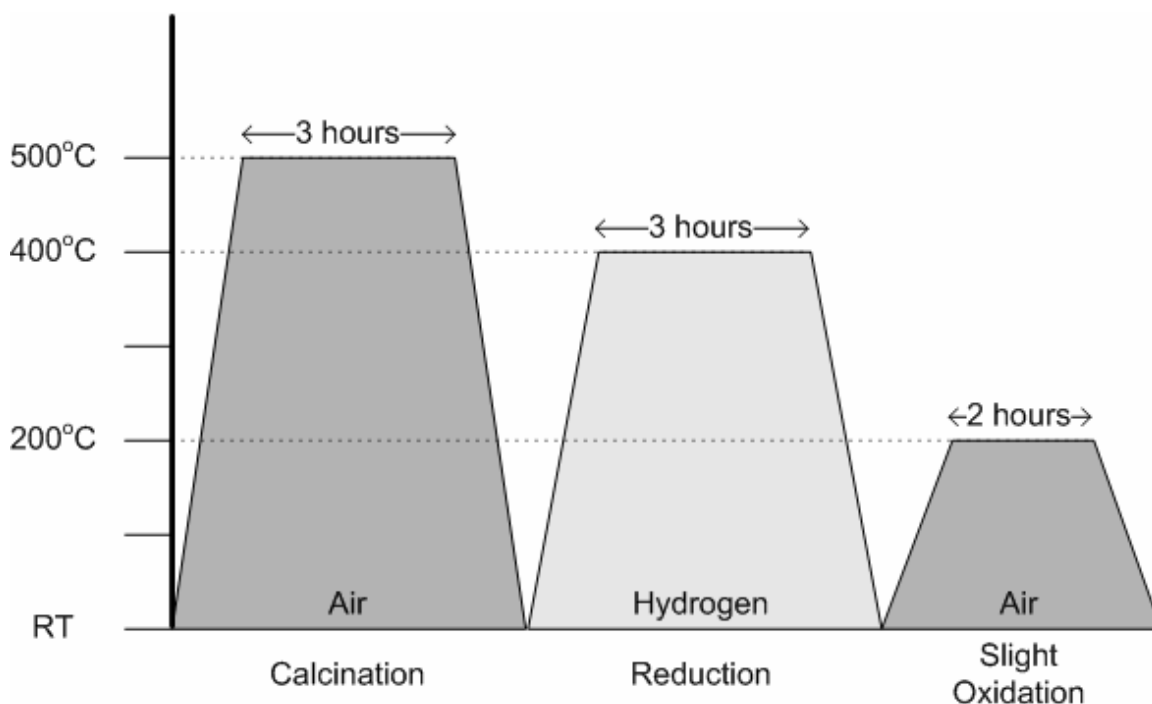


Figure 2.2 Two-phase-method nano-Au catalyst preparation procedure.

## 2.2.2 DLS Analysis

Dynamic light scattering (DLS) verified the gold nanoparticle diameters in solution before combination with the titania support. These experiments contain a range of particles with diameters of $1 \pm 0.25$ nm.

## 2.2.3 X-ray Photoelectron Spectroscopy (XPS)

In order to determine the effect of heat treatments on the oxidation state of GNPs, a small amount (0.6 mL) of the 4 mg GNPs/16 mL toluene solution was applied to the surface of a silicon wafer (Figure 2.3) and evaporated at $150^{\circ}$C overnight in a furnace (Figure 2.4). A silicon wafer was chosen because the XPS binding energy reference peaks for silicon dioxide (Si 2p, 103.4 eV) would not interfere with those of gold (Au $4f_{7/2}$, 84.00 eV). Additionally, the silicon substrate is able to withstand the calcination temperature ($500^{\circ}$C) without a phase change or melting. After an initial XPS reference spectrum of the dried GNPs (Figure 2.5), the Au/silicon sample was then placed in a furnace for 3 hours at $500^{\circ}$C in air at ambient pressure. A second XPS measurement was performed on the calcined sample to determine any changes in the oxidation state of the gold (Figure 2.6).

Exposure to $500^{\circ}$C in air at atmospheric pressures resulted in a reduction in the full width at half maximum (FWHM) of the $Au^{0}$ $4f_{7/2}$ peak (84.00 eV) and $Au^{0}$ $4f_{5/2}$ peak (87.71 eV), which suggests that the GNPs become more single crystalline in nature and no oxidation did occur at this temperature.[42] This is expected since gold oxide decomposes into its elements above $350^{\circ}$C.[43]

Figure 2.3  4 mg GNPs/16 mL toluene on a silicon wafer (single crystal 100 plane).

Figure 2.4  4 mg GNPs/16 mL toluene evaporated onto a Silicon Wafer after overnight 100$^{o}$C evaporation.
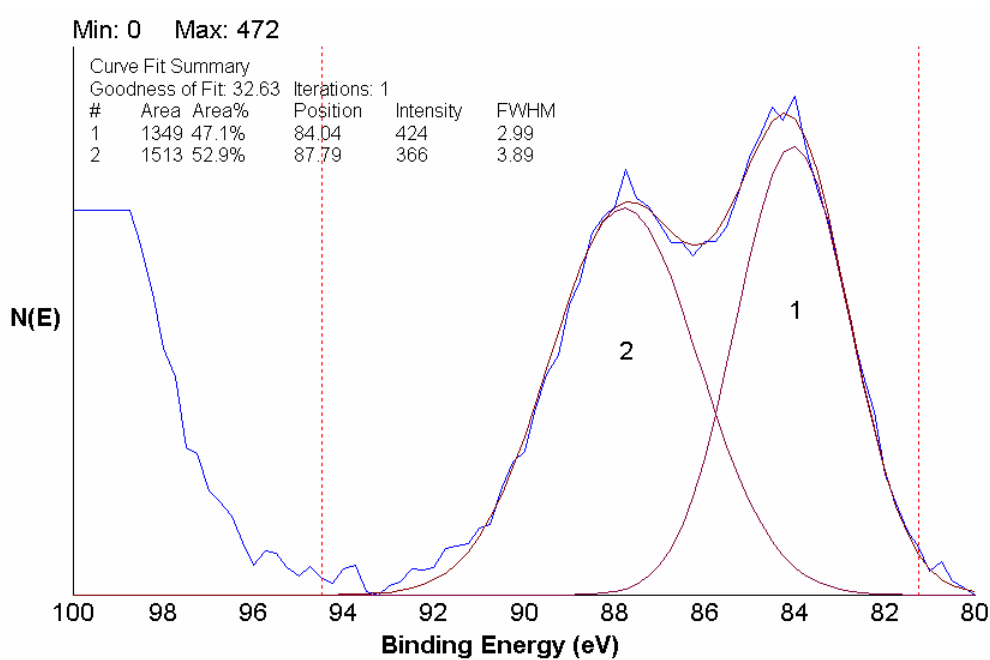


Figure 2.5  High resolution XPS Au 4f$_{7/2}$ spectra of the two-phase-method GNP/silicon as-received after 100$^{o}$C evaporation.
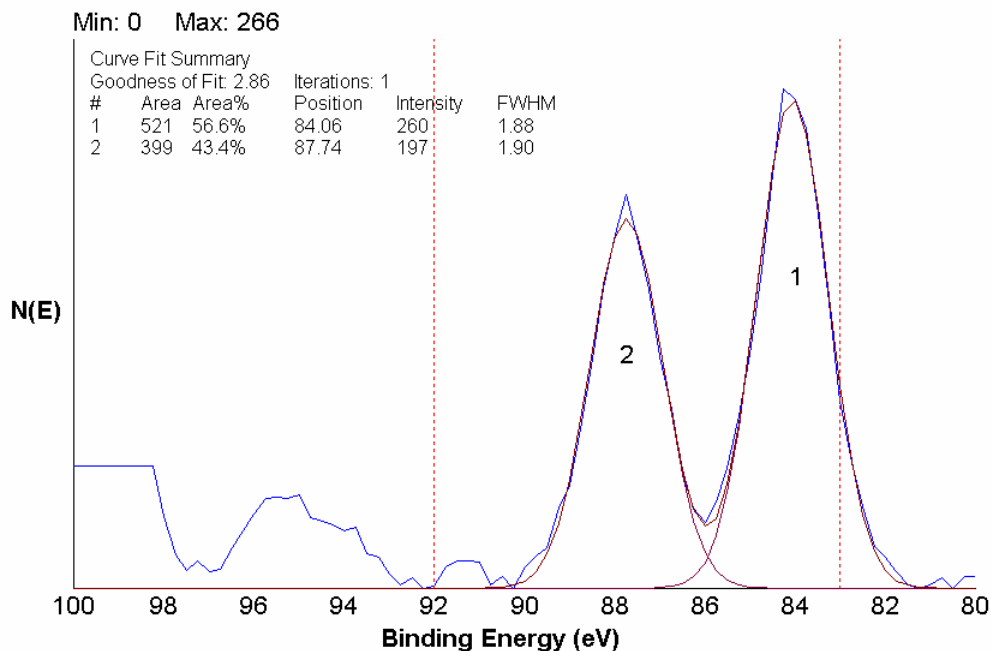
Figure 2.6 High resolution XPS Au 4f$_{7/2}$ spectra of the two-phase-method GNP/silicon after 3 hours at 500$^{o}$C in air.

### 2.2.4 Scanning Electron Micrographs of the Two-Phase-Method GNPs on a Silicon Wafer

SEM micrographs of the gold particles on the silicon surface after air drying were difficult to image (Figure 2.7). This would suggest that the particles are coated with a non conductive film. After the GNP solution was placed in a furnace overnight at 150$^{o}$C in air at ambient pressure, the particles then appeared in the SEM micrograph (Figure 2.8). The 150000x micrograph, Figure 2.9, shows that the particle sizes are quite large.(~100 nm). This could be a result of the nanoparticle mobility on the surface of the wafer leading to agglomeration of the particles.
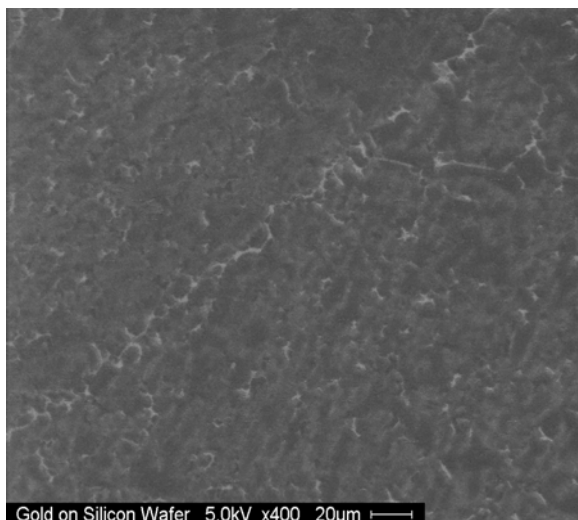
Figure 2.7  SEM (400x) Micrograph of 4 mg GNPs/16 mL toluene air dried onto a silicon wafer.
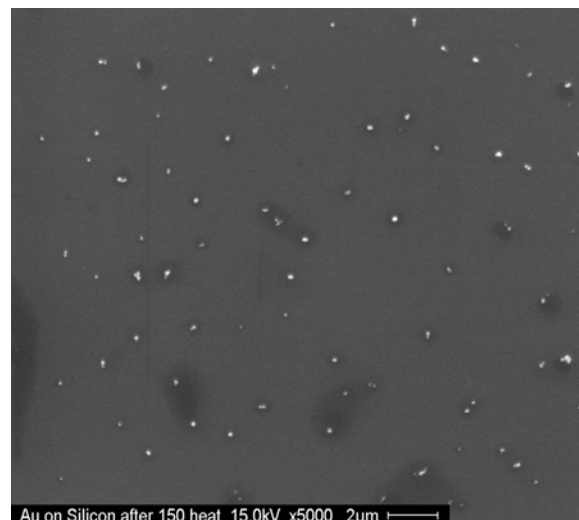


Figure 2.8  SEM (5000x) micrograph of 4 mg GNPs/16 mL Toluene on a silicon wafer after exposure to $150^{\circ}$C.
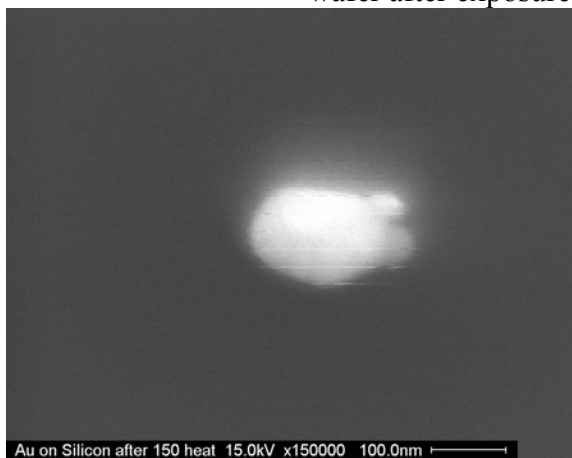


Figure 2.9  SEM (150000x) micrograph of 4 mg GNPs/16 mL toluene evaporated onto a silicon wafer after exposure to $150^{\circ}$C.

## 2.3   Titanium Dioxide ($TiO_2$)

### 2.3.1   XRD and SEM of the Experimental Support

Titanium (IV) oxide powder (Sigma-Aldrich, 99.8%) was used exclusively for the support material for all experiments.  While not explicitly noted, XRD spectra of the support confirmed an anatase crystal structure (Figure 2.10).  SEM micrographs revealed $TiO_2$ particle diameters of ~100 nm (Figure 2.11).  BET measurements (named for Brunauer, Emmett and Teller) of the titania support estimated the specific surface area to

be ~7.16 m$^2$/g with an external area of 4.51 m$^2$/g and a micropore surface area of 2.65 m$^2$/g. The average pore diameter is 84 angstroms.
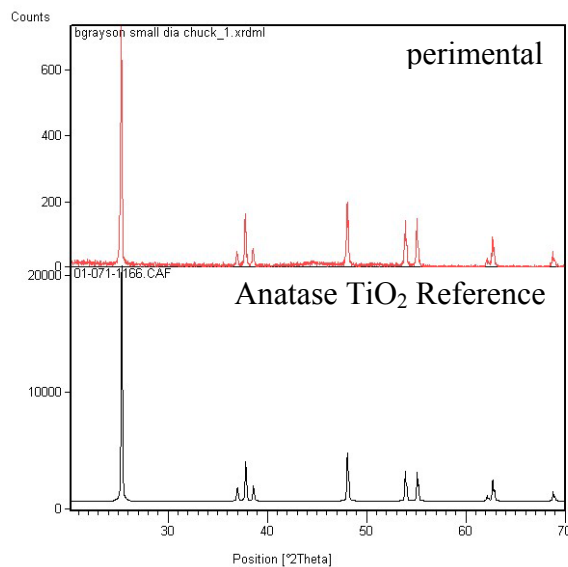


Figure 2.10 XRD spectra of as-received titanium dioxide support.
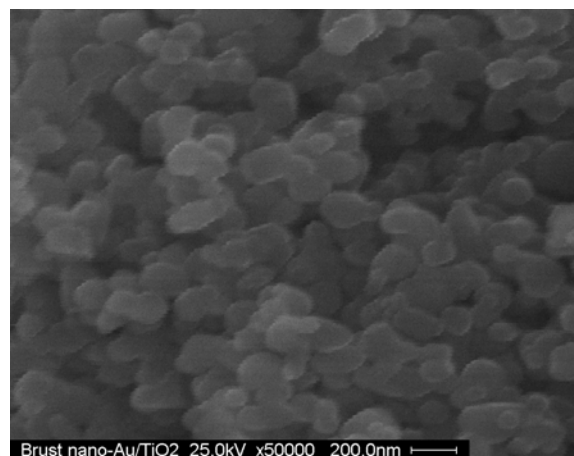
Figure 2.11 SEM micrograph (50000x) of the as-received titania support.

To determine the effect of calcination temperatures on the support, the titania was calcined in an oven for 8 hours at 500$^o$C in air at atmospheric pressure. High temperature processes performed on TiO$_2$ have been shown to cause a transformation from the anatase phase to rutile.[37] XRD analysis verified that a small percentage of the titania recrystallized into the rutile phase (Figure 2.12). It has been proposed that this partial reconstruction creates an optimized interaction between the GNPs and the titania support, leading to higher dispersion and increased CO oxidation activity.[37]
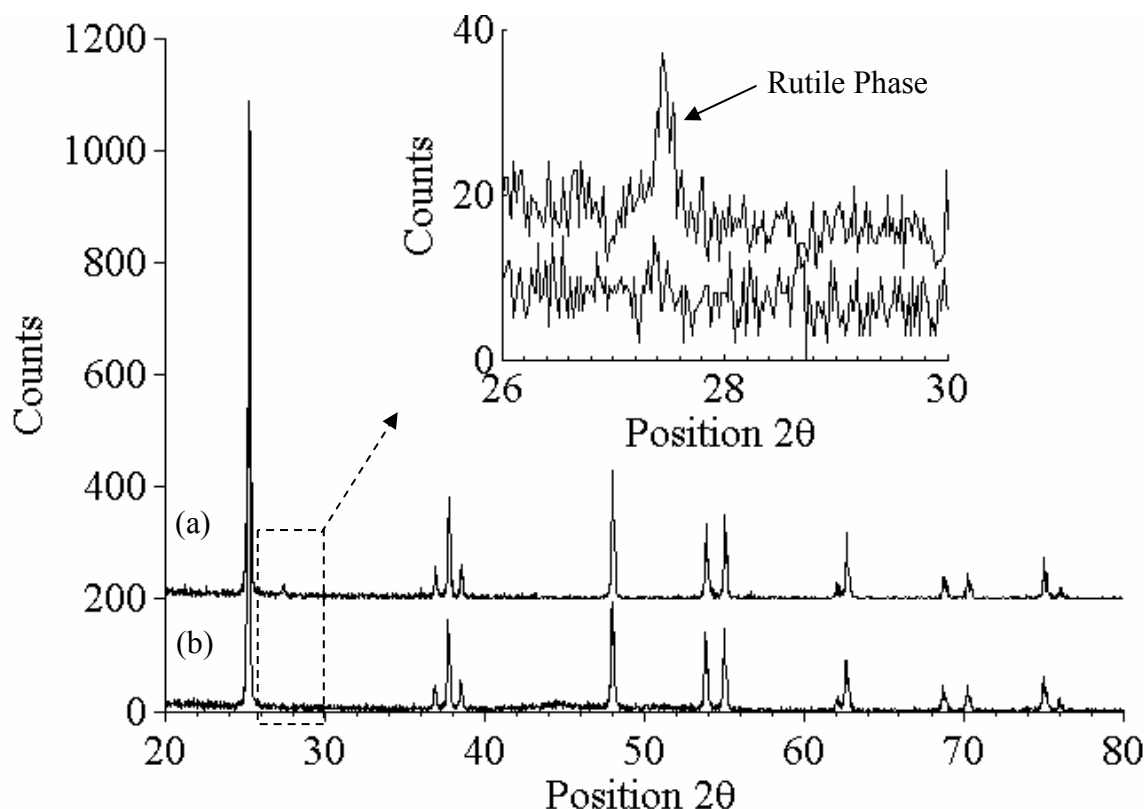
Figure 2.12  XRD spectra of (a) titania after 500°C calcination (b) titania as-received.

2.3.2    Aabspec FTIR Micro-reactor

The next characterization technique involved the use of the Aabspec system described in Chapter 1.4.3.1.  Influent flows to the FTIR reaction chamber were 50 sccm $N_2$, 99 sccm $H_2$, 1 sccm CO, and 20 sccm of air.  The reaction chamber was maintained under steady-state operating conditions for 30 minutes before data collection with temperature ramping from 25-125°C in 25°C increments at atmospheric pressure.  A 30 mg 1:1 titanium dioxide/potassium bromide ($TiO_2$/KBr) pellet, 7 mm diameter, 0.5-1.0 mm thick, was inserted into a variable temperature IR transmission probe and positioned such that the pellet face intersected the infrared (IR) beam.  KBr is a common inert binding agent which allows the formation of rigid pellets and does not influence the measured IR spectrum wavenumber range (4000-400 $cm^{-1}$).  The FTIR is able to detect the three primary constituents of the gas stream other than hydrogen: CO, $CO_2$, and $H_2O$ (Figure 2.13).  One of the main limitations of the FTIR technique is its inability to analyze

diatomic species. This is the primary reason that the GC was used in conjunction with the FTIR for effluent analysis.
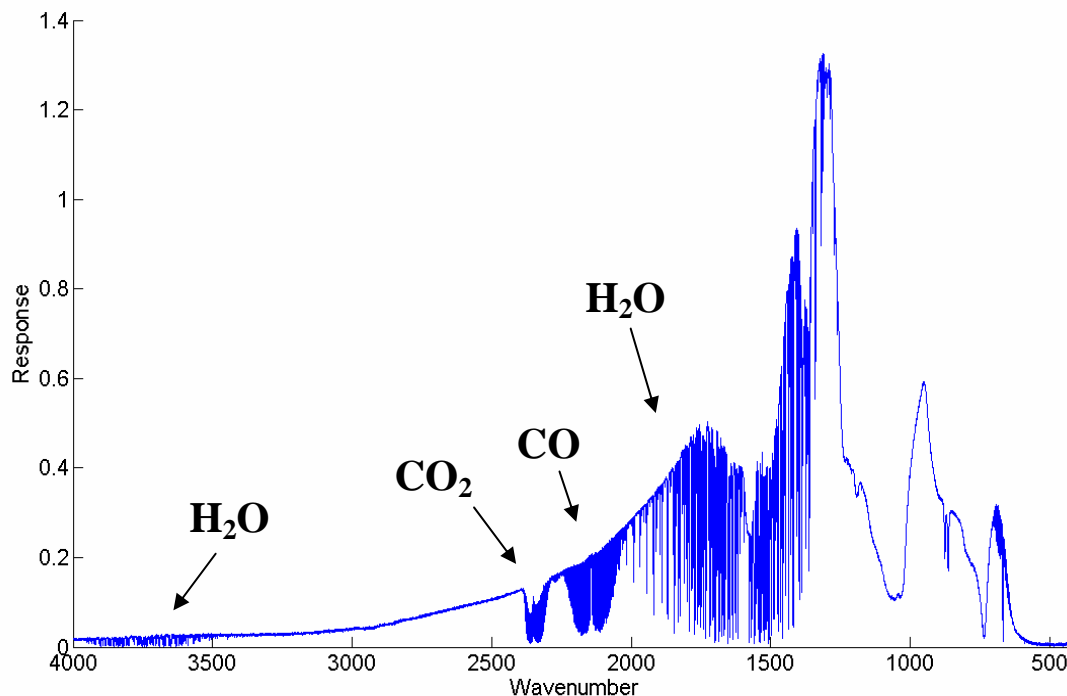


Figure 2.13  Representative FTIR response curve for the reaction effluent.

FTIR transmission absorbance spectra of the 30 mg 1:1 $TiO_2$/KBr pellet are shown in Figure 2.14. While the IR region of CO is located between 2000 and 2250 $cm^{-1}$, a smaller representative R-branch spectral region (2145-2230 $cm^{-1}$) for integration was chosen to eliminate interferences from both $CO_2$ and $H_2O$ in the CO P-branch (2110-2175 $cm^{-1}$).[44] After baseline correction of the absorbance spectral region, the integral of the defined R-branch in each data set was calculated. Since absorbance is linearly proportional to concentration, Figure 2.15 shows that the concentration of adsorbed carbon monoxide decreases with increasing temperature, indicating a negative temperature dependence on the available reserve of CO on the surface of the support. Previous studies on both anatase and rutile $TiO_2$ found that CO only weakly adsorbs to the support surface so it seems reasonable that the sticking coefficient would decrease with increasing temperature.[45-48] Other reported results show that the sticking probability

30

of CO on metal oxides such as ZnO decreases with increased temperature which supports the results seen here on a similar oxide support, $TiO_2$.[49] All of these studies support the negative correlation reported in Figure 3 for the temperature dependence of CO adsorption on $TiO_2$.
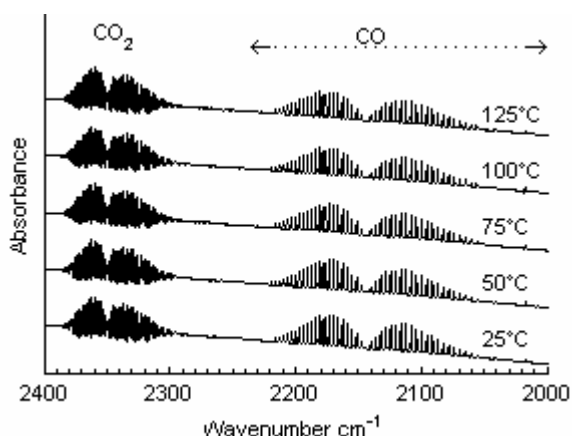


Figure 2.14  FTIR absorbance spectra of the 30 mg 1:1 $TiO_2$/KBr pellet.
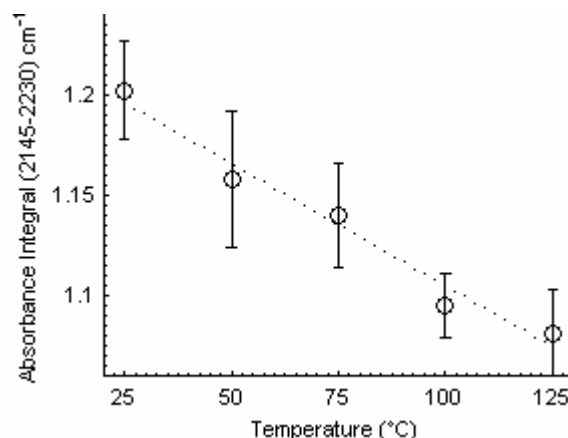
Figure 2.15  FTIR transmission mode CO characteristic peak absorbance integral of the 30 mg 1:1 $TiO_2$/KBr pellet at 25-125°C

### 2.3.3   XPS Analysis

The following three figures are high resolution XPS spectra for the titanium $2p_{1/2}$ and titanium $2p_{3/2}$ doublet peak after a three hour calcination at 500°C in air (Figure 2.16), a three hour reduction at 400°C in hydrogen (Figure 2.17), and a 2 hour slight oxidation at 200°C in air (Figure 2.18).  Gaussian curves labeled "1" and "2" are representative XPS photoelectron features for $TiO_2$ (458.9 eV and 464.3 eV).  Throughout the entire process, these figures show that the $TiO_2$ did not experience a change in oxidation state.  The primary differences between the three figures are the measurements of the width of each Gaussian curve (FWHM – full width at half maximum).  The FWHM is an indication of the degree of crystallinity of the support with smaller values suggesting a more crystalline state.  These results would indicate a restructuring of the crystal lattice of the $TiO_2$; yet, the oxidation state remains constant and does not oxidize to $Ti_2O_3$.  The restructuring of $TiO_2$ from anatase to rutile is observed in the XRD analysis discussed in Section 2.3.1.

31

Min: 0    Max: 1217

Curve Fit Summary
Goodness of Fit: 10.49  Iterations: 1
| # | Area | Area% | Position | Intensity | FWHM |
|---|------|-------|----------|-----------|------|
| 1 | 3351 | 64.8% | 458.88 | 1209 | 2.60 |
| 2 | 1824 | 35.2% | 464.29 | 489 | 3.51 |
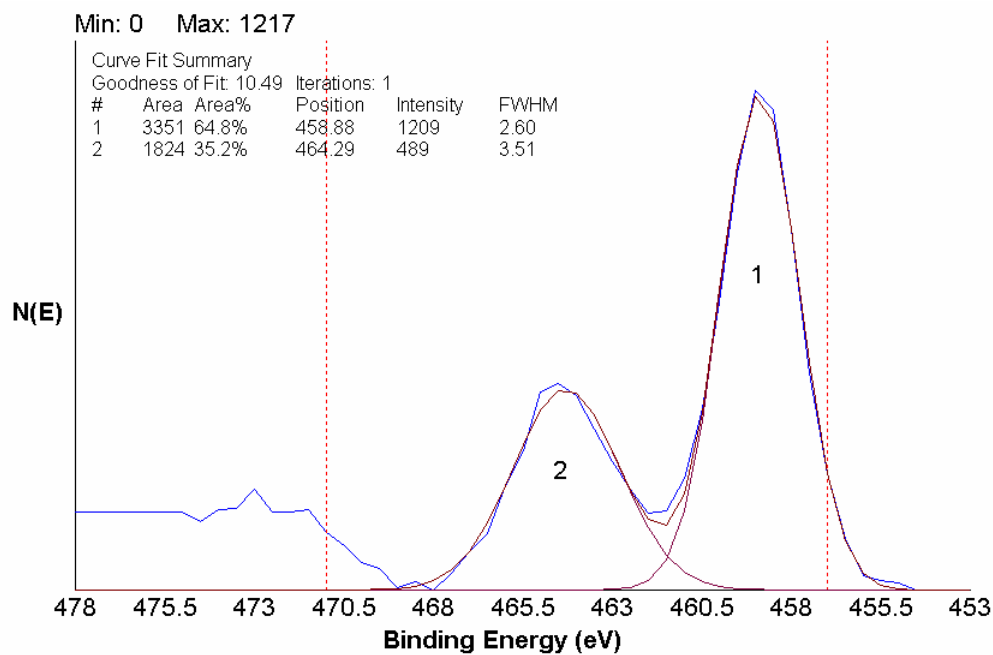
Figure 2.16  Anatase $TiO_2$ powder XPS spectra after air calcination at $500^{o}C$ for 3 hours.

Min: 0    Max: 5199

Curve Fit Summary
Goodness of Fit: 42.36  Iterations: 1
| # | Comment | Area | Area% | Position | Intensity | FWHM |
|---|---------|------|-------|----------|-----------|------|
| 1 | | 20606 | 66.8% | 459.02 | 5151 | 3.76 |
| 2 | | 10255 | 33.2% | 464.34 | 2332 | 4.13 |
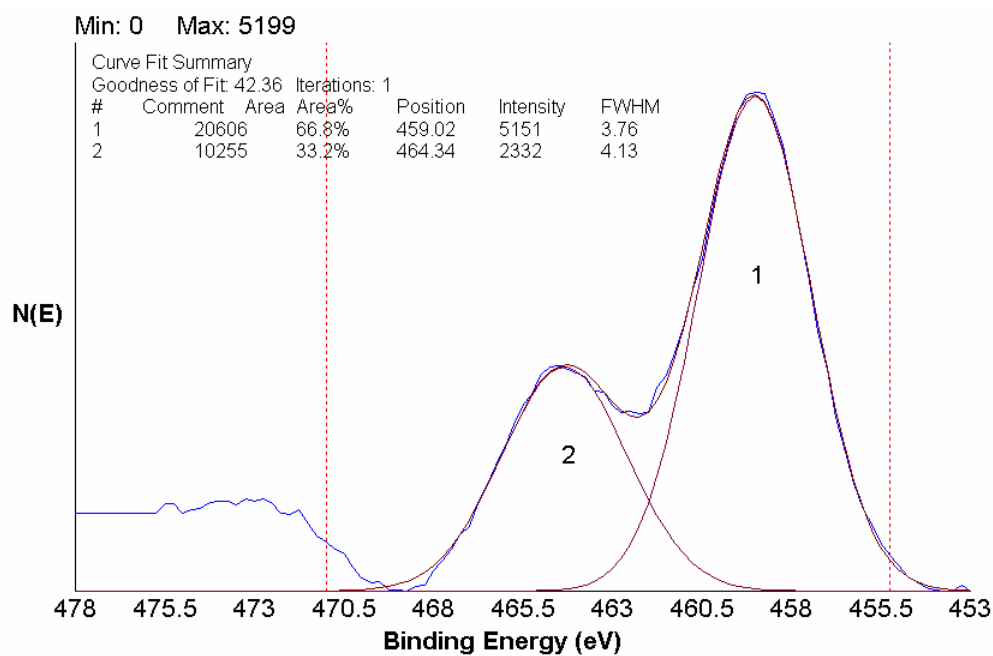
Figure 2.17  Anatase $TiO_2$ powder XPS spectra after air calcination at $500^{o}C$ for 3 hours and hydrogen reduction at $400^{o}C$.

32
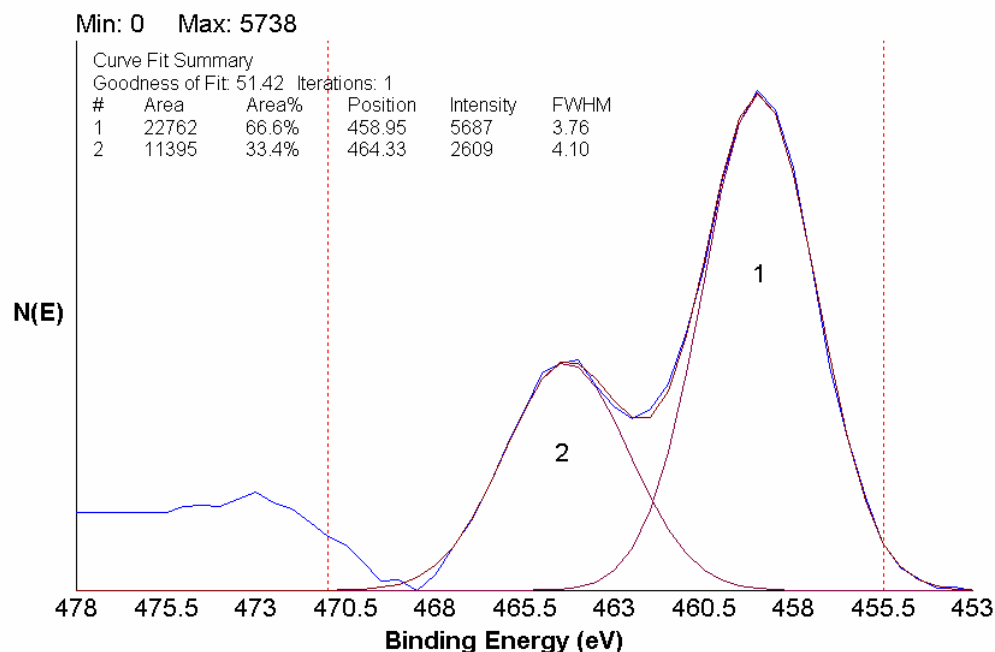
Figure 2.18  Anatase $TiO_2$ powder XPS spectra after air calcination at 500$^o$C for 3 hours and hydrogen reduction at 400$^o$C and slight oxidation in air at 200$^o$C.

## 2.4    World Gold Council Reference Catalyst "A" (nano-Au/$TiO_2$)

According to the material safety data sheet (MSDS), the catalyst A contains 1.5 wt% Au with the balance $TiO_2$, and it was prepared via deposition/precipitation.  The average diameter of the gold particles, verified via TEM, is 3.3 nm with a standard deviation of 0.72 nm.[13]  Additionally, it has been shown, in a fixed bed flow reactor, the temperature at which there is a 50% conversion for CO oxidation is -46$^o$C.[13]  Accordingly, the temperature at which there is a 50% conversion for $H_2$ oxidation is 40$^o$C.[13]  Therefore, the WGC reference is highly reactive with both CO and $H_2$ at the typical fuel cell operating temperature of 80$^o$C.

SEM micrographs of the WGC reference catalyst shows that the average particle size is a lot smaller than the Sigma-Aldrich support used in all experiments.  This may be an advantage of the reference material that needs to be explored in my system.  Ball-milling may be a requirement to lower the average diameter of the support material.
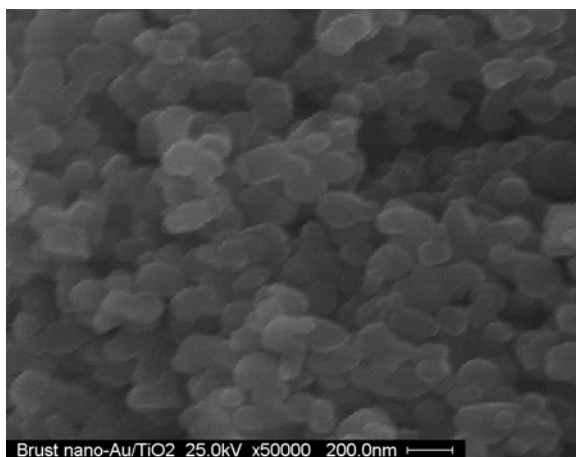
Figure 2.19 SEM micrographs of the two-phase-method gold reveal similar pictures to the As-received $TiO_2$ used as a support.
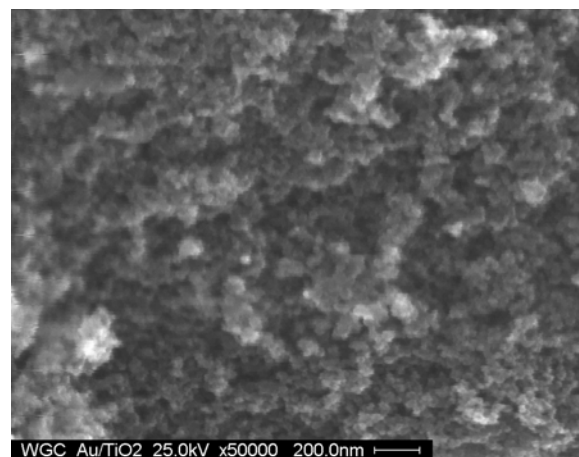
Figure 2.20 SEM micrographs of the WGC show much small particle sizes for the $TiO_2$ support used in their samples.

## 2.4.1 XPS Analysis

Analysis of the XPS spectrum (Figure 2.21) reveals that the World Gold Council supported nano-Au is primarily metallic gold, $Au^0$ $4f_{7/2}$ peak (84.00 eV) and $Au^0$ $4f_{5/2}$ peak (87.71 eV). This is comparable to the two-phase-method nano-Au provided by the Interfacial Phenomena and Polymeric Materials research group (Figure 2.6). Although there is the possibility of a suboxide species present, $Au^{+1}$, the minute quantity of the sample and resolution make it difficult to distinguish.



Min: 0    Max: 42

Curve Fit Summary
Goodness of Fit: 0.17    Iterations: 2

| # | Area | Area% | Position | Intensity | FWHM |
|---|------|-------|----------|-----------|------|
| 1 | 79 | 52.8% | 83.95 | 41 | 1.80 |
| 2 | 70 | 47.2% | 87.62 | 26 | 2.54 |
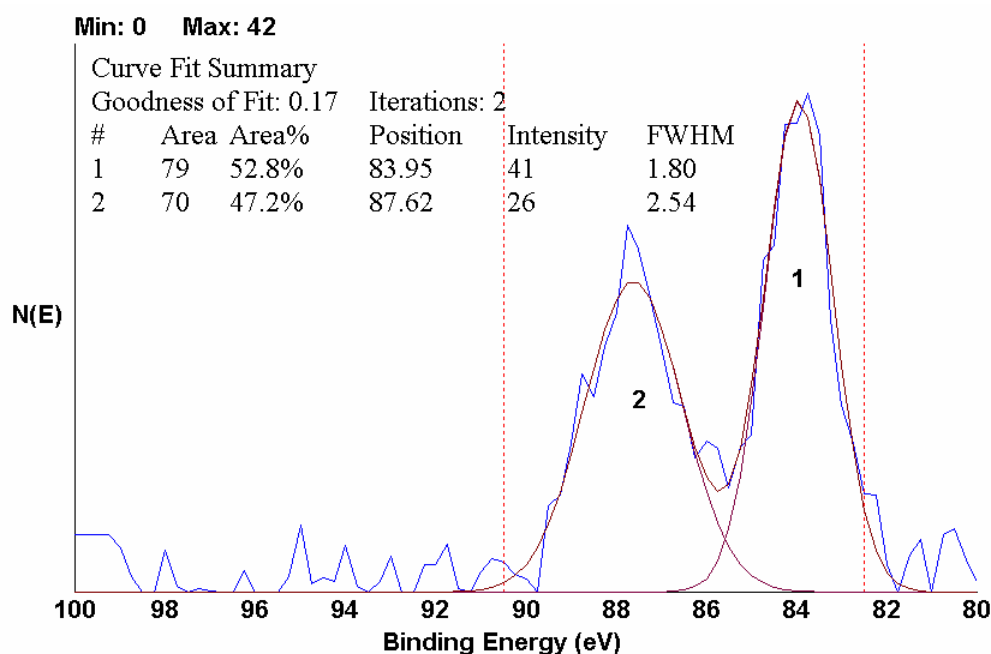
Figure 2.21 WGC nano-Au/$TiO_2$ XPS spectrum.

34

2.5    Summary of Results

Initial characterizations of the two-phase-method gold nanoparticles, titanium dioxide, and the world gold council supported Au/TiO$_2$ were performed.  After the two-phase-method gold nanoparticles were successfully fabricated and combined with TiO$_2$ via incipient wetness techniques, a pre-treatment procedure based on techniques used by Haruta and Choudhary was developed.  This method includes a calcination step at 500$^o$C for solvent removal, a reduction step at 400$^o$C to reduce the GNP to their metallic state, and a slight oxidation step at 200$^o$C to promote the formation of sub-oxide gold species.  XPS verified the metallic state of the GNPs after exposure to 500$^o$C calcination temperature.  Finally, SEM illustrated the high mobility of the GNPs under relatively mild conditions.  This was a cause for concern because of the deactivation of the particles above ~100 nm diameters.

Continuing with the characterization, the TiO$_2$ was then examined.  After calcination at 500$^o$C in air at atmospheric pressure of the TiO$_2$ support, XRD confirmed that the crystal structure changed from anatase to rutile in a small percentage of the sample.  The presence of the rutile phase is suggested to be advantageous due to an optimized interaction between the GNP and the TiO$_2$ support.  Analysis of the TiO$_2$ support via FTIR found that the available CO concentration on the support surface to have a negative temperature dependence when varying the system temperature from 25$^o$C-125$^o$C.  This result is proposed to be due to the decreasing sticking probability of CO on the TiO$_2$ support with increasing temperature, the weak adsorption of CO on the support surface, and the decreasing residence time of CO with increasing temperature.

Lastly, the World Gold Council was characterized via SEM and XPS.  SEM micrographs of the World Gold Council Au/TiO$_2$ catalyst revealed that the support used for its catalyst have much smaller diameter particles than the anatase TiO$_2$ used in the two-phase-method gold experiments.  XPS spectra showed that the WGC supported GNPs are metallic gold and very similar to the two-phase-method GNP provided by Dr. Gupta.

# 3 DEVELOPMENT OF TWO-PHASE-METHOD AU NANOPARTICLE TESTING PROCEDURES AND PROTOCOLS FOR THE OXIDATION OF CO

## 3.1 Introduction

In order to verify the ability of the two-phase-method GNP catalyst provided to oxidize CO in excess hydrogen, an effluent testing protocol was developed. To determine CO conversion, the wavenumber range for each species of the FTIR absorbance spectrum must be integrated and referenced to a background spectrum. Experimental artifacts corresponding to an eight hour cycle in the absorbance data were observed. These artifacts, identified as shifts in the calculated absorbance integrals, were first attributed to the FTIR heating/cooling cycle. This problem made conversion calculations impossible. After identifying the problem, attempts were made to remove the issue through the use of a non-reactive reference species such as methane. After noticing inconsistencies in the noise levels at different temperatures, baseline adjustments for each species and $N_2$ purging to eliminate background $CO_2$ and $H_2O$ contamination were found to be critical for direct comparison of results. After these calibration corrections were implemented, accurate assessments of the two-phase-method GNP catalyst CO oxidation activity was evaluated.

## 3.2 Twenty-four Hour Analysis of Two-Phase-Method GNP Catalyst FTIR Absorbance Integrals

To determine the effluent characteristics of the two-phase-method GNP catalyst, a twenty-four hour experiment was designed to record the absorbance integral of CO (2000-2250 $cm^{-1}$), $CO_2$ (2250-2400 $cm^{-1}$), and $H_2O$ (1400-1900 $cm^{-1}$) every hour (Figure 3.1). The absorbance integral is linearly proportional to the concentration of the species and will be essential in determining the conversion potential of these catalysts. As stated previously in Section 3.2, a 1% two-phase-method $GNP/TiO_2$ catalyst was prepared by incipient wetness and dried, calcined, reduced, and slightly oxidized for FTIR analysis.

The influent stream of 99 sccm $H_2$, 1 sccm CO, 50 sccm $N_2$, and 5 sccm air was reacted isothermally at $200^oC$ and 1 atm. Specie concentrations were then evaluated via ratios of the absorbance integrals.

Initial observation showed a cycling pattern of the FTIR absorbance integrals approximately every 8 hours (Figure 3.1). The mercury cadmium telluride (MCT) detector reservoir is filled with liquid nitrogen at the beginning of each experimental run and allowed to equilibrate for approximately 2 hours before data collection. After every 8 hours, the detector reservoir was refilled. It is hypothesized that the detector is warming over the period of 8 hours. Once the detector is cooled again with liquid nitrogen, the measured integral value readjusts to a new value. In the case of the CO integral, this can be up to about 10-20%. With this large movement in the integral value proposed to be due to the detector warming/cooling over a period of time, it is impossible to determine if the concentration is changing because of a reaction. The second concern with the FTIR spectra is the negative integrals for both the water and carbon dioxide. Since concentration is linearly proportional to the integral of the absorbance, negative values do not have any physical meaning. This can be explained through the calculation of FTIR absorbance (Eqn. 3.1). If the background response curve ($I_o$) is approximately equal to the experimental response ($I$), then the calculation of absorbance can produce negative values caused by noise. The integral of negative values could lead to the values calculated.

$$\text{Absorbance} = A = \log(I_o/I) = ecL \tag{3.1}$$

The FTIR experimental concentration ratios of $CO/CO_2$, $CO/H_2O$, and $CO_2/H_2O$ established a stabilized system after ~2 hours (Figure 3.2) since the ratio values were found to be proportional to each other.

MCT detector filled
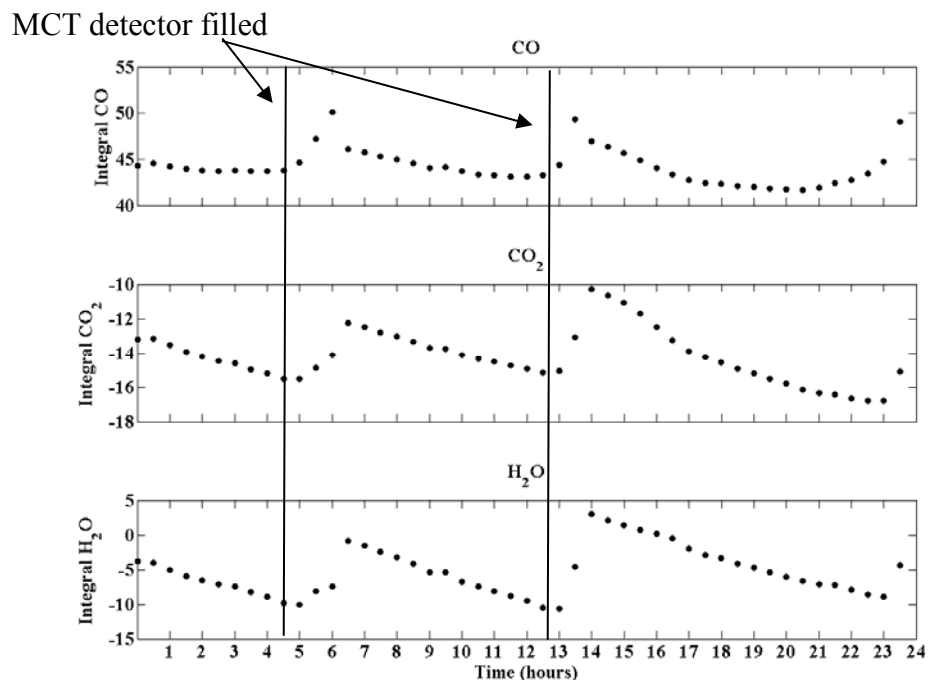


Figure 3.1  FTIR absorbance integrals of carbon monoxide, carbon dioxide and water at $200^{o}$C.  Influent gas composition: 99 sccm $H_2$, 1 sccm CO, 50 sccm $N_2$, and 5 sccm air.
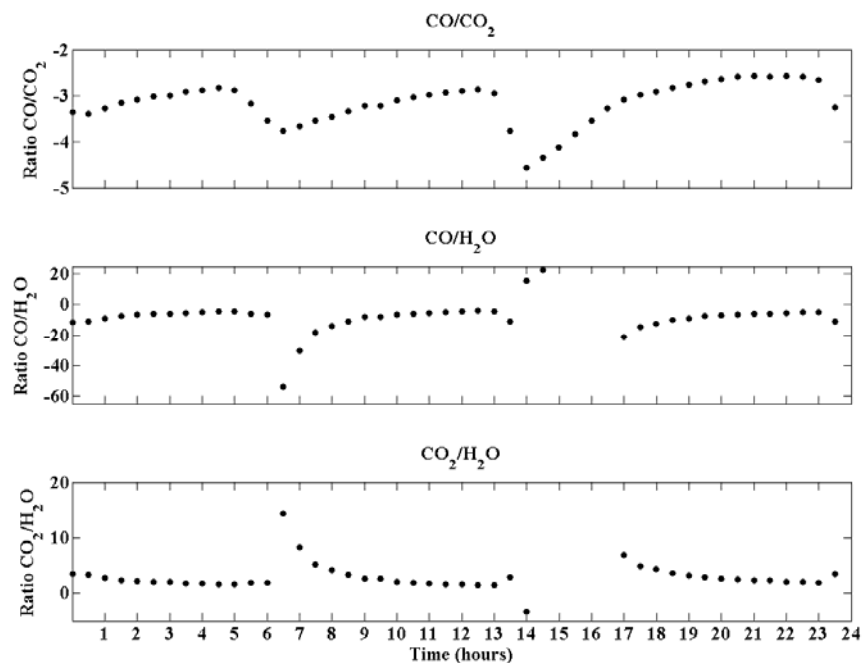


Figure 3.2  Ratios of FTIR absorbance integrals of carbon monoxide, carbon dioxide and water at $200^{o}$C.  Influent gas composition: 99 sccm $H_2$, 1 sccm CO, 50 sccm $N_2$, and 5 sccm air.

In subsequent experiments, the air concentration was increased to 15 sccm to determine if the oxygen concentration may be limiting the reaction; all other influent components remained constant. To determine any temperature dependence on the absorbance integral, isothermal reactions were evaluated at $200^{\circ}$C (Figure 3.3 and Figure 3.4), $300^{\circ}$C(Figure 3.5 and Figure 3.6) and $425^{\circ}$C(Figure 3.7 and Figure 3.8). Initial results were inconclusive until the experimental artifacts were removed. The final results are discussed in Section 4.4.

Once again, an 8 hour cyclic nature to the FTIR absorbance integrals was evident. This observation verified the result of the changing detector temperature in conjunction with the possibility of a non consistent background atmosphere. One proposed solution was to introduce an inert gas into the influent which would remain at a constant concentration throughout the experiment. Adjusting the signal strength such that the inert gas is a straight line will line up the other gas concentrations to their "true" values. Unfortunately, one of the major limitations of FTIR analysis is its inability to measure diatomic species concentrations. Therefore, the nitrogen inert added as air cannot be used as a reference. Another inert gas, unaffected by either the gold nanoparticles or the influent species must be chosen. The gas ultimately selected was methane. The results of those experiments are presented next in Section 4.3
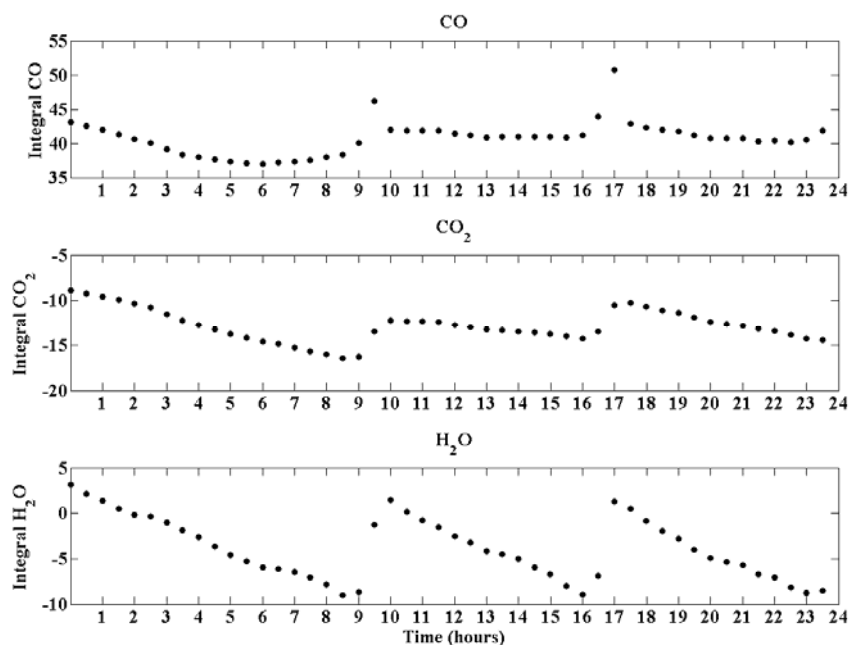
Figure 3.3  FTIR Absorbance integrals of carbon monoxide, carbon dioxide and water at $200^{o}C$.  Influent gas composition: 99 sccm $H_2$, 1 sccm CO, 50 sccm $N_2$, and 15 sccm air.
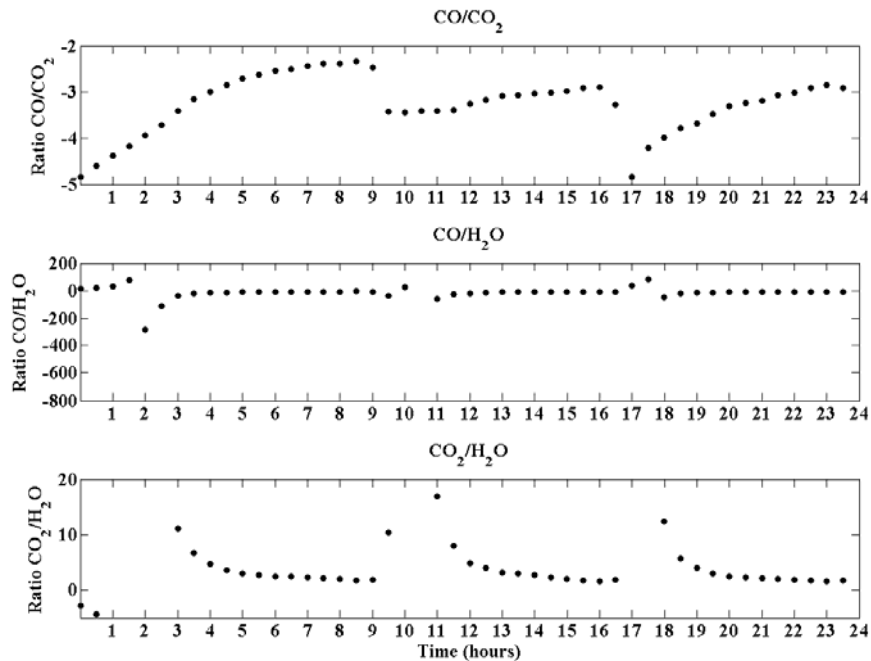


Figure 3.4  Ratios of FTIR absorbance integrals of carbon monoxide, carbon dioxide and water at $200^{o}C$.  Influent gas composition: 99 sccm $H_2$, 1 sccm CO, 50 sccm $N_2$, and 15 sccm air.
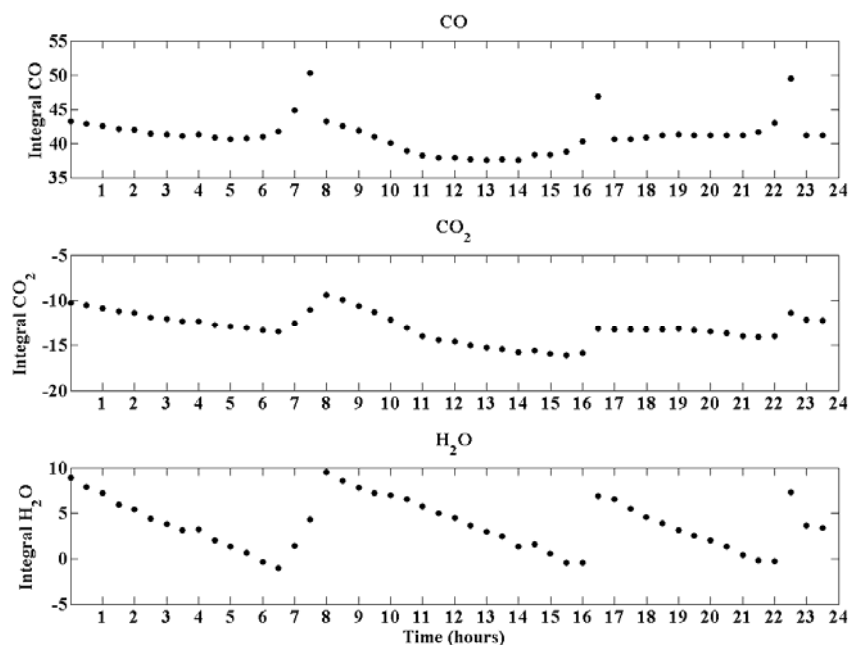
Figure 3.5  FTIR absorbance integrals of carbon monoxide, carbon dioxide and water at $300^{\circ}C$.  Influent gas composition: 99 sccm $H_2$, 1 sccm CO, 50 sccm $N_2$, and 15 sccm air.
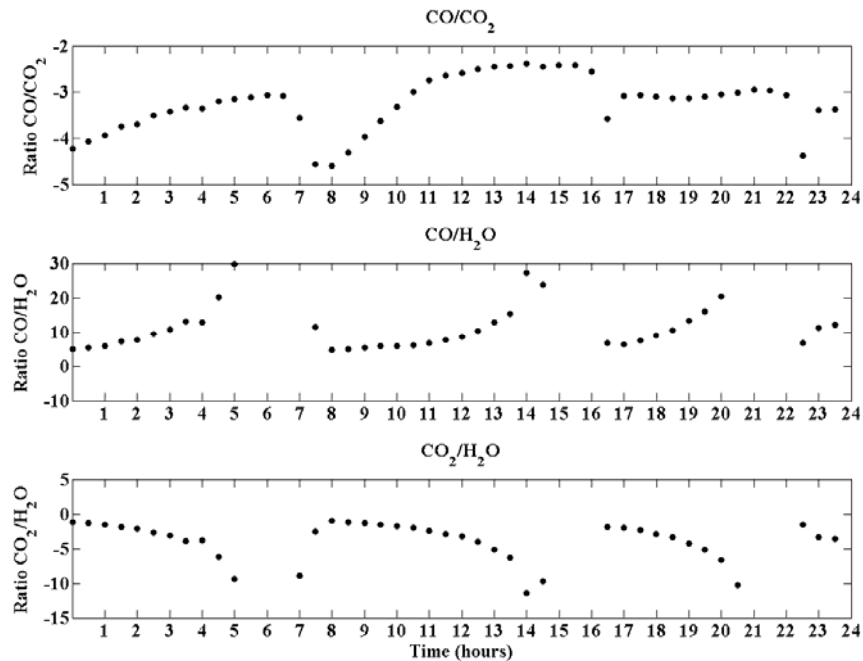


Figure 3.6  Ratios of FTIR absorbance integrals of carbon monoxide, carbon dioxide and water at $300^{\circ}C$. .  Influent gas composition: 99 sccm $H_2$, 1 sccm CO, 50 sccm $N_2$, and 15 sccm air.

41
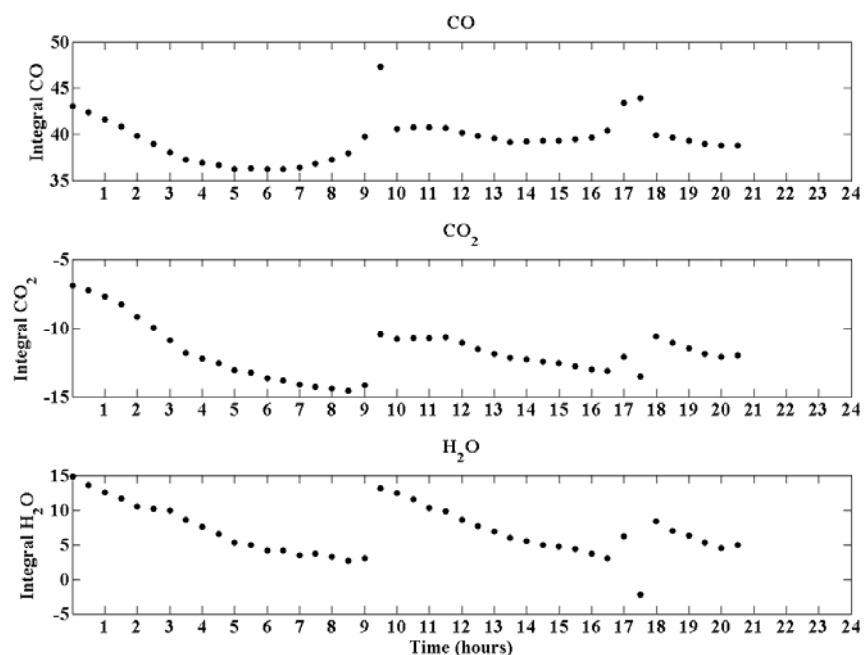
Figure 3.7  FTIR absorbance integrals of carbon monoxide, carbon dioxide and water at $425^{\circ}C$.  Influent gas composition: 99 sccm $H_2$, 1 sccm CO, 50 sccm $N_2$, and 15 sccm air.
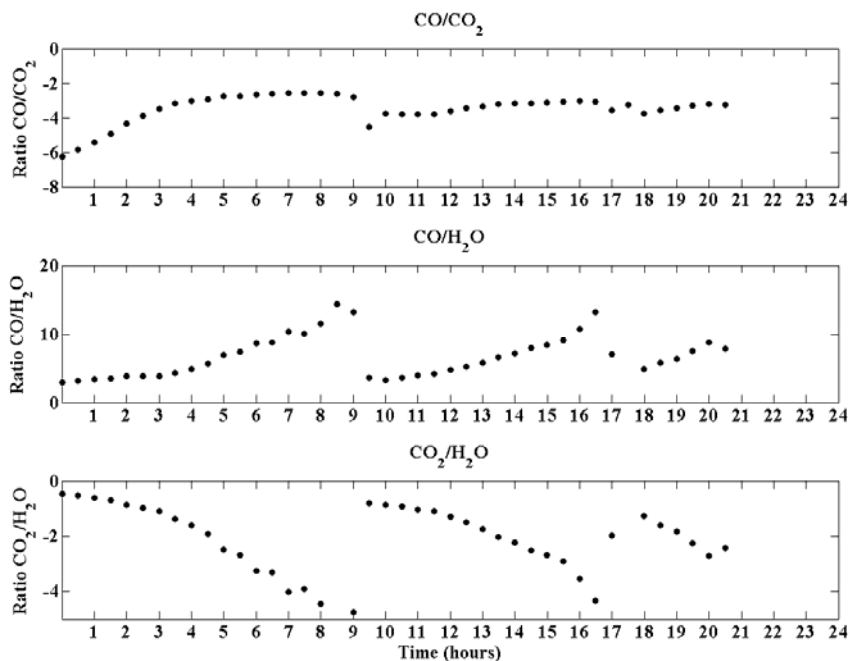


Figure 3.8  Ratios of FTIR absorbance integrals of carbon monoxide, carbon dioxide and water at $425^{\circ}C$.  Influent gas composition: 99 sccm $H_2$, 1 sccm CO, 50 sccm $N_2$, and 15 sccm air.

## 3.3    Data Analysis with Reference Methane in the Influent Stream

Although there have been some studies to oxidize methane using gold catalysts, there has been limited success in gas phase reactions.[50]   Significant reactions involving methane oxidation and gold particles have been made with liquid phase reactions utilizing selenic acid $H_2SeO_4$ as an oxidant.[50]   With no promoters available and at these temperatures, methane will pass unreacted through the catalyst bed.  This will be an excellent reference since the FTIR can easily detect the presence of the methane species.   After the introduction of 10 sccm methane into the feed stream, it appears that there is an inconsistent methane signal which was unexpected (Figure 3.9).  It is interesting to note that the methane signal follows the pattern of the carbon monoxide almost exactly.  This would suggest that the carbon monoxide is not reacting in this system since it is seems to be directly proportional to the unreactive methane.   The ratios lead to very few conclusions other than the cyclic nature of the FTIR effluent absorbance integral of each species (Figure 3.10).
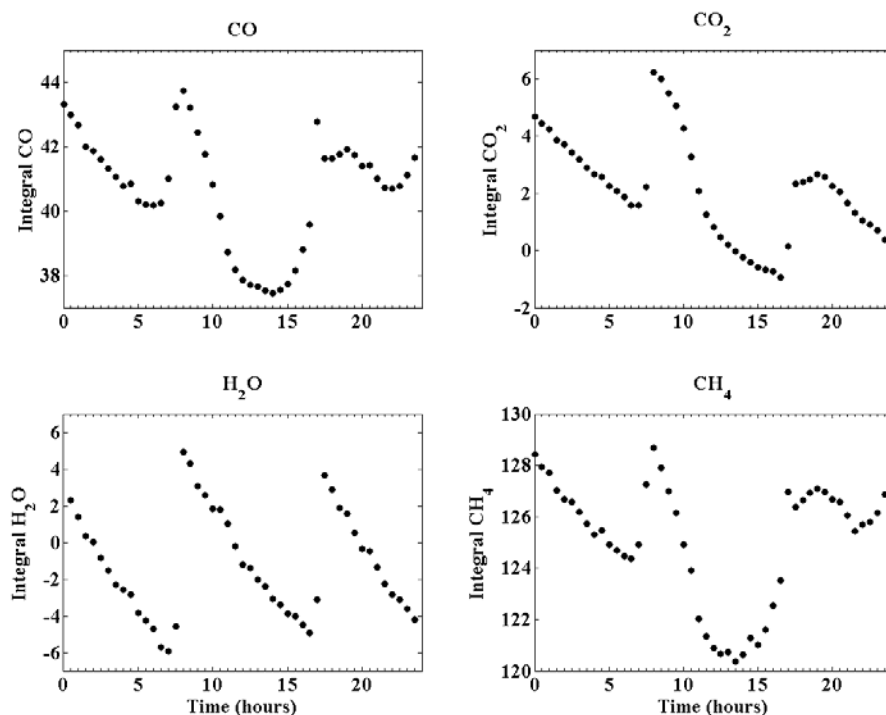


Figure 3.9  FTIR absorbance integrals of carbon monoxide, carbon dioxide, water, and methane at 425°C.  Influent gas composition: 99 sccm $H_2$, 1 sccm CO, 50 sccm $N_2$, and 15 sccm air, 10 sccm methane.

43
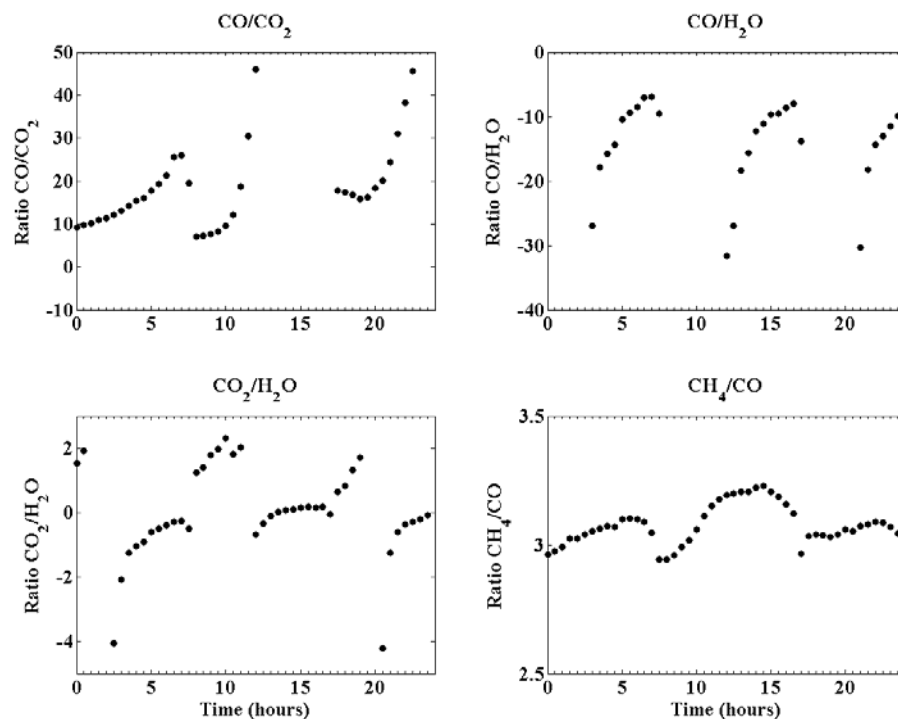
Figure 3.10  Ratios of FTIR absorbance integrals of carbon monoxide, carbon dioxide, water and methane at 425$^o$C.  Influent gas composition: 99 sccm $H_2$, 1 sccm CO, 50 sccm $N_2$, and 15 sccm air, 10 sccm methane.

## 3.4    Reevaluation of the FTIR Spectra to Account for Shifting Baselines

One observation that I have had with the last set of data runs is that the mean value of the noise level changes for each of the species as the runs proceeds through the 24 hours.  In order to accurately determine the value of the areas for each of the data points, it was suggested that I reference the initial starting point of each of the species ranges to the same point.  Since the mean value of the noise level is supposed to be zero, I chose this value as a reference.  My new evaluation procedure was a linear base line subtraction from the first point to the last point in the species evaluation range.  Given a common starting and ending point the areas should line up.  Evaluation of the integrals will then be on areas of the curves with the background subtracted.  Each curve is evaluated on an individual basis and baseline corrected.

After the baseline correction, one obvious change is noticed in Figure 3.12.  The integrals for the components actively controlled and included in the influent flatten out and

44

become relatively constant values with changes over the entire 24 hour time span approaching about 1% for both the carbon monoxide and the methane. Before the reevaluation, the changes as observed in Figure 3.11 show fluctuations approaching 20%. While the signals for the gas stream appear to be constant, the values for $CO_2$ and $H_2O$ are still cycling with the introduction of liquid nitrogen. One possible explanation of this is that the sample chamber is not under sufficient vacuum thus water vapor and carbon dioxide are merely changing due to the unavoidable experimental variations in the surrounding atmosphere around the gas cell.
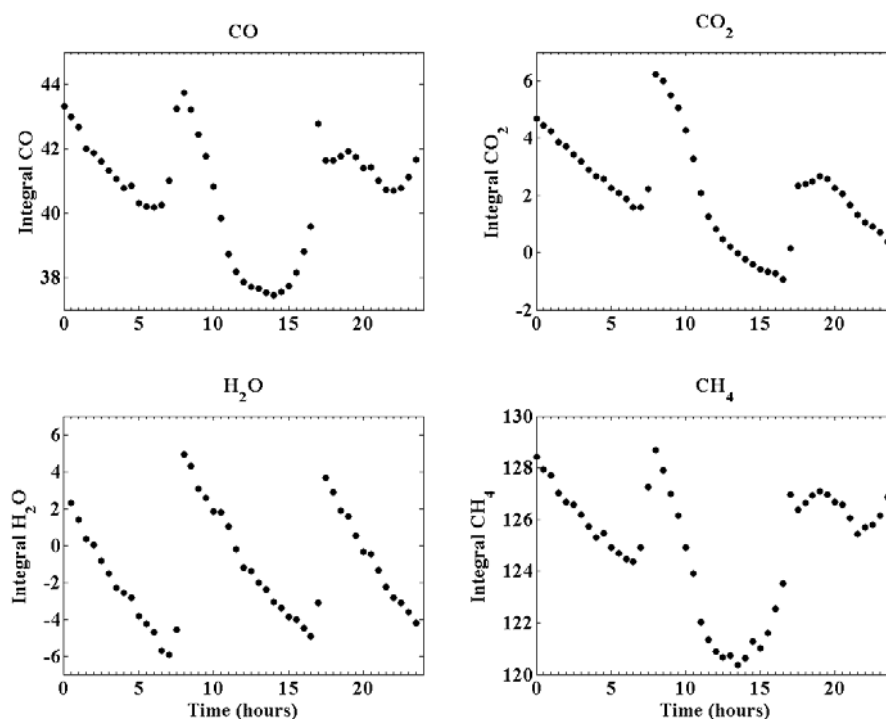


Figure 3.11 FTIR absorbance integrals of carbon monoxide, carbon dioxide, water and methane at 425°C. Influent gas composition: 99 sccm $H_2$, 1 sccm CO, 50 sccm $N_2$, and 15 sccm air, 10 sccm methane.
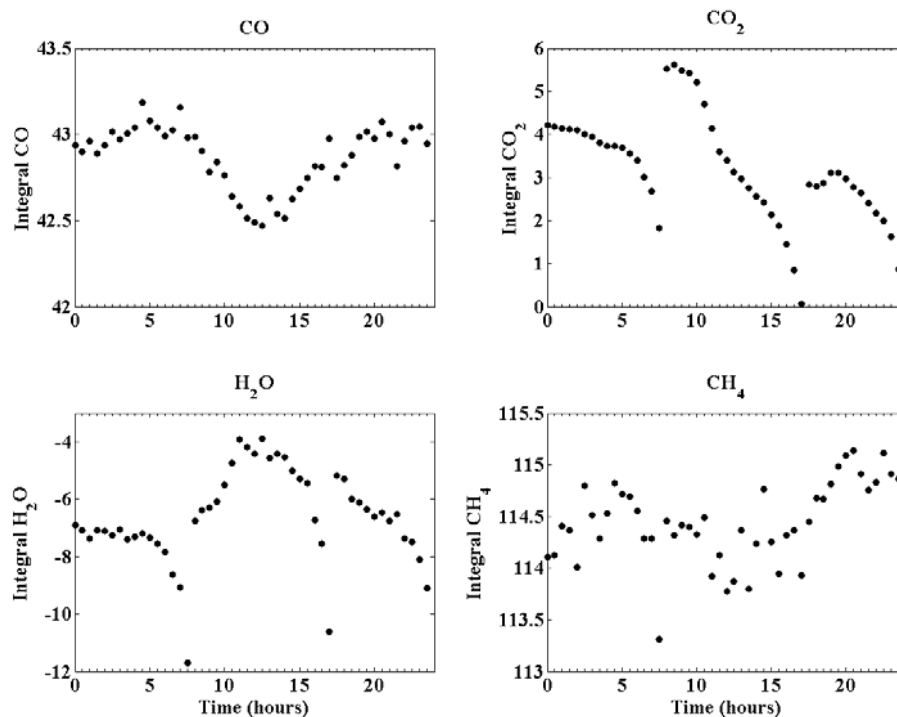
Figure 3.12 Ratios of FTIR absorbance integrals of carbon monoxide, carbon dioxide, water and methane at 425$^{\circ}$C after baseline subtraction. Influent gas composition: 99 sccm $H_2$, 1 sccm CO, 50 sccm $N_2$, and 15 sccm air, 10 sccm methane.

With this updated method of observation for the FTIR spectra, one can see if, in fact, any reactions occurring. The reevaluated CO absorbance integral for each run is presented in Figure 3.13. While there is a slight decrease in the equilibrium concentration of carbon monoxide, there does not appear to be a significant change in the reactivity of the system. A couple things to note about the two runs are that at each temperature, the concentration of CO went down as the concentration of air went up. There was not a huge difference but the trend was as hypothesized that the system may be oxygen deficient.
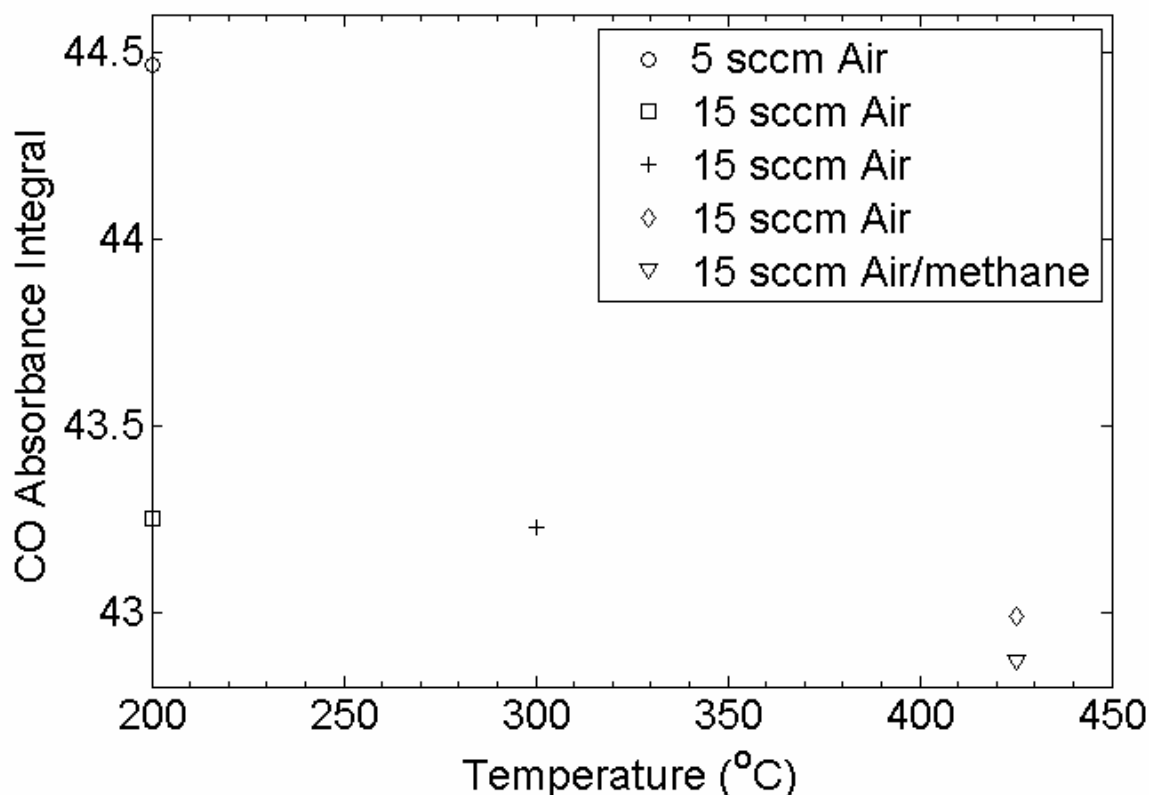
Figure 3.13  Carbon monoxide absorbance integrals for all data collected reevaluated using baseline subtraction to allow for direct comparison.

3.5    Redesign of the Supported Gold Catalyst

Results from the FTIR analysis have been less than promising for the catalysts produced. After discussions with both Dr. Gupta and David Walker from the Interfacial Phenomena and Polymeric Materials research group at USF, an improved creation method was devised to increase the adherence of the GNP to the $TiO_2$.  This improved procedure is as follows:

Walker's improved procedure begins with 0.25 mL 0.01 M aqueous solution of hydrogen tetrachloroaurate ($HAuCl_4$) added slowly to a 0.50 mL 0.01 M sodium citrate solution to stabilize the nanoparticles, 0.1 M sodium borohydride as a reduction agent, and 9 mL of water.   The solution was then stirred for 2 hr to allow the formation of GNPs. Approximately 100 mg of anatase $TiO_2$ was then added, the pH of the entire system was adjusted to 4.45, and the catalyst was continuously stirred for another 30 minutes.  An

acidic solution induces a positive charge to the surface of the $TiO_2$ which promotes the adhesion of the negatively charged GNP. After 30 minutes, the supported GNP/$TiO_2$ catalyst was evaporated and dried in a vacuum oven.

Initially, no attempt was made to expose the GNPs to excessive heat to determine if the calcination temperatures used may be resulting in deactivation. The results of the experimental run with the improved catalyst still yielded very little difference in the values between the non-reacted bypass influent absorbance integrals and the reaction effluent concentrations. Figure 3.14 shows that the absorbance integrals at each temperature and flow to be approximately equal. This correlates to a CO fractional conversion of approximately zero. Next, the catalyst was heated to 205$^o$C for 2 hours in hydrogen. This is based on TGA results which show a decrease in the catalyst weight of ~9% at 200.9$^o$C for the previous catalyst formula (Figure 3.15). The evaporating species at this temperature has yet to be identified. Again, no sizable change in the absorbance integral for carbon monoxide is observed. Only the 25$^o$C data is presented for the catalyst after exposure to the 205$^o$C reduction step because that temperature has been shown to demonstrate highest conversion in the World Gold Council catalyst samples.

3.6    Summary

The development of a FTIR effluent testing protocol which includes baseline subtraction and nitrogen purging is fully functional with both the catalyst provided by the Interfacial Phenomena and Polymeric Materials research group at USF as well as the World Gold Council. The baseline subtraction of the absorbance data to allows direct comparison of data taken under dissimilar conditions and nitrogen purging is used to eliminate background $CO_2$ and $H_2O$ contamination.

Unfortunately, the supplied two-phase-method gold catalyst has yet to show any promise for CO oxidation applications. One hypothesis for the problems is that the surfactants used to keep the gold nanoparticles from aggregating are preventing carbon monoxide transport to the surface of the particle. Another theory is that the gold may not be

adhering to the surface of the TiO$_2$ creating a cohesive metal/support interaction. Future directions for this project are discussed in Chapter 6.
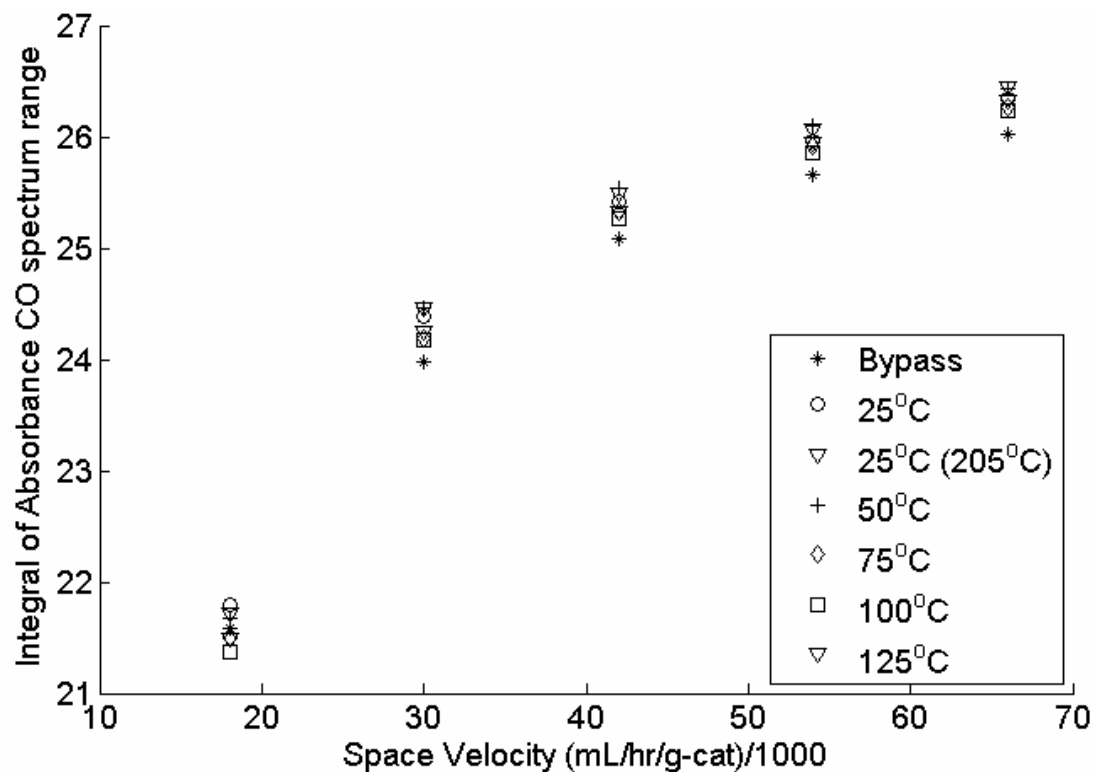


Figure 3.14 FTIR results of redesigned two-phase-method GNP catalyst before and after exposing the sample to a 205$^o$C calcination step.
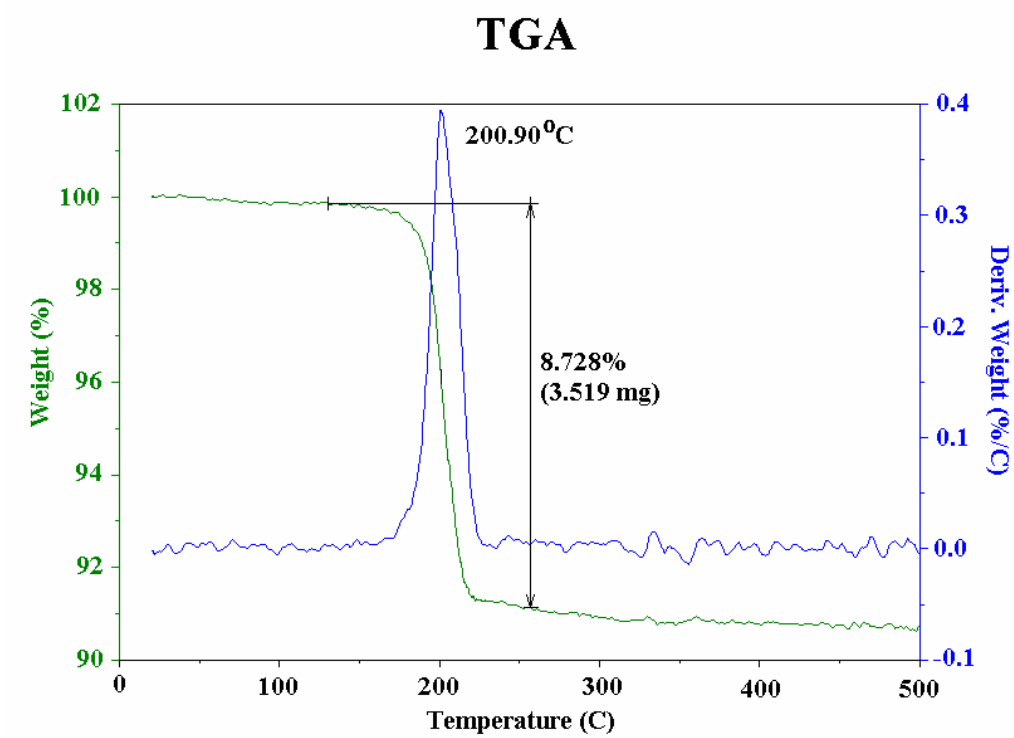
Figure 3.15  TGA analysis of original two-phase-method GNP/TiO$_2$ catalyst formula.

4 EMPIRICAL MODELS OF CARBON MONOXIDE OXIDATION VIA WORLD
GOLD COUNCIL Au/TiO$_2$ IN EXCESS HYDROGEN

## 4.1   Introduction

Numerous research groups have reported CO oxidation fractional conversion over metal oxide-supported nano-Au catalysts at temperatures below 0$^o$C of 1% CO in Air.[51,52] However, information regarding CO preferential oxidation (PROX) at temperatures above 0$^o$C is lacking. Although conceptually simple, the oxidation of CO in the presence of excess H$_2$ and CO$_2$, without oxidizing the hydrogen or remaking CO via the reverse WGS reaction, is a particularly difficult objective, which has so far only been achieved using a multistage reactor.[53]   The presence of excess CO$_2$ presents an additional problem since if the catalyst is active for the reverse water gas shift reaction then CO will be remade; this is a key feature that has limited success in this field to date.

Due to the recent growth in research on fuel cells and fuel processing, a large number of studies on CO selective or preferential oxidation (PROX) have been published.  Indeed, a comprehensive kinetic model for this catalytic system which includes the contributions of CO oxidation, H$_2$ oxidation and the WGS reaction above 0$^o$C is clearly needed.  Most recent papers are focused on catalyst formulation, characterization, and basic performance such as activity and selectivity of CO.  Few papers have investigated the kinetics and rate expressions of the reactions involved.

In this study, kinetic models are presented which predict CO fractional conversions at typical PEMFC operating conditions catalyzed by nano-Au/TiO$_2$ provided by the World Gold Council (WGC). This WGC catalyst is promoted as a benchmark for researchers to evaluate their own catalyst systems against a common reference.[7]  Although many studies have examined the extreme activity of this particular catalyst to oxidize CO at cryogenic temperatures, this study is one of the first attempts to provide a comprehensive kinetic

model of the WGC nano-Au/TiO$_2$ catalyzed PROX of CO in excess hydrogen at temperatures ranging from 25$^o$C-125$^o$C. Although these models do not take into consideration the effects of influent moisture content, this work provides some insight into the behavior of this reference catalyst and its use in possible hydrogen and direct alcohol fuel cell applications.

## 4.2    Experimental

All reactions were performed in a 24 in. quartz tube, 4 mm ID, vertical packed bed micro-reactor inside of a Lindberg/Blue split tubular furnace operating at 1 atm.  One hundred milligrams of nano-Au/TiO$_2$ powder were packed loosely between high temperature quartz wool in order to stabilize and ensure proper influent distribution through the bed.  The reactor was operated under steady state conditions at temperatures ranging from 25-125$^o$C in 25$^o$C increments.  The influent consists of a 1% CO/H$_2$ mixture with a constant 10 sccm of air.  The 1% CO/H$_2$ feed rate was varied from 20-100 sccm in 20 sccm increments.  With the air included, this corresponds to a space velocity ranging from 18000 to 66000 mL/hr/g-cat.  No attempts were made to humidify or de-humidify the influent stream.  The feed stream moisture content was assumed to be ~0%. The reaction effluent is fed directly to an inline Bio-Rad FTS 3000 Excalibur Series Fourier transform infrared spectrometer gas cell for in-situ analysis.  No attempt was made to quench any effluent reactions before entering the FTIR.  Specifications for the gas cell are given in Section 1.5.3.

## 4.3    Calculation of Thermodynamic Properties

Before examining the empirical kinetic calculations, one should determine if the given reactions are thermodynamically feasible through the analysis of Gibbs free energy.  The thermodynamic properties which determine whether or not a given reaction is favorable (spontaneous) are enthalpy and entropy.[54]  Some reactions are spontaneous because of the heat given off during the reaction ($\Delta H^o < 0$).  Other reactions are spontaneous because of an increase in the entropy or disorder of the system ($\Delta S^o > 0$).  However, sometimes, one property may be favorable while another is not.  Another term had to be defined which reflects the balance between the heat of reaction and the change in entropy.  This value is

known as the Gibbs free energy and is defined as the enthalpy of the system minus the product of the temperature times the entropy of the system.[54]  A negative Gibbs free energy indicates a favorable, spontaneous reaction and is most useful for thermo-chemical processes at constant temperature (isothermal) and pressure (isobaric).[54]

Calculations of both the heat of reaction and the Gibbs free energy at room temperature for each reaction are given in Table 4.1.  All data for these calculations were obtained from Appendix C in *Introduction to Chemical Engineering Thermodynamics*.[54]  These calculations show that CO oxidation, $H_2$ oxidation and the WGS are spontaneous while the RWGS is not based on the sign of the calculated Gibbs free energy of reaction.

Table 4.1  Standard heats of reaction and Gibbs free energies of reaction.

|  | $\Delta H^o_{298\,K}$ (kJ/mol) | $\Delta G^o_{298\,K}$ (kJ/mol) |
|---|---|---|
| $CO + O_2 \rightarrow CO_2$ | -283 | -257 |
| $H_2 + O_2 \rightarrow H_2O_{(g)}$ | -242 | -228 |
| $CO + H_2O \rightarrow CO_2 + H_2$ | -41.2 | -28.6 |
| $CO_2 + H_2 \rightarrow CO + H_2O$ | 41.2 | 28.6 |

There is very little change in the calculated values of the Gibbs energy of reaction over the temperature range evaluated in these studies ($25^o$C-$125^o$C) (Table 4.2).  Based on equations outlined in Smith and Van Ness[54], the equilibrium constants are shown in Table 4.3.  The equilibrium constant is another indication of the extent and direction of the given reactions.  A large value indicates the formation of the products in that reaction.  Again, this validates the spontaneous reaction of CO oxidation, $H_2$ oxidation, and the WGS.

Table 4.2  Gibbs free energies of reaction at each temperature.

| | $\Delta G^o_{298\ K}$ (kJ/mol) | $\Delta G^o_{323\ K}$ (kJ/mol) | $\Delta G^o_{348\ K}$ (kJ/mol) | $\Delta G^o_{373\ K}$ (kJ/mol) | $\Delta G^o_{398\ K}$ (kJ/mol) |
|---|---|---|---|---|---|
| $CO + O_2 \rightarrow CO_2$ | -257 | -255 | -253 | -251 | -248 |
| $H_2 + O_2 \rightarrow H_2O_{(g)}$ | -228 | -227 | -226 | -225 | -224 |
| $CO + H_2O \rightarrow CO_2 + H_2$ | -28.6 | -27.8 | -26.5 | -25.5 | -24.4 |
| $CO_2 + H_2 \rightarrow CO + H_2O$ | 28.6 | 27.8 | 26.5 | 25.5 | 24.4 |

Table 4.3  Calculated equilibrium constants at each temperature.

| | $K_{298\ K}$ | $K_{323\ K}$ | $K_{348\ K}$ | $K_{373\ K}$ | $K_{398\ K}$ |
|---|---|---|---|---|---|
| $CO + O_2 \rightarrow CO_2$ | $1.21 \times 10^{45}$ | $1.76 \times 10^{41}$ | $9.01 \times 10^{37}$ | $1.27 \times 10^{35}$ | $4.09 \times 10^{32}$ |
| $H_2 + O_2 \rightarrow H_2O_{(g)}$ | $1.17 \times 10^{40}$ | $6.06 \times 10^{36}$ | $9.17 \times 10^{33}$ | $3.27 \times 10^{31}$ | $2.33 \times 10^{29}$ |
| $CO + H_2O \rightarrow CO_2 + H_2$ | 104000 | 28800 | 9620 | 3730 | 1640 |
| $CO_2 + H_2 \rightarrow CO + H_2O$ | $9.6 \times 10^{-6}$ | $3.47 \times 10^{-5}$ | $1.03 \times 10^{-4}$ | $2.68 \times 10^{-4}$ | $6.10 \times 10^{-4}$ |

## 4.4   Empirical Models

The next sections examine the potential of empirical models to predict the effluent concentrations of CO oxidation over the WGC nano-Au/TiO$_2$ at various temperatures and space velocities.  Matlab code for each model can be found in Appendix A.

## 4.5   Elementary CO Oxidation Single Reaction Model

Based on previous studies at cryogenic temperatures[55], a simple elementary reaction model was chosen first to predict the carbon monoxide oxidation reaction parameters (Eqn. 4.1): activation energy (E) and pre-exponential factor ($\alpha$).  This model assumes an elementary reaction order; a steady state, isothermal, isobaric reaction; Arrhenius reaction rate constants, and ignores the contribution from the water gas shift and hydrogen oxidation reactions.

Table 4.4 Experimental influent conditions to the tubular reactor.

| | | | | | |
|---|---|---|---|---|---|
| Flowrate Air (sccm) | 10 | 10 | 10 | 10 | 10 |
| Flowrate 1% CO/H$_2$ (sccm) | 20 | 40 | 60 | 80 | 100 |
| Flowrate O$_2$ (sccm) | ~2 | ~2 | ~2 | ~2 | ~2 |
| Flowrate CO (sccm) | 0.2 | 0.4 | 0.6 | 0.8 | 1 |
| Space Velocity (mL/hr/g-cat) | 18000 | 30000 | 42000 | 54000 | 66000 |
| $\theta_{O_2} = F_{O2}/F_{CO}$ | 10 | 5 | 3.33 | 2.5 | 2 |
| $\varepsilon *10^3$ | -3.33 | -4 | -4.28 | -4.44 | -4.54 |

$$CO + \frac{1}{2}O_2 \rightarrow CO_2 \tag{4.1}$$

Utilizing the design equation of a packed bed reactor, the following Eqns. 4.2-5 can be formulated to determine CO conversion.

$$F_{CO^o}\frac{\partial X}{\partial W} = -r_{CO}' = kC_{CO}C_{O_2}^{\frac{1}{2}} \tag{4.2}$$

$$k = \alpha \exp^{\left(-\frac{E}{RT}\right)} \tag{4.3}$$

$$f(X) = \int_0^X \left[ \frac{(1-\varepsilon X)^{\frac{3}{2}}}{C_{CO^o}^{\frac{3}{2}}(1-X)(\theta_{O_2} - \frac{1}{2}X)^{\frac{1}{2}}} \right] dX \tag{4.4}$$

$$\ln(\alpha) - \frac{E}{RT} = \ln\left( \frac{F_{CO^o}f(X)}{W} \right) \tag{4.5}$$

A graph of $\ln\left( \dfrac{F_{CO^o}f(X)}{W} \right)$ vs. T$^{-1}$ should yield a slope of -E/R and a y-intercept of $\ln(\alpha)$

if the system can be modeled as a single elementary reaction.

### 4.5.1 Elementary CO Oxidation Single Reaction Model Results

The FTIR CO absorbance integral (2145-2230 cm$^{-1}$) of both an unreacted reference (A$_{REF}$) and after reaction (A$_{RXN}$) were used to calculate CO experimental conversion

defined as $(A_{REF} - A_{RXN})/A_{REF}$. These results are displayed in Table 4.5. The plot of $\ln\left(\dfrac{F_{CO^o}f(X)}{W}\right)$ vs. $T^{-1}$ led to a completely non-linear plot which does not allow an accurate estimation of either the activation or of the pre-exponential factor (Figure 4.1). This plot shows that the carbon monoxide preferential oxidation reaction is non-elementary in nature at these conditions and the effluent CO concentrations cannot be modeled by evaluating a single elementary CO oxidation reaction. A more comprehensive model which includes the contributions of the $H_2$ oxidation and WGS reaction is necessary.

Table 4.5  Experimental reaction effluent fractional conversions at each temperature and flow rate.

|  | 25°C | 50°C | 75°C | 100°C | 125°C |
|---|---|---|---|---|---|
| (20 sccm 1%CO/H$_2$)/100 mg | 0.3062 | 0.0371 | 0.0026 | 0.0057 | 0.0081 |
| (40 sccm 1%CO/H$_2$)/100 mg | 0.1546 | 0.0702 | 0.0032 | 0.0898 | 0.0041 |
| (60 sccm 1%CO/H$_2$)/100 mg | 0.0338 | 0.0218 | 0.0030 | 0.0851 | 0.0020 |
| (80 sccm 1%CO/H$_2$)/100 mg | 0.0312 | 0.0177 | 0.0021 | 0.0017 | 0.0015 |
| (100 sccm 1%CO/H$_2$)/100 mg | 0.0237 | 0.0153 | 0.0014 | 0.0023 | 0.0015 |
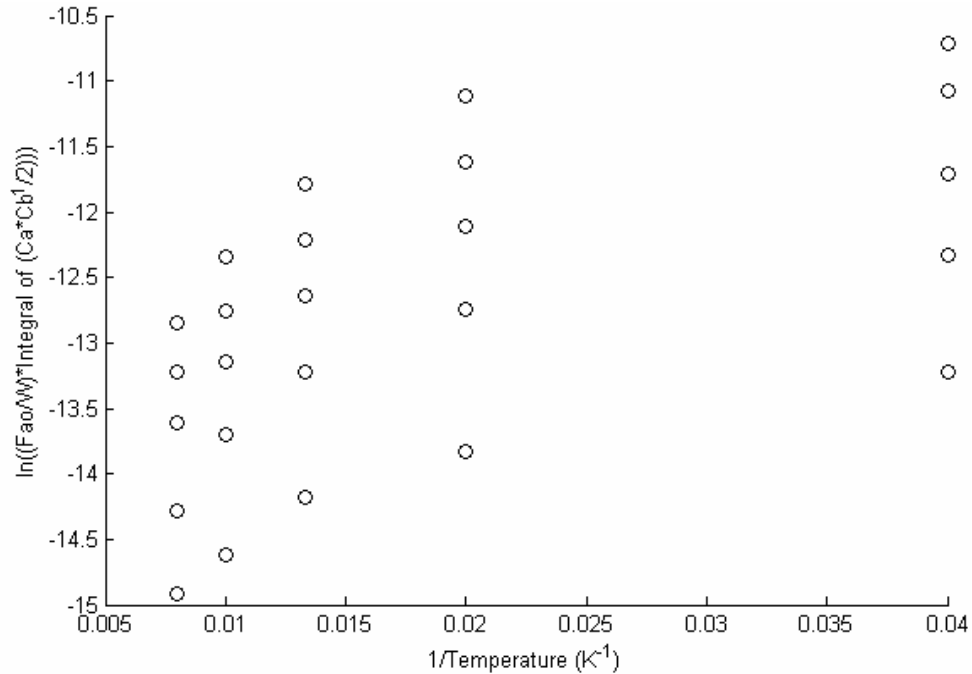


Figure 4.1  Graph of $\ln\left(\dfrac{F_{CO^o}f(X)}{W}\right)$ vs. $T^{-1}$ for the simple elementary model.

The calculated error for each fractional conversion is shown in Table 4.6. This calculation is based on the mean and standard deviation of the FTIR reference and reaction integrals. Each sample was collected four times at each temperature and space velocity. Propagation of error based on sampling accuracy has not been included. The calculations of error are included in Appendix A.

Table 4.6  Calculated error with each fractional conversion value.

|  | 25°C | 50°C | 75°C | 100°C | 125°C |
|---|---|---|---|---|---|
| (20 sccm 1%CO/H$_2$)/100 mg | 0.55 | 0.40 | 0.32 | 0.33 | 0.28 |
| (40 sccm 1%CO/H$_2$)/100 mg | 0.42 | 0.35 | 0.27 | 0.24 | 0.16 |
| (60 sccm 1%CO/H$_2$)/100 mg | 0.37 | 0.34 | 0.24 | 0.20 | 0.14 |
| (80 sccm 1%CO/H$_2$)/100 mg | 0.40 | 0.35 | 0.24 | 0.17 | 0.12 |
| (100 sccm 1%CO/H$_2$)/100 mg | 0.47 | 0.42 | 0.33 | 0.17 | 0.11 |

4.6    Comprehensive PROX Models

After being unable to model the effluent concentrations using a single reaction, a more comprehensive model set was examined. The following two kinetic models utilize all of the primary reactions in the PROX of CO (CO oxidation (Eqn. 4.6.a), H$_2$ oxidation (Eqn. 4.6.b), and the WGS/RWGS reactions (Eqn. 4.7.a-b)). These sets of experiments are based on similar work examining CO oxidation via Pt/TiO$_2$.[8]  In both models, the values of the kinetic model's pre-exponentials and activation energies were determined by minimizing the sum of the square of the difference between predicted and experimental CO conversion via nonlinear least squares fitting (LSQCURVEFIT) in Matlab.[56]  All Matlab code for these models is provided with this text. The predicted CO conversion was calculated by solving the kinetic model's ordinary differential equations by the fourth order Runge-Kutta method and compared to experimental FTIR conversion data. A flow diagram of the kinetic model path is shown in Figure 4.2.

$$CO + \frac{1}{2}O_2 \rightarrow CO_2 \qquad\qquad H_2 + \frac{1}{2}O_2 \rightarrow H_2O \qquad\qquad\qquad (4.6.a\text{-}b)$$

$$CO_2 + H_2 \rightarrow CO + H_2O \qquad\qquad CO + H_2O \rightarrow CO_2 + H_2 \qquad\qquad (4.7.a\text{-}b)$$

Define Constants and Variables

Flow rates, Temperature, Experimental FTIR CO Conversion Results

Define the mole balance equations for each component

Is this an elementary or non-elementary reaction?

Select starting values and any boundary conditions

New Model Variables

Compute model's conversions

Does the model's predicted values far within tolerance?

NO

Adjust the variables to minimize the Least Squares Error

YES

Output Empirical Values

Figure 4.2  Kinetic model flow diagram.

## 4.7    Comprehensive Elementary Reaction Model

After defining the total molar flow rate of the gas stream as the sum of the components (Eqn. 4.8), the concentration of the individual species are calculated as the mole fraction times the total concentration (Eqn. 4.9).  This model assumes elementary reaction orders of all components (Eqns. 4.10.a-b, 4.11.a-b); isothermal, isobaric reactions; and Arrhenius reaction rate constants, and steady state operation.  After describing the mole balances for each reaction (Eqns. 4.12.a-b, 4.13.a-b, and 4.14.a-b), fractional conversion can be predicted and compared to the experimental data.  Fractional conversion of CO is defined as $(F_{CO}{}^{o} - F_{CO@W=100mg})/ F_{CO}{}^{o}$.

$$F_{Total} = F_{CO} + F_{O_2} + F_{CO_2} + F_{H_2} + F_{H_2O} + F_{N_2} \tag{4.8}$$

$$C_{xx} = C_{Total}^{o} * \frac{F_{xx}}{F_{Total}} \tag{4.9}$$

$$r_1 = -k_1 C_{CO} C_{O_2}{}^{\frac{1}{2}} \qquad\qquad r_2 = -k_2 C_{H_2} C_{O_2}{}^{\frac{1}{2}} \tag{4.10.a-b}$$

$$r_3 = -k_3 C_{CO_2} C_{H_2} \qquad\qquad r_4 = -k_4 C_{CO} C_{H_2O} \qquad\qquad (4.11.\text{a-b})$$

$$\frac{dF_{CO}}{dW} = r_1 - r_3 + r_4 \qquad\qquad \frac{dF_{O_2}}{dW} = \frac{1}{2}r_1 + \frac{1}{2}r_2 \qquad\qquad (4.12.\text{a-b})$$

$$\frac{dF_{CO_2}}{dW} = -r_1 + r_3 - r_4 \qquad\qquad \frac{dF_{H_2}}{dW} = r_2 + r_3 - r_4 \qquad\qquad (4.13.\text{a-b})$$

$$\frac{dF_{H_2O}}{dW} = -r_2 - r_3 + r_4 \qquad\qquad \frac{dF_{N_2}}{dW} = 0 \qquad\qquad (4.14.\text{a-b})$$

## 4.8 Comprehensive Non-Elementary Reaction Model

The non-elementary kinetic model also assumes steady state, isothermal, isobaric reactions, and Arrhenius reaction rate constants. However, this model removes the constraints of elementary reaction orders. All steps are repeated as in the elementary reaction except Eqns. 4.15.a-b and Eqns. 4.16.a-b replace Eqns 4.10.a-b and Eqns 4.11.a-b and the concentration dependence (reaction order) for each is evaluated. Fractional conversions are then predicted and compared to the experimental data.

$$r_1 = -k_1 C_{CO}{}^{Exp_1} C_{O_2}{}^{Exp_2} \qquad\qquad r_2 = -k_2 C_{H_2}{}^{Exp_1} C_{O_2}{}^{Exp_2} \qquad\qquad (4.15.\text{a-b})$$

$$r_3 = -k_3 C_{CO_2}{}^{Exp_1} C_{H_2}{}^{Exp_2} \qquad\qquad r_4 = -k_4 C_{CO}{}^{Exp_1} C_{H_2O}{}^{Exp_2} \qquad\qquad (4.16.\text{a-b})$$

## 4.9 Comparison of Comprehensive Models to Experimental Results

At lower temperatures ($25^\circ$C and $50^\circ$C), the CO fractional conversions did not follow as smooth a curve as expected between flow rates. One hypothesis is that the reacting system is in a transitional state between dominance by the carbon monoxide oxidation regime and one dominated by hydrogen oxidation and the WGS reaction. Another theory is that the production of liquid water may be hindering the catalyst at these lower temperatures.[52,57] It is interesting to note that the highest CO conversion occurred at the lowest temperature and flow rate which seems counter intuitive to initial thoughts that CO conversion would increase with increasing temperature as seen in previous cryogenic studies.[55]

### 4.9.1 Comprehensive Elementary Reaction Model Results

As shown in Figure 4.3, the elementary model does not accurately depict the CO fractional conversions experimentally determined. The empirical parameters found are listed in Table 4.7. These calculations revealed that the CO concentrations cannot be modeled given the elementary reaction order restraints. Using equations 4.12.a-b, 4.13.a-b, and 4.14.a-b along with Table 4.7 yields the empirical mole balances found in Table 4.8.

Table 4.7  Calculated pre-exponentials and activation energies for the elementary model which includes CO oxidation, $H_2$ oxidation and the WGS reaction.

|  | Pre-exponential | Activation Energy (kJ/mol) |
|---|---|---|
| $r_1 = -k_1 C_{CO} C_{O_2}^{\frac{1}{2}}$ | 683 | ~0 |
| $r_2 = -k_2 C_{H_2} C_{O_2}^{\frac{1}{2}}$ | 1350 | 6.8 |
| $r_3 = -k_3 C_{CO_2} C_{H_2}$ | 1890 | 3.6 |
| $r_4 = -k_4 C_{CO} C_{H_2O}$ | 0.126 | 43.0 |

Table 4.8  Empirical mole balances for the elementary model which includes CO oxidation, $H_2$ oxidation and the WGS reaction.

$$\frac{dF_{CO}}{dW} = -683 * C_{CO} C_{O_2}^{\frac{1}{2}} + 1890 * \exp(-3.6/RT) * C_{CO_2} C_{H_2}$$
$$-0.126 * \exp(-43.0/RT) * C_{CO} C_{H_2O}$$

$$\frac{dF_{CO_2}}{dW} = 683 * C_{CO} C_{O_2}^{\frac{1}{2}} - 1890 * \exp(-3.6/RT) * C_{CO_2} C_{H_2}$$
$$+0.126 * \exp(-43.0/RT) * C_{CO} C_{H_2O}$$

$$\frac{dF_{H_2O}}{dW} = 1350 * \exp(-6.8/RT) * C_{H_2} C_{O_2}^{\frac{1}{2}} + 1890 * \exp(-3.6/RT) * C_{CO_2} C_{H_2}$$
$$-0.126 * \exp(-43.0/RT) * C_{CO} C_{H_2O}$$

Table 4.7 (Continued)

$$\frac{dF_{O_2}}{dW} = -\frac{1}{2} * 683 * C_{CO} C_{O_2}{}^{\frac{1}{2}} - \frac{1}{2} * 1350 * \exp(-6.8/RT) * C_{H_2} C_{O_2}{}^{\frac{1}{2}}$$

$$\frac{dF_{H_2}}{dW} = -1350 * \exp(-6.8/RT) * C_{H_2} C_{O_2}{}^{\frac{1}{2}} - 1890 * \exp(-3.6/RT) * C_{CO_2} C_{H_2}$$
$$+ 0.126 * \exp(-43.0/RT) * C_{CO} C_{H_2O}$$
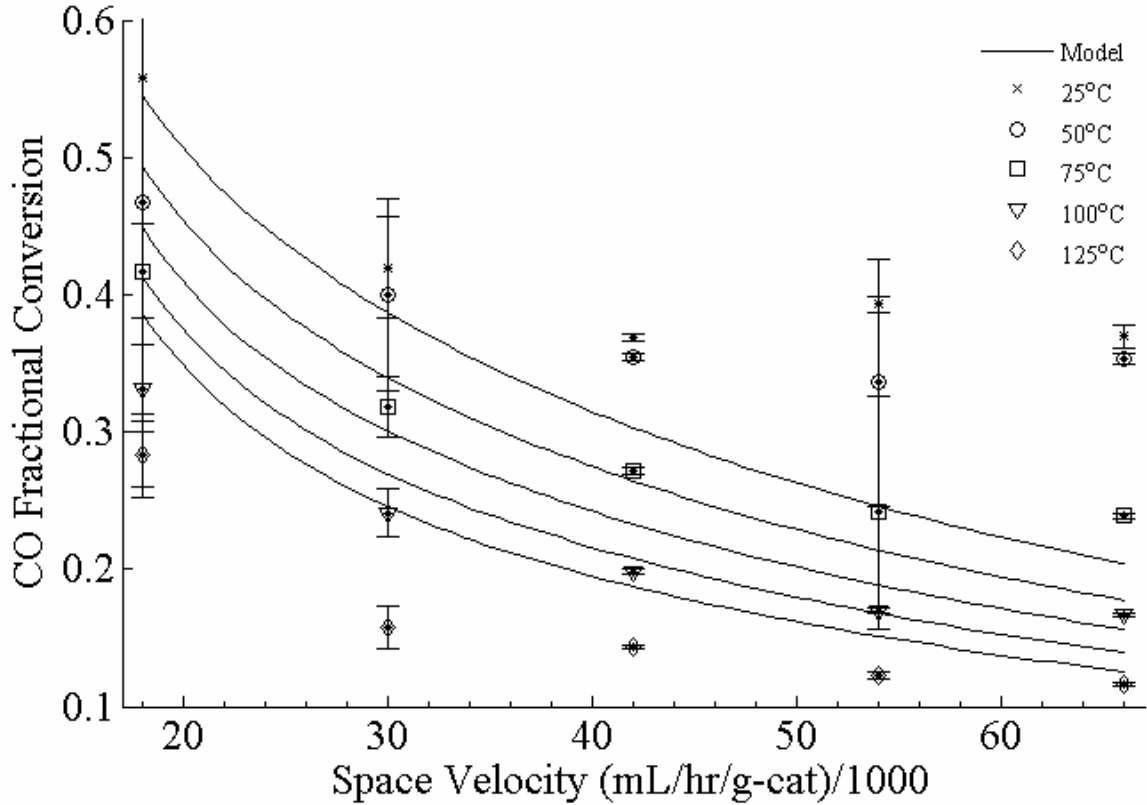


Figure 4.3 Comparison of model results for the comprehensive elementary model.

4.9.2   Comprehensive Non-Elementary Reaction Model Results

After removing the restrictions of elementary reaction orders for each of the concentrations, Figure 4.4 shows that there is an accurate representation of the effluent concentrations predicted by the non-elementary kinetic model. The model parameters are displayed in Table 4.9. This kinetic model calculated positive values for all activation energies, and pre-exponentials. This allows comparisons to literature values for similar reaction mechanisms.

61

After comparing these results to those found by Haruta for CO oxidation over the identical catalyst for 1% CO in air, there appears to be some correlation. Haruta discovered that the activation energy of the carbon monoxide reaction approached zero as one approaches standard temperatures and pressures ($25^{o}$C, 1 atm) from cryo temperatures.[31] While the empirically derived value in this model is not zero, the activation energy of the CO oxidation reaction is significantly lower than the other reactions, resulting in less temperature dependence than all of the other reactions. He also found that the oxygen reaction order for CO oxidation to be between 0-0.25 which correlates well with the 0.15 reaction order calculated.[31] However, he also found that the CO reaction order for CO oxidation to be ~0.[31] This does not match well with 0.91 I calculated. It is speculated that the difference in the reaction order is due to the synergistic combination of the four reactions and the possibility of CO being reformed due to the RWGS reaction. Since in his experiments, Haruta did not have any $H_2$ in the feed stream, there are no comparable numbers for the hydrogen oxidation or WGS/RWGS reactions.

Table 4.9  Calculated pre-exponentials and activation energies for the non-elementary model which includes CO oxidation, $H_2$ oxidation and the WGS reaction.

| | Pre-exponential | Activation Energy (kJ/mol) | $EXP_1$ | $EXP_2$ |
|---|---|---|---|---|
| $r_1 = -k_1 C_{CO}^{Exp_1} C_{O_2}^{Exp_2}$ | 99.0 | 0.4 | 0.91 | 0.15 |
| $r_2 = -k_2 C_{H_2}^{Exp_1} C_{O_2}^{Exp_2}$ | 100.8 | 9.6 | 0.96 | 0.13 |
| $r_3 = -k_3 C_{CO_2}^{Exp_1} C_{H_2}^{Exp_2}$ | 117.4 | 8.3 | 0.38 | 0.80 |
| $r_4 = -k_4 C_{CO}^{Exp_1} C_{H_2O}^{Exp_2}$ | 109.0 | 8.7 | 0.75 | 0.51 |

Table 4.10  Empirical mole balances for the non-elementary model which includes CO oxidation, $H_2$ oxidation and the WGS reaction.

$$\frac{dF_{CO}}{dW} = -99.0 * \exp(-0.4/RT) * C_{CO}^{0.91} C_{O_2}^{0.15} + 117.4 * \exp(-8.3/RT) * C_{CO_2}^{0.38} C_{H_2}^{0.80}$$

$$-109.0 * \exp(-8.7/RT) * C_{CO}^{0.75} C_{H_2O}^{0.51}$$

Table 4.9  (Continued)

$$\frac{dF_{CO_2}}{dW} = 99.0*\exp(-0.4/RT)*C_{CO}{}^{0.91}C_{O_2}{}^{0.15} - 117.4*\exp(-8.3/RT)*C_{CO_2}{}^{0.38}C_{H_2}{}^{0.80}$$
$$+109.0*\exp(-8.7/RT)*C_{CO}{}^{0.75}C_{H_2O}{}^{0.51}$$

$$\frac{dF_{H_2O}}{dW} = 100.8*\exp(9.6/RT)*C_{H_2}{}^{0.96}C_{O_2}{}^{0.13} + 117.4*\exp(-8.3/RT)*C_{CO_2}{}^{0.38}C_{H_2}{}^{0.80}$$
$$-109.0*\exp(-8.7/RT)*C_{CO}{}^{0.75}C_{H_2O}{}^{0.51}$$

$$\frac{dF_{O_2}}{dW} = -\frac{1}{2}*99.0*C_{CO}{}^{0.91}C_{O_2}{}^{0.15} - \frac{1}{2}*100.8*\exp(-6.8/RT)*C_{H_2}{}^{0.96}C_{O_2}{}^{0.13}$$

$$\frac{dF_{H_2}}{dW} = -100.8*\exp(-9.6/RT)*C_{H_2}{}^{0.96}C_{O_2}{}^{0.13} - 117.4*\exp(-8.3/RT)*C_{CO_2}{}^{0.38}C_{H_2}{}^{0.80}$$
$$+109.0*\exp(-8.7/RT)*C_{CO}{}^{0.75}C_{H_2O}{}^{0.51}$$
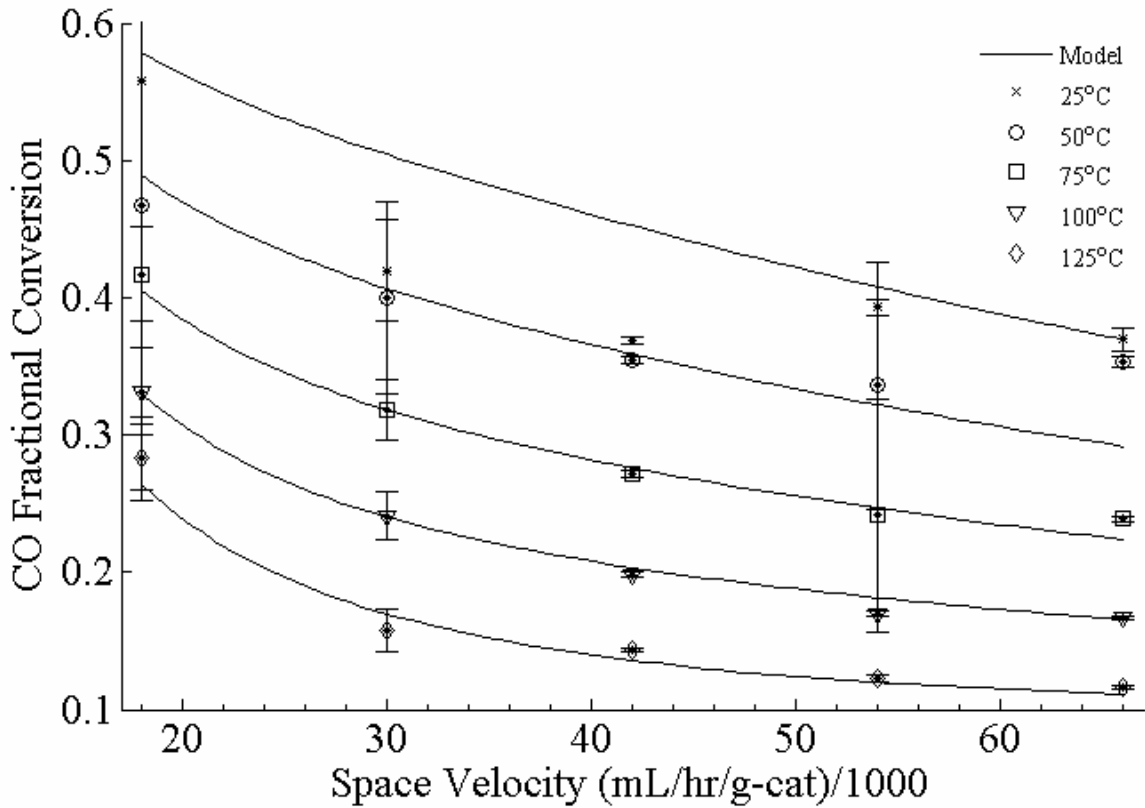


Figure 4.4  Comparison of model results for the comprehensive non-elementary model.

## 4.10 Linearly Independent Model Equations for CO Oxidation

The preceding models in Sections 0-4.9 were based on similar research by Choi et al. for CO oxidation via $Pt/TiO_2$.[8]  However, after examination of the four reactions in Eqns. 6.a-b and 7.a-b, one can see that the CO oxidation, $H_2$ oxidation and WGS/RWGS reactions are not linearly independent.  Equation 6.a minus equation 6.b equals the water gas shift reaction (Equation 7.b).  Also, the WGS/RWGS reactions are not linearly independent of themselves.  Removing the hydrogen oxidation reaction (Eqn. 4.6.b) and restraining the reaction rate constants to be dependent on each based on the equilibrium constants calculated in Table 4.3 allows the system to modeled by a set of linearly independent reactions as shown in Equations 4.17-19.  In the linearly independent elementary model, only four variables are undefined, $\alpha_1$, $E_1$, $\alpha_2$ and $E_2$.  All previous assumptions (isothermal, isobaric reactions, Arrhenius reaction rate constants, and steady state operation) are still valid.  For the non-elementary linearly independent kinetic model, the reaction orders will be undefined brings the total number of variables to ten: $\alpha_1$, $E_1$, $\alpha_2$, $E_2$, and six reaction orders.

$$r_1 = -k_1 C_{CO} C_{O_2}^{\frac{1}{2}} \tag{4.17}$$

$$r_2 = -k_2 C_{CO_2} C_{H_2} \tag{4.18}$$

$$r_3 = -k_2 * K_{298\,K\,(RWGS)} * C_{CO} C_{H_2O} \tag{4.19}$$

### 4.10.1 Linearly Independent Elementary Reaction Model Results

Results for linearly independent elementary model once again fail to accurately depict the effluent CO concentrations.  The values of the pre-exponentials and activations energies for the closest fit are shown in Table 4.11-11 and the graphed in Figure 4.5.

Table 4.11 Calculated pre-exponentials and activation energies for the linearly independent elementary model reaction.

|  | Pre-exponential | Activation Energy (kJ/mol) |
|---|---|---|
| $r_1 = -k_1 C_{CO} C_{O_2}^{\frac{1}{2}}$ | 231 | $5.8 \times 10^{-5}$ |
| $r_2 = -k_2 C_{CO_2} C_{H_2}$ | 957 | $2.97 \times 10^{-3}$ |

Table 4.12 Empirical mole balances for the linearly independent elementary model reaction.

$$\frac{dF_{CO}}{dW} = -231 * \exp(-5.8x10^{-5}/RT) * C_{CO} C_{O_2}^{\frac{1}{2}} + 957 * \exp(-2.97x10^{-3}/RT) * C_{CO_2} C_{H_2}$$
$$-957 * \exp(-2.97x10^{-3}/RT) * K_{298\,K\,(RWGS)} * C_{CO} C_{H_2O}$$

$$\frac{dF_{CO_2}}{dW} = +231 * \exp(-5.8x10^{-5}/RT) * C_{CO} C_{O_2}^{\frac{1}{2}} - 957 * \exp(-2.97x10^{-3}/RT) * C_{CO_2} C_{H_2}$$
$$+957 * \exp(-2.97x10^{-3}/RT) * K_{298\,K\,(RWGS)} * C_{CO} C_{H_2O}$$

$$\frac{dF_{H_2O}}{dW} = +957 * \exp(-2.97x10^{-3}/RT) * C_{CO_2} C_{H_2}$$
$$-957 * \exp(-2.97x10^{-3}/RT) * K_{298K\,(RWGS)} * C_{CO} C_{H_2O}$$

$$\frac{dF_{O_2}}{dW} = -\frac{1}{2} * 231 * \exp(-5.8x10^{-5}/RT) * C_{CO} C_{O_2}^{\frac{1}{2}}$$

$$\frac{dF_{H_2}}{dW} = -957 * \exp(-2.97x10^{-3}/RT) * C_{CO_2} C_{H_2}$$
$$+957 * \exp(-2.97x10^{-3}/RT) * K_{298\,K\,(RWGS)} * C_{CO} C_{H_2O}$$
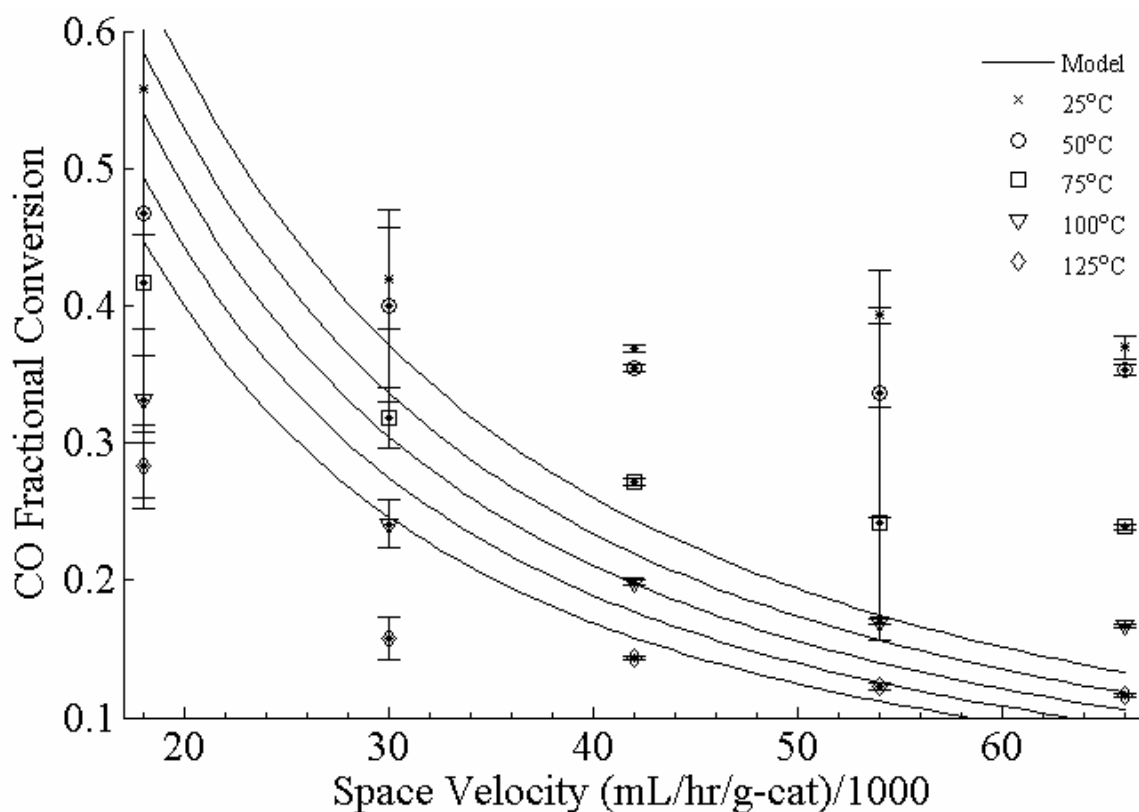
Figure 4.5 Comparison of model results for the linearly independent elementary model.

### 4.10.2 Linearly Independent Non-elementary Reaction Model Results

The last model in this series is the linearly independent non-elementary kinetic model. This model does represent the experimental data (Figure 4.6). The concentration dependence of the CO oxidation is not significantly different than what was calculated via the comprehensive non-linearly independent model found in Table 4.9. The calculated activation energy and pre-exponential are much higher in this model than in the previous incarnations. Once again the CO reaction order in CO oxidation is ~1.0 which is contrary to the expected value of ~0.[31] This last model proves that the PROX of CO in excess $H_2$ can be modeled within the temperature and space velocity constraints using a linearly independent set of reactions.

Table 4.13  Calculated pre-exponentials and activation energies for the linearly independent non-elementary model.

| | Pre-exponential | Activation Energy (kJ/mol) | $EXP_1$ | $EXP_2$ |
|---|---|---|---|---|
| $r_1 = -k_1 C_{CO}^{Exp_1} C_{O_2}^{Exp_2}$ | 10400 | 3.7 | 1.02 | 0.26 |
| $r_2 = -k_2 C_{CO_2}^{Exp_1} C_{H_2}^{Exp_2}$ | 71.9 | 6.9 | 0.34 | 0.45 |
| $r_3 = -k_2 * K_{298\,K\,(RWGS)} * C_{CO}^{Exp_1} C_{H_2O}^{Exp_2}$ | NA | NA | 0.32 | 2.89 |

Table 4.14  Empirical mole balances for the linearly independent non-elementary model.

$$\frac{dF_{CO}}{dW} = -10400 * \exp(-3.7/RT) * C_{CO}^{1\,02} C_{O_2}^{0\,26}$$
$$+71.9 * \exp(-6.9/RT) * C_{CO_2}^{0\,34} C_{H_2}^{0\,45}$$
$$-71.9 * \exp(-6.9/RT) * K_{298\,K\,(RWGS)} * C_{CO}^{0\,32} C_{H_2O}^{2\,89}$$

$$\frac{dF_{CO_2}}{dW} = +10400 * \exp(-3.7/RT) * C_{CO}^{1\,02} C_{O_2}^{0\,26}$$
$$-71.9 * \exp(-6.9/RT) * C_{CO_2}^{0\,34} C_{H_2}^{0\,45}$$
$$+71.9 * \exp(-6.9/RT) * K_{298\,K\,(RWGS)} * C_{CO}^{0\,32} C_{H_2O}^{2\,89}$$

$$\frac{dF_{H_2O}}{dW} = +71.9 * \exp(-6.9/RT) * C_{CO_2}^{0\,34} C_{H_2}^{0\,45}$$
$$-71.9 * \exp(-6.9/RT) * K_{298\,K\,(RWGS)} * C_{CO}^{0\,32} C_{H_2O}^{2\,89}$$

$$\frac{dF_{O_2}}{dW} = -\frac{1}{2} * 10400 * \exp(-3.7/RT) * C_{CO}^{1\,02} C_{O_2}^{0\,26}$$

$$\frac{dF_{H_2}}{dW} = -71.9 * \exp(-6.9/RT) * C_{CO_2}^{0\,34} C_{H_2}^{0\,45}$$
$$+71.9 * \exp(-6.9/RT) * K_{298\,K\,(RWGS)} * C_{CO}^{0\,32} C_{H_2O}^{2\,89}$$
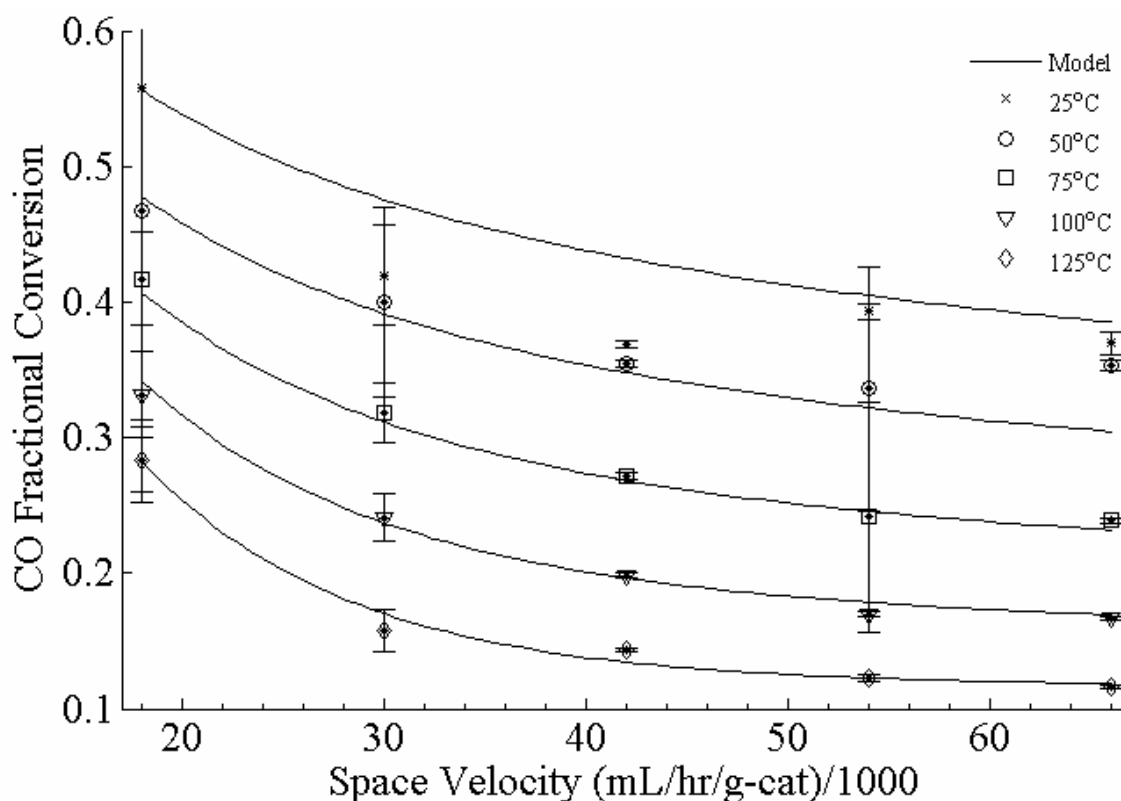
Figure 4.6  Comparison of model results for the linearly independent non-elementary model.

4.11  Verification of FTIR Effluent Concentrations via Gas Chromatography

Although the FTIR is highly sensitive to the concentrations of carbon monoxide, carbon dioxide, and water, there is an extreme limitation to the technique.  It is unable to measure diatomic molecules effluent concentrations (i.e. $H_2$, $O_2$, and $N_2$).  So, concurrently with each of the FTIR effluent runs, a 1 mL effluent gas sample was extracted and compared to the FTIR results.  The GC column used in all experiments was a Varian CP7534 plot fused silica 30 m x 0.32 mm ID coating Molsieve 5A (DF = 10 μm).  All GC experimental parameters are listed in Chapter 1.4.4.

A representative image of a GC effluent signal is shown in Figure 4.7.  Four peaks located at approximately 0.8, 1, 1.8, and 8 minutes correspond to the effluent concentrations of hydrogen, oxygen, nitrogen and carbon monoxide respectively.

Unfortunately, this column/detector combination was unable to detect either water or carbon dioxide for comparison.

Similar to the FTIR, area integrals of each curve are linearly proportional the concentration of the species and allow for the calculation of conversion. All peak signals should be positive except for hydrogen. The reason that the hydrogen signal is pointing in the opposite direction than the other peaks is because of the thermal conductivity detector's carrier gas being helium. The GC mV response is directly proportional to the molecular species entering the detector relative to a carrier gas reference. Oxygen, nitrogen, and carbon monoxide have a lower thermal conductivity than the carrier gas and the detector signal represents this as a positive peak. Oppositely, hydrogen has a higher thermal conductivity than helium and graphs as a negative peak.
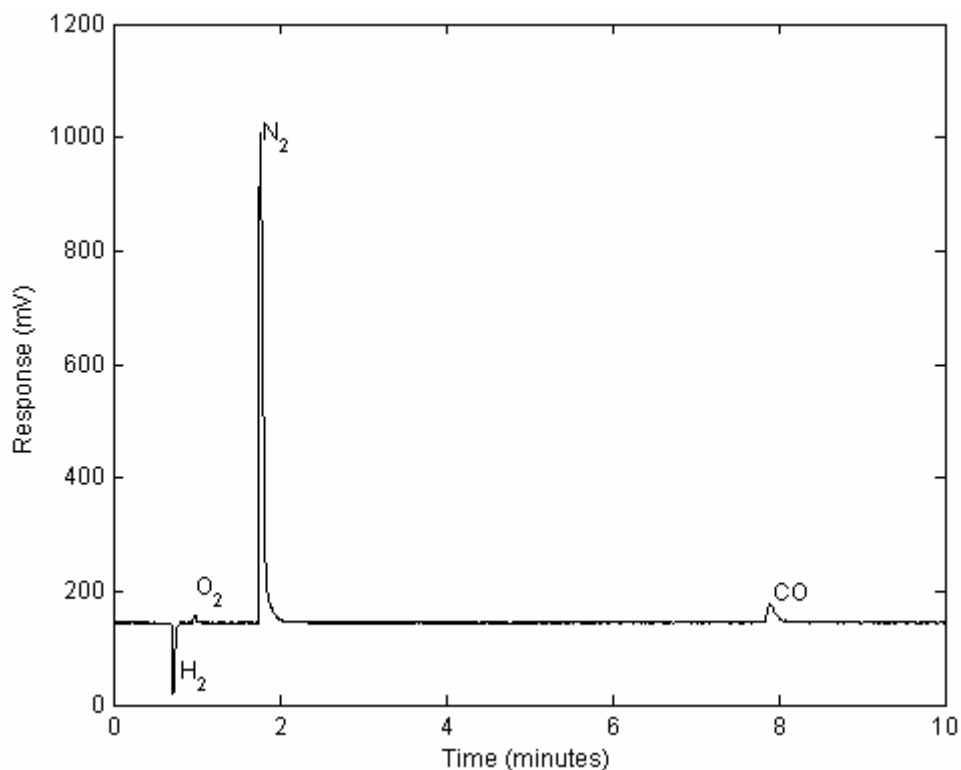


Figure 4.7 Representative image of a GC response spectrum of the effluent gases which include hydrogen, oxygen, nitrogen, carbon monoxide, carbon dioxide, and water.

I will begin the discussion of the GC results by examining the experimental integral data for hydrogen. Figure 4.8 shows the integral of the hydrogen signal becoming more negative as the flow rate of the 1%CO/H$_2$ mixture is increased. This is reasonable since an increasingly negative value of the integral indicates an increasing amount of H$_2$ in the effluent stream. Figure 4.9 graphs the integral of nitrogen in the effluent versus temperature and 1%CO/H$_2$ flow rate. The nitrogen in the feed stream to this process is treated as an inert, and therefore it does not react with any species at these operating temperatures. The decreasing integral is indicative of the fact that the 10 sccm air flow rate was kept constant. With increasing CO/H$_2$ flow rates, the fractional concentration of nitrogen decreased. Another observation is that as flow rate increases, the standard deviation between integrals at each temperature decreases. This discrepancy between samples is mirrored in other calculated integrals and is one rationale to install an autosampler to obtain more consistent results.
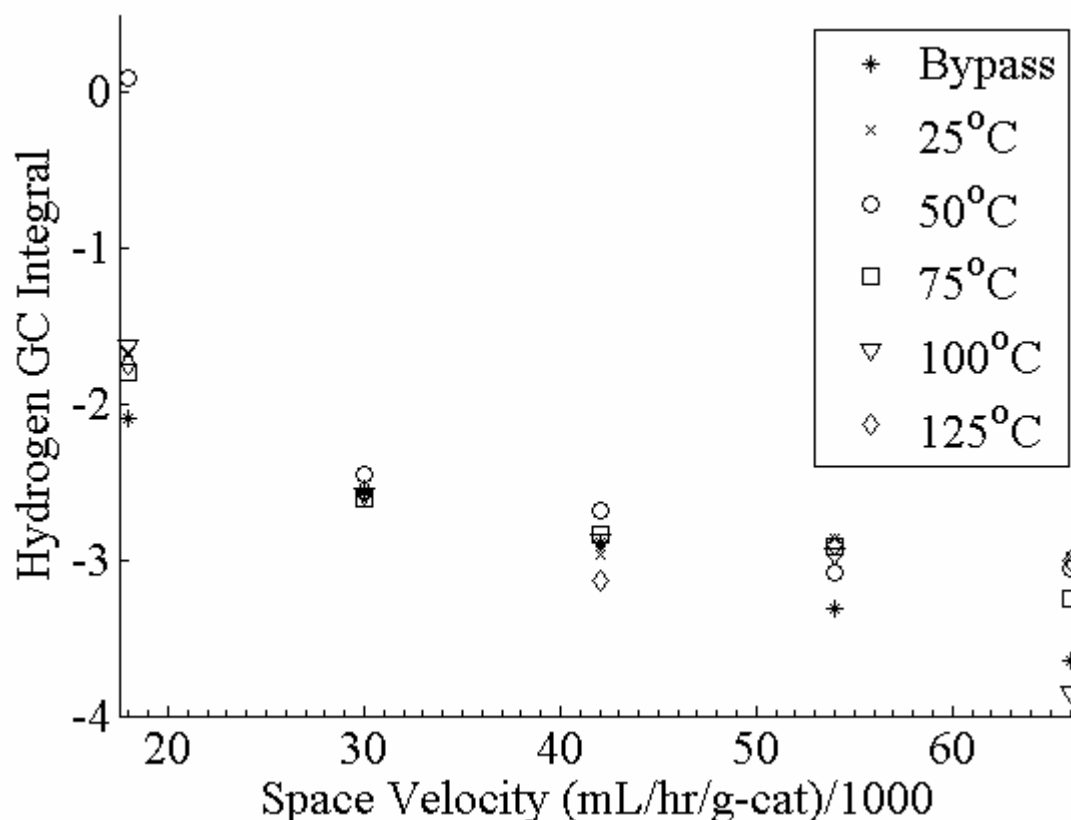


Figure 4.8 Integral of gas chromatography hydrogen spectrum data range versus influent flow rate at temperatures ranging from 25$^o$C-125$^o$C.

70
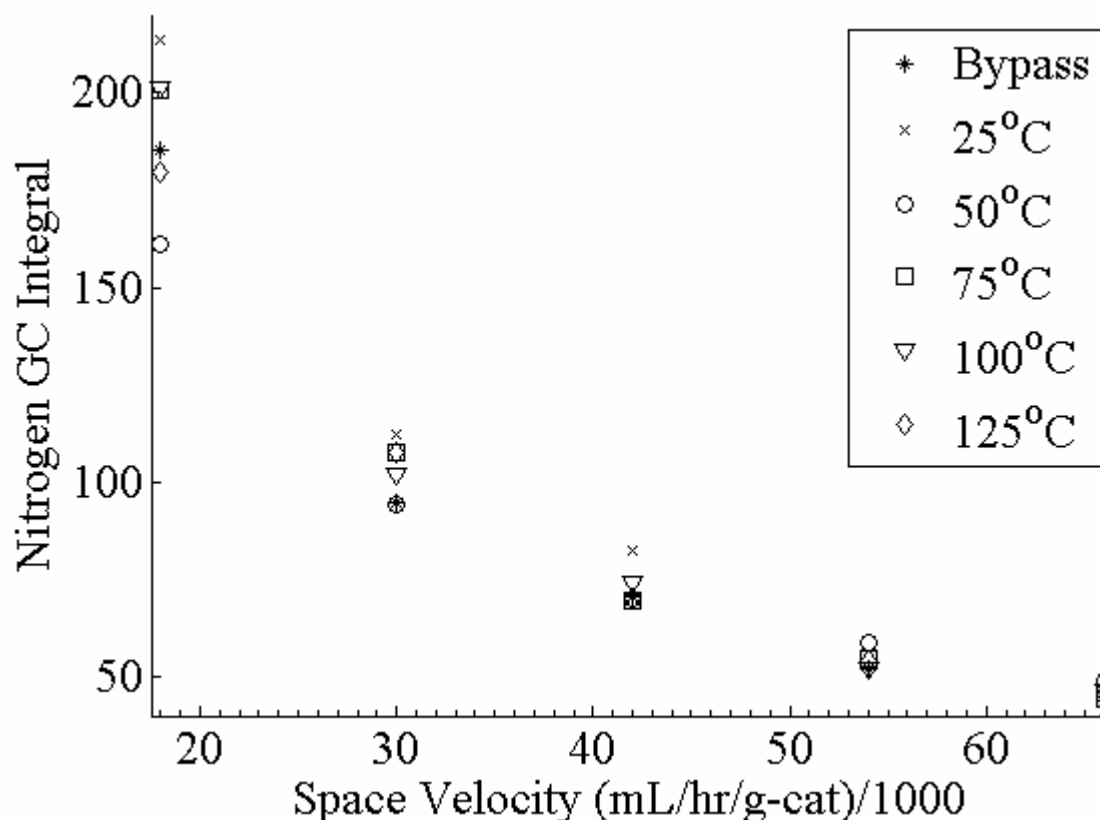
Figure 4.9  Integral of gas chromatography nitrogen spectrum data range versus influent flow rate at temperatures ranging from 25°C-125°C.

Figure 4.10 is one of the most interesting of the GC spectra.  As shown, the oxygen concentrations plummet to almost zero in each of the sample runs.  This indicates that the amount of oxygen in the influent is a limiting factor in the reaction kinetics and is completely depleted due to the carbon monoxide oxidation and hydrogen oxidation reactions.  Future work will include the effects of increasing the oxygen content.  Care must be taken to avoid the potential fire and explosion hazard of having a hydrogen/oxygen mixture entering an exothermic reaction.

Figure 4.11 represents the concentration of carbon monoxide in the effluent stream.  The general trend of the data follows that found by the FTIR (Figure 4.4) with the largest conversions of carbon monoxide occurring at the lowest temperature, 25°C (Figure 4.12).  Once again, the GC experimental integral results (Figure 4.11) are inconclusive at the lowest flow rate.  This is most likely due to the extremely low flow rate of the influent

71

gases. Even though the influents were allowed to equilibrate over ~1 hour, this may not have been enough time. Another possibility is that since these inaccuracies did not appear as significantly in the FTIR spectra, the flow regime does not allow for adequate mixing and, thus, syringe extraction is not extremely accurate at low flow rate regimes.

The conversion for 20 sccm was excluded due to experimental inaccuracies. The calculations for CO conversion are identical to the FTIR model with the conversion being defined as:

Conversion = (Bypass integral – Experimental Integral)/Bypass Integral          (4.20)

One would expect to have a nice correlation between the results of the FTIR and the GC; however, the GC conversion results (Figure 4.12) are much higher than the FTIR calculations although the trend is the same. However, with the sensitivity of the FTIR being much greater than the GC, the FTIR being plumbed directly, and the syringe transportation method to the GC introducing error into the procedure, the FTIR data is a more accurate representation of the effluent concentration.
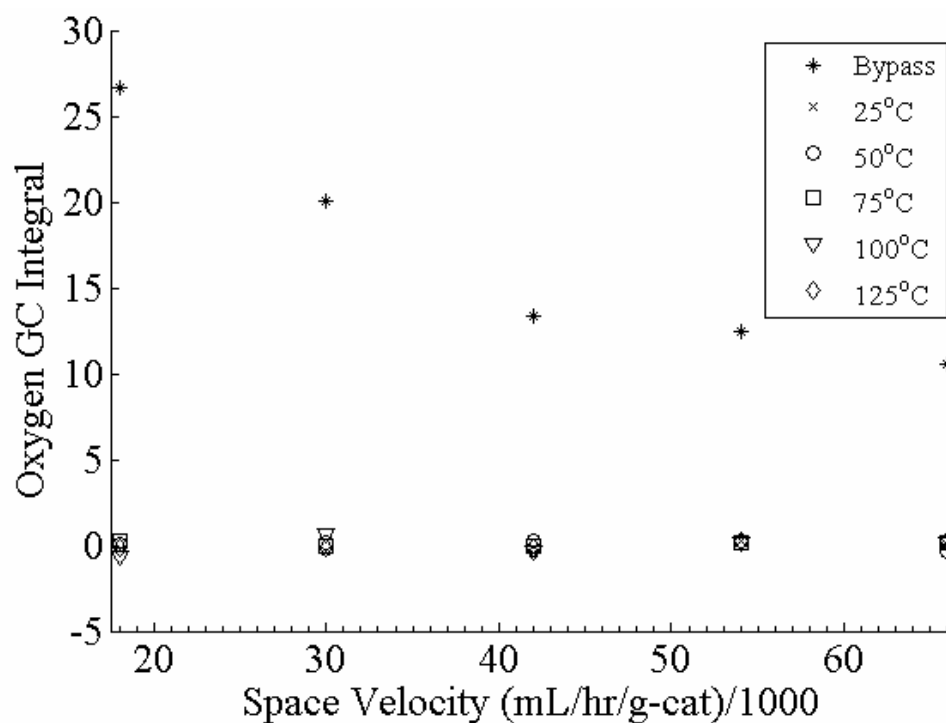
Figure 4.10  Integral of gas chromatography oxygen spectrum data range versus influent flow rate at temperatures ranging from $25^{o}$C-$125^{o}$C.
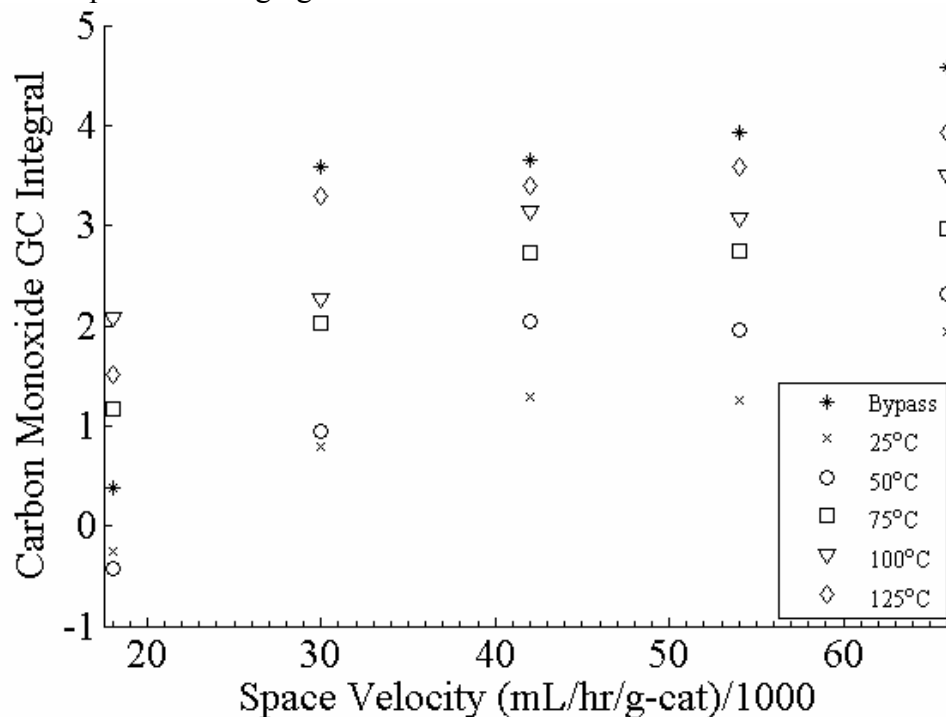


Figure 4.11  Integral of gas chromatography carbon monoxide spectrum data range versus influent flow rate at temperatures ranging from $25^{o}$C-$125^{o}$C.

## Experimental Conversion Results - GC
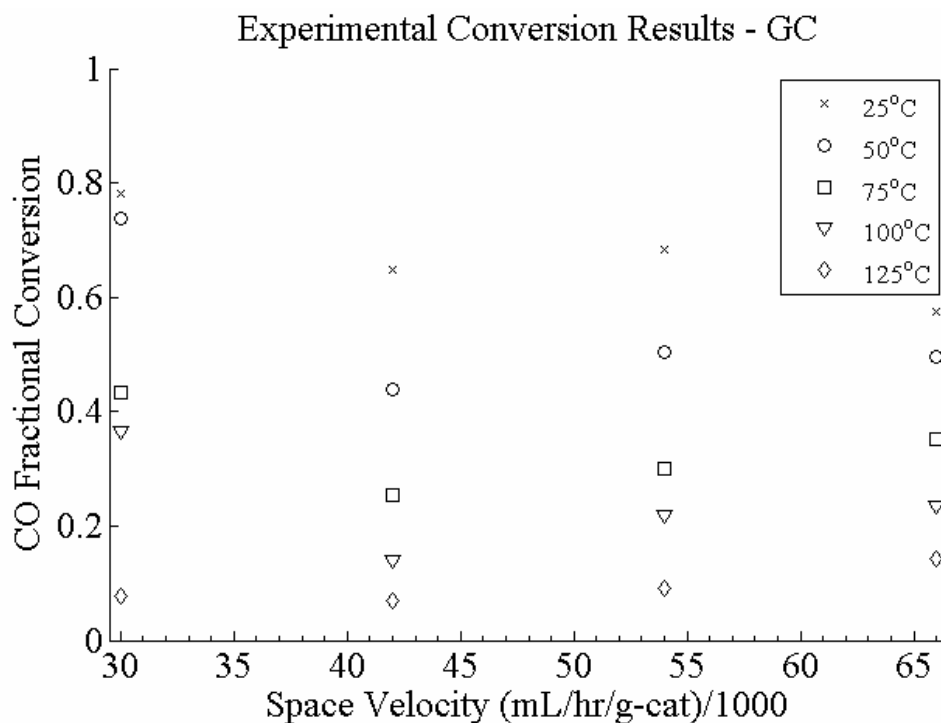


Figure 4.12 Conversion calculations of gas chromatography carbon monoxide spectrum data range versus influent flow rate at temperatures ranging from $25^oC$-$125^oC$.
Legend: $25^oC$(x), $50^oC$(o), $75^oC$($\square$), $100^oC$($\nabla$), $125^oC$($\diamond$)

4.12  Conclusions and Future Work

Several elementary and non-elementary models were presented which describe the effluent CO fractional conversions of a PROX reaction catalyzed by the World Gold Council nano-Au/TiO$_2$ catalyst.  Each model attempts to represent the effect of CO oxidation, hydrogen oxidation, and the water gas shift reaction on the reaction effluent concentrations of a 1% CO mixture in excess hydrogen with a small amount of air. These models included a single CO reaction elementary model, a set of comprehensive elementary/non-elementary, and linearly independent elementary/non-elementary kinetic models.

Beginning with the calculations of Gibbs free energy for each reaction at each temperature, it was verified that the CO oxidation, H$_2$ oxidation and WGS reactions are spontaneous at these conditions.  The reverse-water-gas-shift reaction is not favorable at the conditions examined.  The calculation of equilibrium constants verified the results.

74

After examining the results of the predicted models, none of the elementary models accurately depicted the CO oxidation experimental results. The conclusions gained from these tests find that the PROX of CO is unlikely to be an elementary reaction and should not be modeled as such. The non-linear models were better suited to calculating the effluent CO fractional conversions. Both the comprehensive and the linearly independent models accurately depicted the CO fractional conversion.

Since the non-elementary model accurately approximated the CO fractional conversion, correlation with previous studies are possible. Haruta discovered that the apparent activation energy of the carbon monoxide reaction approached zero as one approaches standard temperatures and pressures ($25^{\circ}C$, 1 atm). While the empirically derived value in this model is not zero, the activation energy of the CO oxidation reaction is significantly lower than the other reactions, resulting in less temperature dependence than all of the other reactions. Also, the oxygen reaction order for CO oxidation in the comprehensive kinetic model falls within the range sited in other papers for CO oxidation via $Au/TiO_2$.

After the analysis of the fits to the FTIR data, comparisons were made to the simultaneous GC measurements. The general trends of the GC matched the data collected from the FTIR with the highest CO conversion occurring at the lowest temperature. One interesting observation was the limiting amount of oxygen in the system. Another observation is that the GC conversion results are much higher than the FTIR calculations although the trend is the same. Inconsistencies are most likely due to the syringe transportation method introducing error into the procedure and will be addressed in future experiments.

Although, the experimental results show that the most effective CO oxidation for this catalyst system occurs much lower temperatures than PEMFCs operate which would suggest that incorporation of this catalyst into a PEMFC anode for CO reduction would

not be advantageous. A lower temperature pre-filter not incorporated into the fuel cell anode would be a better solution to remove CO contamination from the influent stream.

List of Variables for Chapter 4

$\alpha$ = pre-exponential factor
$A_{REF}$ = FTIR CO absorbance integral (2145-2230 cm$^{-1}$) of an unreacted feed stream
$A_{RXN}$ = FTIR CO absorbance integral (2145-2230 cm$^{-1}$) after reaction
$C_{CO}$ = concentration of carbon monoxide (mol/L)
$C_{CO2}$ = concentration of carbon dioxide (mol/L)
$C_{H2}$ = concentration of hydrogen (mol/L)
$C_{H2O}$ = concentration of water (mol/L)
$C_{N2}$ = concentration of nitrogen (mol/L)
$C_{O2}$ = concentration of oxygen (mol/L)
CO = carbon monoxide
$CO_2$ = carbon dioxide
$C_{Total}^{o}$ = total concentration
$C_{xx}$ = concentration of a single species
E = activation energy
Exp = exponent
$F_{CO}$ = flow rate of carbon monoxide (sccm)
$F_{CO2}$ = flow rate of carbon dioxide (sccm)
$F_{CO}^{o}$ = initial flow rate of carbon monoxide (sccm)
$F_{H2}$ = flow rate of hydrogen (sccm)
$F_{H2O}$ = flow rate of water (sccm)
$F_{N2}$ = flow rate of nitrogen (sccm)
$F_{O2}$ = flow rate of oxygen (sccm)
$F_{xx}$ = flow rate of a single species (sccm)
GNP = gold nanoparticle
$H_2$ = hydrogen
$H_2O$ = water
k = reaction rate constant
$N_2$ = nitrogen
PEMFC = proton exchange membrane fuel cell
PROX = preferential oxidation
r = reaction rate
W = weight of catalyst (gram)
WGC = World Gold Council
WGS = water-gas shift reaction which includes the reverse water gas shift reaction

# 5  FUTURE WORK

## 5.1  Introduction

In this study, two catalyst systems were evaluated: the two-phase-method GNPs provided by Dr. Gupta (Interfacial Phenomena and Polymeric Materials research group at USF) and the reference GNP/TiO$_2$ purchased from the World Gold Council.  Future work with the two-phase-method gold nanoparticles includes optimization of pre-treatment and fabrication to prevent nanoparticle agglomeration and to activate gold sites.  The goals in this future work are to reduce carbonization, improve CO transport to the catalyst surface, and to increase the surface-gold concentration.  Future work with the WGC Au/TiO$_2$ catalyst includes the determination of moisture effects on catalyst activity.  This will necessitate the introduction of more complex models and analysis.

## 5.2  Two-Phase-Method Gold

The proposed difficulties with the catalytic activity of the two-phase-method GNP catalysts are the surfactant layer used to prevent agglomeration of the particles and the inability of the gold particles to form a cohesive bond to the substrate.  While these two problems are related, I will begin with the hypothesized solutions to the surfactant layer. The initial solution to this problem was the evaporation of the solvent through the calcination step.  This has been proven to be unsuccessful.  The carbonization of the solvents used may be coating the gold particles and preventing transport to the surface. While this may not be the ultimate source of the inactivity of the catalyst, this is one aspect to consider.

Another possible cause is that the concentration of gold nanoparticles is too low even in a 4% mixture.  Although the initial loading for the 100 mg of TiO$_2$ is 4 mg which would lead to an ideal 4% mixture, there are inherent losses with the incipient wetness procedure.  Difficulties in quantifying the concentration after creation may have led to a

misrepresentation final catalyst's gold loading percentage. It has been speculated by both David Walker and Dr. Gupta that the gold nanoparticles may be attracted to the quartz containers and not sticking to the $TiO_2$ support. However, the redesign of the experiment to include in situ mixing of $TiO_2$ while the nanoparticles are being formed still did not lead to improved results. Increasing the initial concentration of gold to an 8% initial may not be the most elegant of solutions, but it may overcome the inherent losses of fabrication.

The next iteration of tests will include analysis of the pre-treatment procedure. Though this process has been developed for similar GNP pre-treatment in other research, this catalyst may require a more specialized process. The high mobility of the GNP on silicon shown in Section 3.2.4 may be responsible for the low activity due to reduction of low coordinated gold active sites.

The protocol for determining the activation of the $TiO_2$ support Brust GNPs will be as follows:

1. Calcination/Oxidation experiments
    a. Create 100 mg of 8% Au/$TiO_2$ catalyst
        i. Redesigned method to improve Au-$TiO_2$ adhesion (Section 4.5)
    b. Load 100 mg sample into FTIR micro-reactor
        i. No pretreatment
    c. Start at 100$^o$C in an oxygen environment
        i. Can vary time in oven from 30 minutes-2 hours
    d. FTIR effluent analysis to determine activity
        i. 20 sccm 1% CO/$H_2$
        ii. 10 sccm oxygen
    e. Repeat procedure for 150$^o$C-600$^o$C in 50$^o$C increments to determine if calcination is advantageous
        i. This should verify the necessity of a slight oxidation to end the pre-treatment procedure

2. Reduction Experiments

   a. Repeat 1.a-e but in a hydrogen rich environment to promote GNP and TiO₂ reduction.

## 5.3 Modification of the WGC Effluent Model

The most significant modification to the WGC model of the PROX reaction kinetics would be the inclusion of moisture effects on the reaction kinetics. For all models discussed in Chapter 5, dry gases were used for the experiments and no attempt was made to humidify the influent. Therefore, the influent gas moisture content was approximated to be 0%. This allowed the removal of that parameter from the equation.

This next set of experiments would necessitate several additions to the current setup, primarily a set of bubblers and relative humidity sensors. A diagram of the modified setup is shown in Figure 5.1 which shows a bubbler inline with the microreactor. A relative humidity gauge after the bubbler will indicate the moisture content of the influent stream. The models will remain exactly the same except for a slightly modified Arrhenius relationship for each of the species. Equation (3) in Chapter 5 will now become

$$k = \alpha * f(M,T) * \exp^{\left(-\frac{E}{RT}\right)}$$ (5.1)

where f(M,T) is a function of moisture content and temperature.
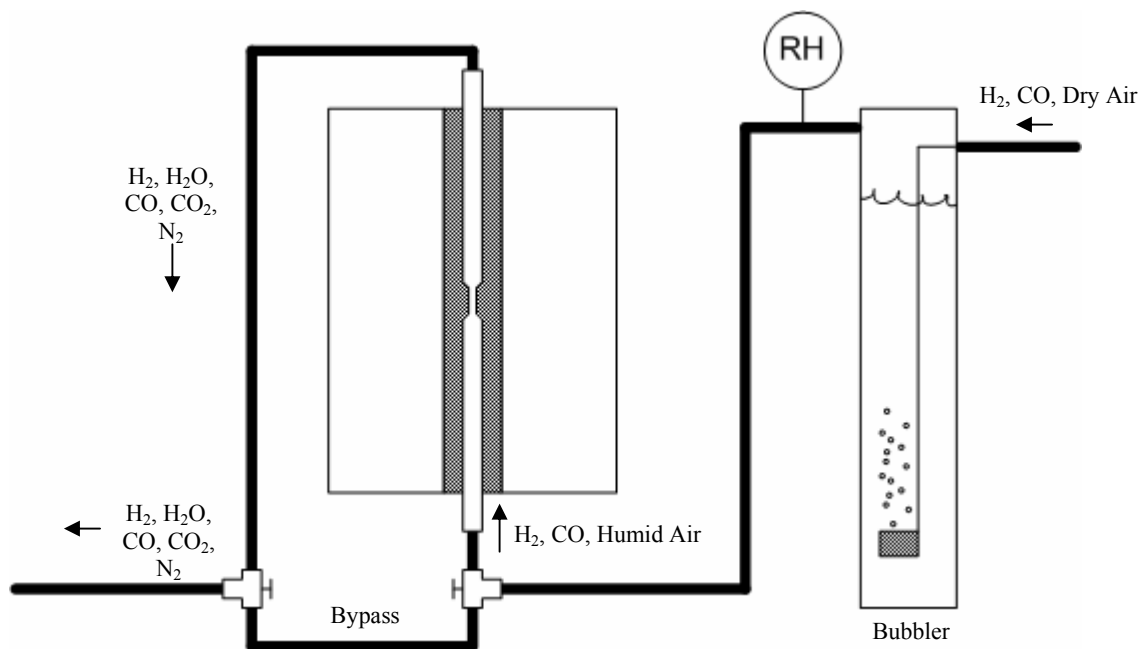
Figure 5.1  Modified microreactor setup which includes bubbler and relative humidity gauge for moisture content calculations.

## 5.4    Experimental Applications

Experimental results from the World Gold Council supported gold catalyst indicate that their use in fuel cell anodes may have limited results due to the predominance of the water gas shift reaction and hydrogen oxidation at normal operating conditions ($80^{\circ}$C, 1 atm).  The GNPs will mostly be useful for a room temperature pre-filter for the influent gases.  Having the temperature near room temperature or lower shifts the selectivity of the catalyst towards the production of $CO_2$ over $H_2O$.

REFERENCES

1    C.H. Bartholomew and R.J. Farrauto, *Fundamentals of Industrial Catalytic Processes*, Second ed. (John Wiley & Sons, Inc., 2006).

2    R.I. Masel, *Chemical Kinetics and Catlaysis* (John Wiley & Sons, Inc., 2001).

3    A. Cho, Science **299**(14 March 2003)**,** 1684-1685 (2003).

4    M.B. Cortie and E.v.d. Lingen, Materials Forum **26,** 1-14 (2002).

5    M. Haruta, Journal of New Materials for Electrochemical Systems **7,** 163-172 (2004).

6    P. Landon, J. Ferguson, B.E. Solsona, T. Garcia, A.F. Carley, A.A. Herzing, C.J. Kiely, S.E. Golunskic, and G.J. Hutchings, Chemical Communications**,** 3385-3387 (2005).

7    D. Cameron, R. Holliday, and D. Thompson, Journal of Power Sources **118,** 298-303 (2003).

8    Y. Choi and H.G. Stenger, Journal of Power Sources **129,** 246-254 (2004).

9    http://www1.eere.energy.gov/hydrogenandfuelcells/mypp/, "3.4 Fuel Cells", 2006.

10    R. O'Hayre, S.-W. Cha, W. Colella, and F.B. Prinz, *Fuel Cell Fundamentals* (John Wiley & Sons, Inc. , 2006).

11    S. Schimpf, M. Lucas, C. Mohra, U. Rodemerck, A. Bruckner, J. Radnik, H. Hofmeister, and P. Claus, Catalysis Today **2592,** 1-16 (2002).

12    G. Schmid and B. Corain, European Journal of Inorganic Chemistry**,** 3081-3098 (2003).

13    http://www.gold.org/discover/sci_indu/gold_catalysts/refcat.html.

14    *Metals Handbook*, Vol. 10, 9th ed. (1986).

15    N.A. Hodgea, C.J. Kiely, R. Whyman, M.R.H. Siddiqui, G.J. Hutchings, Q.A. Pankhurst, F.E. Wagner, R.R. Rajaram, and S.E. Golunski, Catalysis Today **72,** 133-144 (2002).

16    M. Okumura, S. Nakamura, S. Tsubota, T. Nakamura, M. Azuma, and M. Haruta, Catalysis Letters **51,** 53-58 (1998).

17    B.D. Cullity, *Elements of X-ray Diffraction, 2$^{nd}$ edition* (Addison-Wesley Publishing Company, Inc., 1978).

18    B.C. Smith, *Fundamentals of Fourier transform infrared spectroscopy* (CRC Press, Boca Raton, 1996).

19    Win-IR Pro online help, "Quant Analysis - error sources"(Version 3.4.2.025).

20    H. Phan, in *Fundamental Infrared Spectroscopy* (http://www.midac.com/apnotes/Tn-100.PDF).

21    B. Stuart, *Infrared Spectroscopy: Fundamentals and Applications* (John Wiley & Sons, Ltd, 2004).

22    T. Venkov, K. Fajerwerg, L. Delannoy, H. Klimev, K. Hadjiivanov, and C. Louis, Applied Catalysis A: General **301,** 106-114 (2006).

23    V. Rossiter, Research & Development(February 1988)**,** 94-97 (February 1988).

24    Agilent Technologies 6890N Gas Chromatograph User Information Manual **May** (2001).

25    http://www.impactanalytical.com/tga.html.

26    O. Levenspiel, *Chemical Reaction Engineering*, Third ed. (John Wiley & Sons, Inc., 1999).

27    M. Mavrikakis, P. Stoltze, and J.K. Nørskov, Catalysis Letters **64,** 101-106 (2000).

28    Z.-P. Liu, S.J. Jenkins, and D.A. King, Physical Review Letters **93**(No. 15)**,** 156102(4) (2004).

29    M. Haruta, The Chemical Record **3,** 75-87 (2003).

30    M.M. Schubert, S. Hackenberg, A.C.v. Veen, M. Muhler, V. Plzak, and R.J. Behm, Journal of Catalysis **197,** 113-122 (2001).

31    M. Haruta, Gold Bulletin **37**(1-2)**,** 27-36 (2004).

32     S.K. Shaikhutdinov, R. Meyer, M. Naschitzki, M. Baumer, and H.-J. Freund, Catalysis Letters **86**(No. 4, March)**,** 211-219 (2003).

33     D.T. Thompson, Topics in Catalysis **38**(4)**,** 231-240 (2006).

34     N.M. Gupta and A.K. Tripathi, Gold Bulletin **34**(4)**,** 120-128 (2001).

35     J. Guzman and B.C. Gates, Journal of the American Chemical Society **126,** 2672-2673 (2004).

36     M. Valden, X. Lai, and D.W. Goodman, Science **281,** 1647-1650 (11 September 1998).

37     T.V. Choudhary, C. Sivadinarayana, C.C. Chusuei, A.K. Datye, J. J.P.Fackler, and D.W.Goodman, Journal of Catalysis **207,** 247-255 (2002).

38     M. Brust, D. Bethell, D.J. Schiffrin, and C.J. Kiely, Advanced Materials **7,** 795 (1995).

39     C. Demaille, M. Brust, M. Tsionsky, and A.J. Bard, Analytical Chemistry **69,** 2323-2328 (1997).

40     http://www.eng.usf.edu/~vkgupta/.

41     I. Khramtsov, G.B. MacDonald, Z. Fakhraai, J.H. Teichroeb, and J.A. Forrest, (Department of Physics and Guelph-Waterloo Physics Institute, University of Waterloo, Canada, ON).

42     B.C. Beard, H.W. Sandusky, B.C. Glancy, and W.L. Elban, Surface and Interface Analysis **20**(2)**,** 140-148 (1993).

43     L. Maya, M. Paranthaman, T. Thundat, and M.L. Bauer, Journal of Vacuum Science and Technology B **14**(1)**,** 15-21 (1996).

44     M. Grutter, Atmosfera **16,** 1-13 (2003).

45     Z. Yang, R. Wu, Q. Zhang, and D.W. Goodman, Physical Review B **63,** 045419(6) (2001).

46     D.C. Sorescu and J.T. Yates, Jr., Journal of Physical Chemistry B **102,** 4556-4565 (1998).

47     Z. Dohnalek, J. Kim, O. Bondarchuk, J.M. White, and B.D. Kay, Journal of Physical Chemistry B **110,** 6229-6235 (2006).

48     K. Hadjiivanov, J. Lamotte, and J.-C. Lavalley, Langmuir **13,** 3374-3381 (1997).

49    T. Becker, C. Boas, U. Burghaus, and C. Woll, Physical Review B **61**(7)**,** 4538-4541 (2000).

50    D.E. De Vos and B.F. Sels, Angewandte Chemie International Edition **44,** 30-32 (2005).

51    S. Tsubota, A. Yamaguchi, M. Date, and M. Haruta**,** http://www.gold.org/discover/sci_indu/gold2003/pdf/s36a1383p1030.pdf.

52    M. Daté and M. Haruta, Journal of Catalysis **201,** 221-224 (2001).

53    N. Edwards, S.R. Ellis, J.C. Frost, S.E. Golunski, A.N.J. van Keulan, N.G. Lindewald, and J.G. Reinkingh, Journal of Power Sources **71,** 123-128 (1998).

54    J.M. Smith, H.C. Van Ness, and M.M. Abbott, *Introduction to Chemical Engineering Thermodynamics*, Sixth ed. (McGraw-Hill Companies, Inc., New York, NY, 2001).

55    http://www.gold.org/discover/sci_indu/gold2003/pdf/s36a1383p1030.pdf.

56    H.S. Fogler, *Elements of Chemical Reaction Engineering*, Fourth ed. (Prentice Hall Professional Technical Reference, 2006), p. 327.

57    M. Daté, M. Okumura, S. Tsubota, and M. Haruta, Angewandte Chemie International Edition **43,** 2129-2132 (2004).

APPENDICES

Appendix A  Matlab Code for FTIR Modeling


A.1 Elementary Model without WGS

function ElementaryModel_without_WGS

clc; close all; clear all

```
% Model of the reaction of the WGC and the Brust Gold
% CO + 1/2O2 = CO2            (Equation 1)
% A  + 1/2B  = C             (Equation 1.a)

% Temperature
T = [25*ones(1,5) 50*ones(1,5) 75*ones(1,5) 100*ones(1,5) 125*ones(1,5)];
R = 0.0821;                % Gas Constant (L*atm/mole*K)
P = 1;                     % Pressure
W = 0.1;                   % grams of catalyst

% Flow rates of the 1% mixture of CO in balance H2(sccm)
COH2 = [20 40 60 80 100 20 40 60 80 100 20 40 60 80 100 20 40 60 80 100 20 40 60 80
100];
% Amount of CO in the mixture(sccm)
CO = 0.01*COH2;

% Flow rates of Air(sccm)
Air = 10*ones(1,25);
% Amount of O2 in the Air(sccm)
O2 = 0.21*Air;

%Conversion
conversionCO = [0.5583 0.4195 0.3694 0.3932 0.3696 0.4674 0.3999 0.3545 0.3361
0.3533 0.4173 0.3181 0.2714 0.2414 0.2388 0.3318 0.2410 0.1982 0.1697 0.1667 0.2837
0.1576 0.1439 0.1229 0.1165];

yao = (CO./(COH2+Air));        % mole fraction of carbon monoxide
ybo = (O2./(COH2+Air));        % mole fraction of oxygen
Cao = yao*P./R.*T;             % Concentration A initially = moles/liter
Cbo = ybo*P./R.*T;             % Concentration B initially moles/liter
Fao = Cao.*CO*1/1000*1/60;     % Initial molar flowrate of A (moles/sec)
Fbo = Cbo.*O2*1/1000*1/60;     % Initial molar flowrate of B (moles/sec)

% theta_b = Fbo/Fao
theta_b = Fbo./Fao;
```

Appendix A (Continued)

```
% epsilon = (c/a - b/a - a/a)*Va/Vt
epsilon = (1/1 - (1/2)/1 -1/1)*(CO./(COH2+Air));
% ratio b to a; coefficients of CO and O2 in Equation 1.a
ratio_ba = (1/2)/1;
%
% PBR Design Equation
%

% Fao*dX/dW = -ra
% -ra = k*Ca*Cb^1/2
% Ca = Cao(1-X)/(1 + epsilon*X)
% Cb = Cbo(theta_b - ratio_ba*X)/(1 + epsilon*X)

% -ra = k*Ca*Cb^1/2
% k = alpha*exp(-E/RT)

% Fao*dX/dW = alpha*exp(-E/RT))*Ca*Cb^1/2
% (Fao/alpha*exp(-E/RT))*Ca*Cb^1/2)dX = dW

% (Fao/alpha*exp(-E/RT))*Integral of (Ca*Cb^1/2) = W
% (Fao/W)*Integral = alpha*exp(-E/RT)

% ln((Fao/W)*Integral = ln alpha - E/R*1/T

% Therefore a plot of

% ln((Fao/(W*Integral of (Ca*Cb^1/2))) vs (1/T) should give me activation
% energy.  From there I can get the preexponential factor. Then, calculate
% k and have a model of the activity of the oxidation reaction.

% Experimentally determine conversion

for n = 1:length(T)
    whos
    X = linspace(0, conversionCO(n));
    Ca(n,:) = Cao(n).*(1-X)./(1+epsilon(n).*X);
    Cb(n,:) = Cao(n).*(theta_b(n) - ratio_ba*X)./(1+epsilon(n).*X);
    Y = 1./(Ca(n,:).*(Cb(n,:).^(1/2)));
    Integral(n) = Simpson(X,Y)
    Answer(n) = log((Fao(n)/W)*Integral(n));
end

 hold on
```

Appendix A (Continued)

```
plot(1./T(1:5), Answer(1:5), 'ko')
plot(1./T(6:10), Answer(6:10), 'ko')
plot(1./T(11:15), Answer(11:15), 'ko')
plot(1./T(16:20), Answer(16:20), 'ko')
plot(1./T(21:25), Answer(21:25), 'ko')

%
% poly = polyfit(1./T, Answer, 1)
% hold on
% plot(linspace(1./T(1), 1./T(end)), poly(1).*linspace(1./T(1), 1./T(end))+ poly(2), 'k:')
xlabel('1/Temperature (K^{-1})')
ylabel('ln((Fao/W)*Integral of (Ca*Cb^1/2)))')
```

A.2  Comprehensive Elementary Model Fit Routine

```
function Final = Nonlinear_leastsquares_fit_WGC_version3_Ele(Initialguesses)
% Edit
% I removed some of the errant points to get a better fit
close all; clc

% conversionCO = [0.5583 0.4195 0.3694 0.3932 0.3696 0.4674 0.3999 0.3545 0.3361
0.3533 0.4173 0.3181 0.2714 0.2414 0.2388 0.3318 0.2410 0.1982 0.1697 0.1667 0.2837
0.1576 0.1439 0.1229 0.1165];
conversionCO = [0.5583 0.3932 0.3696 0.4674 0.3999 0.3545 0.3361 0.4173 0.3181
0.2714 0.2414 0.2388 0.3318 0.2410 0.1982 0.1697 0.1667 0.1576 0.1439 0.1229
0.1165];
Temps  = [25 50 75 100 125];
Air    = [10 10 10 10 10];
COH2   = [20 40 60 80 100];

data = [Temps; Air; COH2];

[Final,RESNORM,RESIDUAL,EXITFLAG,OUTPUT,LAMBDA,JACOBIAN] =
lsqcurvefit(@myfun, Initialguesses, data, conversionCO, [0 0 0 0 0 0 0 0], [+inf +inf +inf
+inf 50000 50000 50000 50000])

function Conversionresults = myfun(VAR, data);

Temps = data(1,:);
Air   = data(2,:);
COH2  = data(3,:);
```

Appendix A (Continued)

```
%  Conversionresults = NewmodelwithWGS_version2(Temperature, alpha, E, [CO O2
CO2 H2 H2O N2])
Conversionresults(1) = NewmodelwithWGS_version2(Temps(1), [VAR(1) VAR(2)
VAR(3) VAR(4)], [VAR(5) VAR(6) VAR(7) VAR(8)], [0.01*COH2(1)  0.21*10 0
0.99*COH2(1)  0 0.79*Air(1)], [1 0.5 1 0.5 1 1 1 1]);     % 10 sccm Air 20 sccm COH2
% Conversionresults(2) = NewmodelwithWGS_version2(Temps(1), [VAR(1) VAR(2)
VAR(3) VAR(4)], [VAR(5) VAR(6) VAR(7) VAR(8)], [0.01*COH2(2)  0.21*Air(2) 0
0.99*COH2(2)  0 0.79*Air(2)]);     % 10 sccm Air 40 sccm COH2
% Conversionresults(3) = NewmodelwithWGS_version2(Temps(1), [VAR(1) VAR(2)
VAR(3) VAR(4)], [VAR(5) VAR(6) VAR(7) VAR(8)], [0.01*COH2(3)  0.21*Air(3) 0
0.99*COH2(3)  0 0.79*Air(3)]);     % 10 sccm Air 60 sccm COH2
Conversionresults(2) = NewmodelwithWGS_version2(Temps(1), [VAR(1) VAR(2)
VAR(3) VAR(4)], [VAR(5) VAR(6) VAR(7) VAR(8)], [0.01*COH2(4)  0.21*10 0
0.99*COH2(4)  0 0.79*Air(4)], [1 0.5 1 0.5 1 1 1 1]);     % 10 sccm Air 80 sccm COH2
Conversionresults(3) = NewmodelwithWGS_version2(Temps(1), [VAR(1) VAR(2)
VAR(3) VAR(4)], [VAR(5) VAR(6) VAR(7) VAR(8)], [0.01*COH2(5)  0.21*10 0
0.99*COH2(5)  0 0.79*Air(5)], [1 0.5 1 0.5 1 1 1 1]);     % 10 sccm Air 100 sccm COH2

Conversionresults(4) = NewmodelwithWGS_version2(Temps(2), [VAR(1) VAR(2)
VAR(3) VAR(4)], [VAR(5) VAR(6) VAR(7) VAR(8)], [0.01*COH2(1)  0.21*10 0
0.99*COH2(1)  0 0.79*10], [1 0.5 1 0.5 1 1 1 1]);     % 10 sccm Air 20 sccm COH2
Conversionresults(5) = NewmodelwithWGS_version2(Temps(2), [VAR(1) VAR(2)
VAR(3) VAR(4)], [VAR(5) VAR(6) VAR(7) VAR(8)], [0.01*COH2(2)  0.21*10 0
0.99*COH2(2)  0 0.79*10], [1 0.5 1 0.5 1 1 1 1]);     % 10 sccm Air 40 sccm COH2
Conversionresults(6) = NewmodelwithWGS_version2(Temps(2), [VAR(1) VAR(2)
VAR(3) VAR(4)], [VAR(5) VAR(6) VAR(7) VAR(8)], [0.01*COH2(3)  0.21*10 0
0.99*COH2(3)  0 0.79*10], [1 0.5 1 0.5 1 1 1 1]);     % 10 sccm Air 60 sccm COH2
Conversionresults(7) = NewmodelwithWGS_version2(Temps(2), [VAR(1) VAR(2)
VAR(3) VAR(4)], [VAR(5) VAR(6) VAR(7) VAR(8)], [0.01*COH2(4)  0.21*10 0
0.99*COH2(4)  0 0.79*10], [1 0.5 1 0.5 1 1 1 1]);     % 10 sccm Air 80 sccm COH2
% Conversionresults(10) = NewmodelwithWGS_version2(Temps(2), [VAR(1) VAR(2)
VAR(3) VAR(4)], [VAR(5) VAR(6) VAR(7) VAR(8)], [0.01*COH2(5) 0.21*10 0
0.99*COH2(5)  0 0.79*10]);     % 10 sccm Air 100 sccm COH2

Conversionresults(8) = NewmodelwithWGS_version2(Temps(3), [VAR(1) VAR(2)
VAR(3) VAR(4)], [VAR(5) VAR(6) VAR(7) VAR(8)], [0.01*COH2(1)  0.21*10 0
0.99*COH2(1)  0 0.79*10], [1 0.5 1 0.5 1 1 1 1]);     % 10 sccm Air 20 sccm COH2
Conversionresults(9) = NewmodelwithWGS_version2(Temps(3), [VAR(1) VAR(2)
VAR(3) VAR(4)], [VAR(5) VAR(6) VAR(7) VAR(8)], [0.01*COH2(2)  0.21*10 0
0.99*COH2(2)  0 0.79*10], [1 0.5 1 0.5 1 1 1 1]);     % 10 sccm Air 40 sccm COH2
Conversionresults(10) = NewmodelwithWGS_version2(Temps(3), [VAR(1) VAR(2)
VAR(3) VAR(4)], [VAR(5) VAR(6) VAR(7) VAR(8)], [0.01*COH2(3)  0.21*10 0
0.99*COH2(3)  0 0.79*10], [1 0.5 1 0.5 1 1 1 1]);     % 10 sccm Air 60 sccm COH2
```

Appendix A (Continued)

Conversionresults(11) = NewmodelwithWGS_version2(Temps(3), [VAR(1) VAR(2)
VAR(3) VAR(4)], [VAR(5) VAR(6) VAR(7) VAR(8)], [0.01*COH2(4)  0.21*10 0
0.99*COH2(4)  0 0.79*10], [1 0.5 1 0.5 1 1 1 1]);     % 10 sccm Air 80 sccm COH2
Conversionresults(12) = NewmodelwithWGS_version2(Temps(3), [VAR(1) VAR(2)
VAR(3) VAR(4)], [VAR(5) VAR(6) VAR(7) VAR(8)], [0.01*COH2(5)  0.21*10 0
0.99*COH2(5)  0 0.79*10], [1 0.5 1 0.5 1 1 1 1]);     % 10 sccm Air 100 sccm COH2

Conversionresults(13) = NewmodelwithWGS_version2(Temps(4), [VAR(1) VAR(2)
VAR(3) VAR(4)], [VAR(5) VAR(6) VAR(7) VAR(8)], [0.01*COH2(1)  0.21*10 0
0.99*COH2(1)  0 0.79*10], [1 0.5 1 0.5 1 1 1 1]);     % 10 sccm Air 20 sccm COH2
Conversionresults(14) = NewmodelwithWGS_version2(Temps(4), [VAR(1) VAR(2)
VAR(3) VAR(4)], [VAR(5) VAR(6) VAR(7) VAR(8)], [0.01*COH2(2)  0.21*10 0
0.99*COH2(2)  0 0.79*10], [1 0.5 1 0.5 1 1 1 1]);     % 10 sccm Air 40 sccm COH2
Conversionresults(15) = NewmodelwithWGS_version2(Temps(4), [VAR(1) VAR(2)
VAR(3) VAR(4)], [VAR(5) VAR(6) VAR(7) VAR(8)], [0.01*COH2(3)  0.21*10 0
0.99*COH2(3)  0 0.79*10], [1 0.5 1 0.5 1 1 1 1]);     % 10 sccm Air 60 sccm COH2
Conversionresults(16) = NewmodelwithWGS_version2(Temps(4), [VAR(1) VAR(2)
VAR(3) VAR(4)], [VAR(5) VAR(6) VAR(7) VAR(8)], [0.01*COH2(4)  0.21*10 0
0.99*COH2(4)  0 0.79*10], [1 0.5 1 0.5 1 1 1 1]);     % 10 sccm Air 80 sccm COH2
Conversionresults(17) = NewmodelwithWGS_version2(Temps(4), [VAR(1) VAR(2)
VAR(3) VAR(4)], [VAR(5) VAR(6) VAR(7) VAR(8)], [0.01*COH2(5)  0.21*10 0
0.99*COH2(5)  0 0.79*10], [1 0.5 1 0.5 1 1 1 1]);     % 10 sccm Air 100 sccm COH2

% Conversionresults(21) = NewmodelwithWGS_version2(Temps(5), [VAR(1) VAR(2)
VAR(3) VAR(4)], [VAR(5) VAR(6) VAR(7) VAR(8)], [0.01*COH2(1)  0.21*10 0
0.99*COH2(1)  0 0.79*10]);     % 10 sccm Air 20 sccm COH2
Conversionresults(18) = NewmodelwithWGS_version2(Temps(5), [VAR(1) VAR(2)
VAR(3) VAR(4)], [VAR(5) VAR(6) VAR(7) VAR(8)], [0.01*COH2(2)  0.21*10 0
0.99*COH2(2)  0 0.79*10], [1 0.5 1 0.5 1 1 1 1]);     % 10 sccm Air 40 sccm COH2
Conversionresults(19) = NewmodelwithWGS_version2(Temps(5), [VAR(1) VAR(2)
VAR(3) VAR(4)], [VAR(5) VAR(6) VAR(7) VAR(8)], [0.01*COH2(3)  0.21*10 0
0.99*COH2(3)  0 0.79*10], [1 0.5 1 0.5 1 1 1 1]);     % 10 sccm Air 60 sccm COH2
Conversionresults(20) = NewmodelwithWGS_version2(Temps(5), [VAR(1) VAR(2)
VAR(3) VAR(4)], [VAR(5) VAR(6) VAR(7) VAR(8)], [0.01*COH2(4)  0.21*10 0
0.99*COH2(4)  0 0.79*10], [1 0.5 1 0.5 1 1 1 1]);     % 10 sccm Air 80 sccm COH2
Conversionresults(21) = NewmodelwithWGS_version2(Temps(5), [VAR(1) VAR(2)
VAR(3) VAR(4)], [VAR(5) VAR(6) VAR(7) VAR(8)], [0.01*COH2(5)  0.21*10 0
0.99*COH2(5)  0 0.79*10], [1 0.5 1 0.5 1 1 1 1]);     % 10 sccm Air 100 sccm COH2


A.3  Comprehensive Non-Elementary Model Fit Routine

function Final = Nonlinear_leastsquares_fit_WGC_version3_Non(Initialguesses)

90

Appendix A (Continued)

```
% Edit
% I removed some of the errant points to get a better fit
close all; clc

% conversionCO = [0.5583 0.4195 0.3694 0.3932 0.3696 0.4674 0.3999 0.3545 0.3361
0.3533 0.4173 0.3181 0.2714 0.2414 0.2388 0.3318 0.2410 0.1982 0.1697 0.1667 0.2837
0.1576 0.1439 0.1229 0.1165];
conversionCO = [0.5583 0.3932 0.3696 0.4674 0.3999 0.3545 0.3361 0.4173 0.3181
0.2714 0.2414 0.2388 0.3318 0.2410 0.1982 0.1697 0.1667 0.1576 0.1439 0.1229
0.1165];
Temps  = [25 50 75 100 125];
Air    = [10 10 10 10 10];
COH2   = [20 40 60 80 100];

data = [Temps; Air; COH2];

[Final,RESNORM,RESIDUAL,EXITFLAG,OUTPUT,LAMBDA,JACOBIAN] =
lsqcurvefit(@myfun, Initialguesses, data, conversionCO, [0 0 0 0 0 0 0 0 -2 -2 -2 -2 -2 -2
-2 -2], [+inf +inf +inf +inf 50000 50000 50000 50000 2 2 2 2 2 2 2 2])

function Conversionresults = myfun(VAR, data);

Temps = data(1,:);
Air   = data(2,:);
COH2  = data(3,:);

%  Conversionresults = NewmodelwithWGS_version2(Temperature, alpha, E, [CO O2
CO2 H2 H2O N2])
Conversionresults(1) = NewmodelwithWGS_version2(Temps(1), [VAR(1) VAR(2)
VAR(3) VAR(4)], [VAR(5) VAR(6) VAR(7) VAR(8)], [0.01*COH2(1)  0.21*10 0
0.99*COH2(1)  0 0.79*Air(1)], [VAR(9) VAR(10) VAR(11) VAR(12) VAR(13)
VAR(14) VAR(15) VAR(16)]);     % 10 sccm Air 20 sccm COH2
% Conversionresults(2) = NewmodelwithWGS_version2(Temps(1), [VAR(1) VAR(2)
VAR(3) VAR(4)], [VAR(5) VAR(6) VAR(7) VAR(8)], [0.01*COH2(2)  0.21*Air(2) 0
0.99*COH2(2)  0 0.79*Air(2)]);     % 10 sccm Air 40 sccm COH2
% Conversionresults(3) = NewmodelwithWGS_version2(Temps(1), [VAR(1) VAR(2)
VAR(3) VAR(4)], [VAR(5) VAR(6) VAR(7) VAR(8)], [0.01*COH2(3)  0.21*Air(3) 0
0.99*COH2(3)  0 0.79*Air(3)]);     % 10 sccm Air 60 sccm COH2
Conversionresults(2) = NewmodelwithWGS_version2(Temps(1), [VAR(1) VAR(2)
VAR(3) VAR(4)], [VAR(5) VAR(6) VAR(7) VAR(8)], [0.01*COH2(4)  0.21*10 0
0.99*COH2(4)  0 0.79*Air(4)], [VAR(9) VAR(10) VAR(11) VAR(12) VAR(13)
VAR(14) VAR(15) VAR(16)]);     % 10 sccm Air 80 sccm COH2
```

Appendix A (Continued)

Conversionresults(3) = NewmodelwithWGS_version2(Temps(1), [VAR(1) VAR(2)
VAR(3) VAR(4)], [VAR(5) VAR(6) VAR(7) VAR(8)], [0.01*COH2(5)  0.21*10 0
0.99*COH2(5)  0 0.79*Air(5)], [VAR(9) VAR(10) VAR(11) VAR(12) VAR(13)
VAR(14) VAR(15) VAR(16)]);     % 10 sccm Air 100 sccm COH2


Conversionresults(4) = NewmodelwithWGS_version2(Temps(2), [VAR(1) VAR(2)
VAR(3) VAR(4)], [VAR(5) VAR(6) VAR(7) VAR(8)], [0.01*COH2(1)  0.21*10 0
0.99*COH2(1)  0 0.79*10], [VAR(9) VAR(10) VAR(11) VAR(12) VAR(13) VAR(14)
VAR(15) VAR(16)]);     % 10 sccm Air 20 sccm COH2
Conversionresults(5) = NewmodelwithWGS_version2(Temps(2), [VAR(1) VAR(2)
VAR(3) VAR(4)], [VAR(5) VAR(6) VAR(7) VAR(8)], [0.01*COH2(2)  0.21*10 0
0.99*COH2(2)  0 0.79*10], [VAR(9) VAR(10) VAR(11) VAR(12) VAR(13) VAR(14)
VAR(15) VAR(16)]);     % 10 sccm Air 40 sccm COH2
Conversionresults(6) = NewmodelwithWGS_version2(Temps(2), [VAR(1) VAR(2)
VAR(3) VAR(4)], [VAR(5) VAR(6) VAR(7) VAR(8)], [0.01*COH2(3)  0.21*10 0
0.99*COH2(3)  0 0.79*10], [VAR(9) VAR(10) VAR(11) VAR(12) VAR(13) VAR(14)
VAR(15) VAR(16)]);     % 10 sccm Air 60 sccm COH2
Conversionresults(7) = NewmodelwithWGS_version2(Temps(2), [VAR(1) VAR(2)
VAR(3) VAR(4)], [VAR(5) VAR(6) VAR(7) VAR(8)], [0.01*COH2(4)  0.21*10 0
0.99*COH2(4)  0 0.79*10], [VAR(9) VAR(10) VAR(11) VAR(12) VAR(13) VAR(14)
VAR(15) VAR(16)]);     % 10 sccm Air 80 sccm COH2
% Conversionresults(10) = NewmodelwithWGS_version2(Temps(2), [VAR(1) VAR(2)
VAR(3) VAR(4)], [VAR(5) VAR(6) VAR(7) VAR(8)], [0.01*COH2(5) 0.21*10 0
0.99*COH2(5)  0 0.79*10]);     % 10 sccm Air 100 sccm COH2


Conversionresults(8) = NewmodelwithWGS_version2(Temps(3), [VAR(1) VAR(2)
VAR(3) VAR(4)], [VAR(5) VAR(6) VAR(7) VAR(8)], [0.01*COH2(1)  0.21*10 0
0.99*COH2(1)  0 0.79*10], [VAR(9) VAR(10) VAR(11) VAR(12) VAR(13) VAR(14)
VAR(15) VAR(16)]);     % 10 sccm Air 20 sccm COH2
Conversionresults(9) = NewmodelwithWGS_version2(Temps(3), [VAR(1) VAR(2)
VAR(3) VAR(4)], [VAR(5) VAR(6) VAR(7) VAR(8)], [0.01*COH2(2)  0.21*10 0
0.99*COH2(2)  0 0.79*10], [VAR(9) VAR(10) VAR(11) VAR(12) VAR(13) VAR(14)
VAR(15) VAR(16)]);     % 10 sccm Air 40 sccm COH2
Conversionresults(10) = NewmodelwithWGS_version2(Temps(3), [VAR(1) VAR(2)
VAR(3) VAR(4)], [VAR(5) VAR(6) VAR(7) VAR(8)], [0.01*COH2(3)  0.21*10 0
0.99*COH2(3)  0 0.79*10], [VAR(9) VAR(10) VAR(11) VAR(12) VAR(13) VAR(14)
VAR(15) VAR(16)]);     % 10 sccm Air 60 sccm COH2
Conversionresults(11) = NewmodelwithWGS_version2(Temps(3), [VAR(1) VAR(2)
VAR(3) VAR(4)], [VAR(5) VAR(6) VAR(7) VAR(8)], [0.01*COH2(4)  0.21*10 0
0.99*COH2(4)  0 0.79*10], [VAR(9) VAR(10) VAR(11) VAR(12) VAR(13) VAR(14)
VAR(15) VAR(16)]);     % 10 sccm Air 80 sccm COH2
Conversionresults(12) = NewmodelwithWGS_version2(Temps(3), [VAR(1) VAR(2)
VAR(3) VAR(4)], [VAR(5) VAR(6) VAR(7) VAR(8)], [0.01*COH2(5)  0.21*10 0

Appendix A (Continued)

0.99*COH2(5)  0 0.79*10], [VAR(9) VAR(10) VAR(11) VAR(12) VAR(13) VAR(14)
VAR(15) VAR(16)]);      % 10 sccm Air 100 sccm COH2

Conversionresults(13) = NewmodelwithWGS_version2(Temps(4), [VAR(1) VAR(2)
VAR(3) VAR(4)], [VAR(5) VAR(6) VAR(7) VAR(8)], [0.01*COH2(1)  0.21*10 0
0.99*COH2(1)  0 0.79*10], [VAR(9) VAR(10) VAR(11) VAR(12) VAR(13) VAR(14)
VAR(15) VAR(16)]);      % 10 sccm Air 20 sccm COH2
Conversionresults(14) = NewmodelwithWGS_version2(Temps(4), [VAR(1) VAR(2)
VAR(3) VAR(4)], [VAR(5) VAR(6) VAR(7) VAR(8)], [0.01*COH2(2)  0.21*10 0
0.99*COH2(2)  0 0.79*10], [VAR(9) VAR(10) VAR(11) VAR(12) VAR(13) VAR(14)
VAR(15) VAR(16)]);      % 10 sccm Air 40 sccm COH2
Conversionresults(15) = NewmodelwithWGS_version2(Temps(4), [VAR(1) VAR(2)
VAR(3) VAR(4)], [VAR(5) VAR(6) VAR(7) VAR(8)], [0.01*COH2(3)  0.21*10 0
0.99*COH2(3)  0 0.79*10], [VAR(9) VAR(10) VAR(11) VAR(12) VAR(13) VAR(14)
VAR(15) VAR(16)]);      % 10 sccm Air 60 sccm COH2
Conversionresults(16) = NewmodelwithWGS_version2(Temps(4), [VAR(1) VAR(2)
VAR(3) VAR(4)], [VAR(5) VAR(6) VAR(7) VAR(8)], [0.01*COH2(4)  0.21*10 0
0.99*COH2(4)  0 0.79*10], [VAR(9) VAR(10) VAR(11) VAR(12) VAR(13) VAR(14)
VAR(15) VAR(16)]);      % 10 sccm Air 80 sccm COH2
Conversionresults(17) = NewmodelwithWGS_version2(Temps(4), [VAR(1) VAR(2)
VAR(3) VAR(4)], [VAR(5) VAR(6) VAR(7) VAR(8)], [0.01*COH2(5)  0.21*10 0
0.99*COH2(5)  0 0.79*10], [VAR(9) VAR(10) VAR(11) VAR(12) VAR(13) VAR(14)
VAR(15) VAR(16)]);      % 10 sccm Air 100 sccm COH2

% Conversionresults(21) = NewmodelwithWGS_version2(Temps(5), [VAR(1) VAR(2)
VAR(3) VAR(4)], [VAR(5) VAR(6) VAR(7) VAR(8)], [0.01*COH2(1)  0.21*10 0
0.99*COH2(1)  0 0.79*10]);      % 10 sccm Air 20 sccm COH2
Conversionresults(18) = NewmodelwithWGS_version2(Temps(5), [VAR(1) VAR(2)
VAR(3) VAR(4)], [VAR(5) VAR(6) VAR(7) VAR(8)], [0.01*COH2(2)  0.21*10 0
0.99*COH2(2)  0 0.79*10], [VAR(9) VAR(10) VAR(11) VAR(12) VAR(13) VAR(14)
VAR(15) VAR(16)]);      % 10 sccm Air 40 sccm COH2
Conversionresults(19) = NewmodelwithWGS_version2(Temps(5), [VAR(1) VAR(2)
VAR(3) VAR(4)], [VAR(5) VAR(6) VAR(7) VAR(8)], [0.01*COH2(3)  0.21*10 0
0.99*COH2(3)  0 0.79*10], [VAR(9) VAR(10) VAR(11) VAR(12) VAR(13) VAR(14)
VAR(15) VAR(16)]);      % 10 sccm Air 60 sccm COH2
Conversionresults(20) = NewmodelwithWGS_version2(Temps(5), [VAR(1) VAR(2)
VAR(3) VAR(4)], [VAR(5) VAR(6) VAR(7) VAR(8)], [0.01*COH2(4)  0.21*10 0
0.99*COH2(4)  0 0.79*10], [VAR(9) VAR(10) VAR(11) VAR(12) VAR(13) VAR(14)
VAR(15) VAR(16)]);      % 10 sccm Air 80 sccm COH2
Conversionresults(21) = NewmodelwithWGS_version2(Temps(5), [VAR(1) VAR(2)
VAR(3) VAR(4)], [VAR(5) VAR(6) VAR(7) VAR(8)], [0.01*COH2(5)  0.21*10 0
0.99*COH2(5)  0 0.79*10], [VAR(9) VAR(10) VAR(11) VAR(12) VAR(13) VAR(14)
VAR(15) VAR(16)]);      % 10 sccm Air 100 sccm COH2

Appendix A (Continued)

A.4  General Comprehensive Model

```
function ConversionresultsCO = NewmodelwithWGS_version2(T, alpha, E, Flowrates,
Exponents)
% NewmodelwithWGS(T, alpha, E, Flowrates, Exponents)
% Temperature(C), alpha, E, Flowrates(sccm), Exponents(CO, O2, CO2, H2, CO, H2O)

% Information needed,
% Temperature, reaction rate constants(alphas and E's), Flow rates of gases
%
% Information attained
% Approximate conversions for all species

clc;
% New thought process

% CO + 1/2O2 = CO2          (1)
% H2 + 1/2O2 = H2O        (2)
% CO2 + H2 = CO + H2O        (3)
% CO + H2O = CO2 + H2      (4)

T = T + 273.15;                    % Temperature (K)
R = 8.314;                      % R = J/mol*K
k(1) = alpha(1)*exp(-E(1)/(R*T));
k(2) = alpha(2)*exp(-E(2)/(R*T));
k(3) = alpha(3)*exp(-E(3)/(R*T));
k(4) = alpha(4)*exp(-E(4)/(R*T));

% Fo = [1 2 0 99 0 8]';            % Initial Flowrates (sccm)
Fo = Flowrates./600;              % Initial Flowrates (L/s)

CTo = 1/(0.0821*T);                % CTo = Po/(R*To)   % mol/L  where R in this case
is (L*atm/mol K)
weight_int = 0;                % Weight (g)
weight_final = 0.1;             % Weight (g)

[W, C_rk1] = RK(@funct, weight_int, weight_final, weight_final/1000, Fo, 4, k, CTo,
Exponents);

% Conversionresults = (C_rk1(:,1) - C_rk1(:,end))./C_rk1(:,1);
Conversionresults = (C_rk1(1,1) - C_rk1(1,end))./C_rk1(1,1);  % Changed "all rows" to
one to speed up calculations Conversionresults = (C_rk1(:,1) - C_rk1(:,end))./C_rk1(:,1);
ConversionresultsCO = Conversionresults(1);
```

Appendix A (Continued)


```
function dCs = funct(W, C, k, CTo, Exponents)

FCO  = C(1);
FO2  = C(2);
FCO2 = C(3);
FH2  = C(4);
FH2O = C(5);
FN2  = C(6);

FT = FCO + FO2 + FCO2 + FH2 + FH2O + FN2;

CCO  = CTo*FCO/FT;
CO2  = CTo*FO2/FT;
CCO2 = CTo*FCO2/FT;
CH2  = CTo*FH2/FT;
CH2O = CTo*FH2O/FT;

r1CO = -k(1)*CCO^Exponents(1)*CO2^(Exponents(2));
r1O2 = 1/2*r1CO;
r1CO2 = -r1CO;

r2H2 = -k(2)*CH2^Exponents(3)*CO2^(Exponents(4));
r2O2 = 1/2*r2H2;
r2H2O = -r2H2;

r3H2 = -k(3)*CCO2^Exponents(5)*CH2^Exponents(6);
r3CO2 = r3H2;
r3CO = -r3H2;
r3H2O = -r3H2;

r4CO = -k(4)*CCO^Exponents(7)*CH2O^Exponents(8);
r4H2O = r4CO;
r4CO2 = -r4CO;
r4H2 = -r4CO;

rCO  = r1CO  + r3CO  + r4CO;
rO2  = r1O2 + r2O2;
rCO2 = r1CO2 + r3CO2 + r4CO2;
rH2  = r2H2 + r3H2  + r4H2;
rH2O = r2H2O + r3H2O + r4H2O;

dFCO = rCO;
```

Appendix A (Continued)

```
dFO2 = rO2;
dFCO2 = rCO2;
dFH2 = rH2;
dFH2O = rH2O;
dFN2 = 0;


dCs = [dFCO dFO2 dFCO2 dFH2 dFH2O dFN2]';
```


A.5  Independent Elementary Model Fit Routine

```
function Final = IndependentReactionModelFit_Non(Initialguesses)
% Edit
% I removed some of the errant points to get a better fit
close all; clc;

% conversionCO = [0.5583 0.4195 0.3694 0.3932 0.3696 0.4674 0.3999 0.3545 0.3361
0.3533 0.4173 0.3181 0.2714 0.2414 0.2388 0.3318 0.2410 0.1982 0.1697 0.1667 0.2837
0.1576 0.1439 0.1229 0.1165];
conversionCO = [0.5583 0.3932 0.3696 0.4674 0.3999 0.3545 0.3361 0.4173 0.3181
0.2714 0.2414 0.2388 0.3318 0.2410 0.1982 0.1697 0.1667 0.1576 0.1439 0.1229
0.1165];
Temps  = [25 50 75 100 125];
Keq    = [104000 28800 9620 3730 1640];
Air    = [10 10 10 10 10];
COH2   = [20 40 60 80 100];

data = [Temps; Keq; Air; COH2];

[Final,RESNORM,RESIDUAL,EXITFLAG,OUTPUT,LAMBDA,JACOBIAN] =
lsqcurvefit(@myfun, Initialguesses, data, conversionCO, [0 0 0 0], [+inf +inf 50000
50000])


function Conversionresults = myfun(VAR, data);

Temps = data(1,:);
Keq   = data(2,:);
Air   = data(3,:);
COH2  = data(4,:);

% Conversionresults = IndependentReactionModel_3reaction(Temperature, alpha, E,
[CO O2 CO2 H2 H2O N2])
```

Appendix A (Continued)

```
Conversionresults(1) = IndependentReactionModel_3reaction(Temps(1), Keq(1),
[VAR(1) VAR(2)], [VAR(3) VAR(4)], [0.01*COH2(1)  0.21*10 0 0.99*COH2(1)  0
0.79*10], [1 0.5 1 1 1 1]);     % 10 sccm Air 20 sccm COH2
% Conversionresults(2) = IndependentReactionModel_3reaction(Temps(1), Keq(1),
[VAR(1) VAR(2)], [VAR(3) VAR(4)], [0.01*COH2(2)  0.21*10 0 0.99*COH2(2)  0
0.79*10]);     % 10 sccm Air 40 sccm COH2
% Conversionresults(3) = IndependentReactionModel_3reaction(Temps(1), Keq(1),
[VAR(1) VAR(2)], [VAR(3) VAR(4)], [0.01*COH2(3)  0.21*10 0 0.99*COH2(3)  0
0.79*10]);     % 10 sccm Air 60 sccm COH2
Conversionresults(2) = IndependentReactionModel_3reaction(Temps(1), Keq(1),
[VAR(1) VAR(2)], [VAR(3) VAR(4)], [0.01*COH2(4)  0.21*10 0 0.99*COH2(4)  0
0.79*10], [1 0.5 1 1 1 1]);     % 10 sccm Air 80 sccm COH2
Conversionresults(3) = IndependentReactionModel_3reaction(Temps(1), Keq(1),
[VAR(1) VAR(2)], [VAR(3) VAR(4)], [0.01*COH2(5)  0.21*10 0 0.99*COH2(5)  0
0.79*10], [1 0.5 1 1 1 1]);     % 10 sccm Air 100 sccm COH2

Conversionresults(4) = IndependentReactionModel_3reaction(Temps(2), Keq(2),
[VAR(1) VAR(2)], [VAR(3) VAR(4)], [0.01*COH2(1)  0.21*10 0 0.99*COH2(1)  0
0.79*10], [1 0.5 1 1 1 1]);     % 10 sccm Air 20 sccm COH2
Conversionresults(5) = IndependentReactionModel_3reaction(Temps(2), Keq(2),
[VAR(1) VAR(2)], [VAR(3) VAR(4)], [0.01*COH2(2)  0.21*10 0 0.99*COH2(2)  0
0.79*10], [1 0.5 1 1 1 1]);     % 10 sccm Air 40 sccm COH2
Conversionresults(6) = IndependentReactionModel_3reaction(Temps(2), Keq(2),
[VAR(1) VAR(2)], [VAR(3) VAR(4)], [0.01*COH2(3)  0.21*10 0 0.99*COH2(3)  0
0.79*10], [1 0.5 1 1 1 1]);     % 10 sccm Air 60 sccm COH2
Conversionresults(7) = IndependentReactionModel_3reaction(Temps(2), Keq(2),
[VAR(1) VAR(2)], [VAR(3) VAR(4)], [0.01*COH2(4)  0.21*10 0 0.99*COH2(4)  0
0.79*10], [1 0.5 1 1 1 1]);     % 10 sccm Air 80 sccm COH2
% Conversionresults(10) = IndependentReactionModel_3reaction(Temps(2), Keq(2),
[VAR(1) VAR(2)], [VAR(3) VAR(4)], [0.01*COH2(5) 0.21*10 0 0.99*COH2(5)  0
0.79*10]);     % 10 sccm Air 100 sccm COH2

Conversionresults(8) = IndependentReactionModel_3reaction(Temps(3), Keq(3),
[VAR(1) VAR(2)], [VAR(3) VAR(4)], [0.01*COH2(1)  0.21*10 0 0.99*COH2(1)  0
0.79*10], [1 0.5 1 1 1 1]);     % 10 sccm Air 20 sccm COH2
Conversionresults(9) = IndependentReactionModel_3reaction(Temps(3), Keq(3),
[VAR(1) VAR(2)], [VAR(3) VAR(4)], [0.01*COH2(2)  0.21*10 0 0.99*COH2(2)  0
0.79*10], [1 0.5 1 1 1 1]);     % 10 sccm Air 40 sccm COH2
Conversionresults(10) = IndependentReactionModel_3reaction(Temps(3), Keq(3),
[VAR(1) VAR(2)], [VAR(3) VAR(4)], [0.01*COH2(3)  0.21*10 0 0.99*COH2(3)  0
0.79*10], [1 0.5 1 1 1 1]);     % 10 sccm Air 60 sccm COH2
```

Appendix A (Continued)

Conversionresults(11) = IndependentReactionModel_3reaction(Temps(3), Keq(3), [VAR(1) VAR(2)], [VAR(3) VAR(4)], [0.01*COH2(4)  0.21*10 0 0.99*COH2(4)  0 0.79*10], [1 0.5 1 1 1 1]);     % 10 sccm Air 80 sccm COH2
Conversionresults(12) = IndependentReactionModel_3reaction(Temps(3), Keq(3), [VAR(1) VAR(2)], [VAR(3) VAR(4)], [0.01*COH2(5)  0.21*10 0 0.99*COH2(5)  0 0.79*10], [1 0.5 1 1 1 1]);     % 10 sccm Air 100 sccm COH2

Conversionresults(13) = IndependentReactionModel_3reaction(Temps(4), Keq(4), [VAR(1) VAR(2)], [VAR(3) VAR(4)], [0.01*COH2(1)  0.21*10 0 0.99*COH2(1)  0 0.79*10], [1 0.5 1 1 1 1]);     % 10 sccm Air 20 sccm COH2
Conversionresults(14) = IndependentReactionModel_3reaction(Temps(4), Keq(4), [VAR(1) VAR(2)], [VAR(3) VAR(4)], [0.01*COH2(2)  0.21*10 0 0.99*COH2(2)  0 0.79*10], [1 0.5 1 1 1 1]);     % 10 sccm Air 40 sccm COH2
Conversionresults(15) = IndependentReactionModel_3reaction(Temps(4), Keq(4), [VAR(1) VAR(2)], [VAR(3) VAR(4)], [0.01*COH2(3)  0.21*10 0 0.99*COH2(3)  0 0.79*10], [1 0.5 1 1 1 1]);     % 10 sccm Air 60 sccm COH2
Conversionresults(16) = IndependentReactionModel_3reaction(Temps(4), Keq(4), [VAR(1) VAR(2)], [VAR(3) VAR(4)], [0.01*COH2(4)  0.21*10 0 0.99*COH2(4)  0 0.79*10], [1 0.5 1 1 1 1]);     % 10 sccm Air 80 sccm COH2
Conversionresults(17) = IndependentReactionModel_3reaction(Temps(4), Keq(4), [VAR(1) VAR(2)], [VAR(3) VAR(4)], [0.01*COH2(5)  0.21*10 0 0.99*COH2(5)  0 0.79*10], [1 0.5 1 1 1 1]);     % 10 sccm Air 100 sccm COH2

% Conversionresults(21) = IndependentReactionModel_3reaction(Temps(5), Keq(5), [VAR(1) VAR(2)], [VAR(3) VAR(4)], [0.01*COH2(1)  0.21*10 0 0.99*COH2(1)  0 0.79*10]);     % 10 sccm Air 20 sccm COH2
Conversionresults(18) = IndependentReactionModel_3reaction(Temps(5), Keq(5), [VAR(1) VAR(2)], [VAR(3) VAR(4)], [0.01*COH2(2)  0.21*10 0 0.99*COH2(2)  0 0.79*10], [1 0.5 1 1 1 1]);     % 10 sccm Air 40 sccm COH2
Conversionresults(19) = IndependentReactionModel_3reaction(Temps(5), Keq(5), [VAR(1) VAR(2)], [VAR(3) VAR(4)], [0.01*COH2(3)  0.21*10 0 0.99*COH2(3)  0 0.79*10], [1 0.5 1 1 1 1]);     % 10 sccm Air 60 sccm COH2
Conversionresults(20) = IndependentReactionModel_3reaction(Temps(5), Keq(5), [VAR(1) VAR(2)], [VAR(3) VAR(4)], [0.01*COH2(4)  0.21*10 0 0.99*COH2(4)  0 0.79*10], [1 0.5 1 1 1 1]);     % 10 sccm Air 80 sccm COH2
Conversionresults(21) = IndependentReactionModel_3reaction(Temps(5), Keq(5), [VAR(1) VAR(2)], [VAR(3) VAR(4)], [0.01*COH2(5)  0.21*10 0 0.99*COH2(5)  0 0.79*10], [1 0.5 1 1 1 1]);     % 10 sccm Air 100 sccm COH2


A.6  Independent Non-Elementary Model Fit Routine

function Final = IndependentReactionModelFit_Non(Initialguesses)

Appendix A (Continued)

```matlab
% Edit
% I removed some of the errant points to get a better fit
close all; clc;

% conversionCO = [0.5583 0.4195 0.3694 0.3932 0.3696 0.4674 0.3999 0.3545 0.3361
0.3533 0.4173 0.3181 0.2714 0.2414 0.2388 0.3318 0.2410 0.1982 0.1697 0.1667 0.2837
0.1576 0.1439 0.1229 0.1165];
conversionCO = [0.5583 0.3932 0.3696 0.4674 0.3999 0.3545 0.3361 0.4173 0.3181
0.2714 0.2414 0.2388 0.3318 0.2410 0.1982 0.1697 0.1667 0.1576 0.1439 0.1229
0.1165];
Temps  = [25 50 75 100 125];
Keq    = [104000 28800 9620 3730 1640];
Air    = [10 10 10 10 10];
COH2   = [20 40 60 80 100];

data = [Temps; Keq; Air; COH2];

% [Final,RESNORM,RESIDUAL,EXITFLAG,OUTPUT,LAMBDA,JACOBIAN] =
lsqcurvefit(@myfun, Initialguesses, data, conversionCO, [0 0 0 0 -2 -2 -2 -2 -2 -2], [+inf
+inf 50000 50000 2 2 2 2 2 2])
[Final,RESNORM,RESIDUAL,EXITFLAG,OUTPUT,LAMBDA,JACOBIAN] =
lsqcurvefit(@myfun, Initialguesses, data, conversionCO, [0 0 0 0 0 0 0 0 0 0 0], [+inf +inf
+inf +inf 3 3 3 3 3 3])

function Conversionresults = myfun(VAR, data);

Temps = data(1,:);
Keq   = data(2,:);
Air   = data(3,:);
COH2  = data(4,:);

%  Conversionresults = IndependentReactionModel_3reaction(Temperature, alpha, E,
[CO O2 CO2 H2 H2O N2])
Conversionresults(1) = IndependentReactionModel_3reaction(Temps(1), Keq(1),
[VAR(1) VAR(2)], [VAR(3) VAR(4)], [0.01*COH2(1)  0.21*10 0 0.99*COH2(1)  0
0.79*10], [VAR(5) VAR(6) VAR(7) VAR(8) VAR(9) VAR(10)]);     % 10 sccm Air 20
sccm COH2
% Conversionresults(2) = IndependentReactionModel_3reaction(Temps(1), Keq(1),
[VAR(1) VAR(2)], [VAR(3) VAR(4)], [0.01*COH2(2)  0.21*10 0 0.99*COH2(2)  0
0.79*10]);     % 10 sccm Air 40 sccm COH2
% Conversionresults(3) = IndependentReactionModel_3reaction(Temps(1), Keq(1),
[VAR(1) VAR(2)], [VAR(3) VAR(4)], [0.01*COH2(3)  0.21*10 0 0.99*COH2(3)  0
0.79*10]);     % 10 sccm Air 60 sccm COH2
```

Appendix A (Continued)

Conversionresults(2) = IndependentReactionModel_3reaction(Temps(1), Keq(1), [VAR(1) VAR(2)], [VAR(3) VAR(4)], [0.01*COH2(4)  0.21*10 0 0.99*COH2(4)  0 0.79*10], [VAR(5) VAR(6) VAR(7) VAR(8) VAR(9) VAR(10)]);     % 10 sccm Air 80 sccm COH2
Conversionresults(3) = IndependentReactionModel_3reaction(Temps(1), Keq(1), [VAR(1) VAR(2)], [VAR(3) VAR(4)], [0.01*COH2(5)  0.21*10 0 0.99*COH2(5)  0 0.79*10], [VAR(5) VAR(6) VAR(7) VAR(8) VAR(9) VAR(10)]);     % 10 sccm Air 100 sccm COH2

Conversionresults(4) = IndependentReactionModel_3reaction(Temps(2), Keq(2), [VAR(1) VAR(2)], [VAR(3) VAR(4)], [0.01*COH2(1)  0.21*10 0 0.99*COH2(1)  0 0.79*10], [VAR(5) VAR(6) VAR(7) VAR(8) VAR(9) VAR(10)]);     % 10 sccm Air 20 sccm COH2
Conversionresults(5) = IndependentReactionModel_3reaction(Temps(2), Keq(2), [VAR(1) VAR(2)], [VAR(3) VAR(4)], [0.01*COH2(2)  0.21*10 0 0.99*COH2(2)  0 0.79*10], [VAR(5) VAR(6) VAR(7) VAR(8) VAR(9) VAR(10)]);     % 10 sccm Air 40 sccm COH2
Conversionresults(6) = IndependentReactionModel_3reaction(Temps(2), Keq(2), [VAR(1) VAR(2)], [VAR(3) VAR(4)], [0.01*COH2(3)  0.21*10 0 0.99*COH2(3)  0 0.79*10], [VAR(5) VAR(6) VAR(7) VAR(8) VAR(9) VAR(10)]);     % 10 sccm Air 60 sccm COH2
Conversionresults(7) = IndependentReactionModel_3reaction(Temps(2), Keq(2), [VAR(1) VAR(2)], [VAR(3) VAR(4)], [0.01*COH2(4)  0.21*10 0 0.99*COH2(4)  0 0.79*10], [VAR(5) VAR(6) VAR(7) VAR(8) VAR(9) VAR(10)]);     % 10 sccm Air 80 sccm COH2
% Conversionresults(10) = IndependentReactionModel_3reaction(Temps(2), Keq(2), [VAR(1) VAR(2)], [VAR(3) VAR(4)], [0.01*COH2(5) 0.21*10 0 0.99*COH2(5)  0 0.79*10]);     % 10 sccm Air 100 sccm COH2

Conversionresults(8) = IndependentReactionModel_3reaction(Temps(3), Keq(3), [VAR(1) VAR(2)], [VAR(3) VAR(4)], [0.01*COH2(1)  0.21*10 0 0.99*COH2(1)  0 0.79*10], [VAR(5) VAR(6) VAR(7) VAR(8) VAR(9) VAR(10)]);     % 10 sccm Air 20 sccm COH2
Conversionresults(9) = IndependentReactionModel_3reaction(Temps(3), Keq(3), [VAR(1) VAR(2)], [VAR(3) VAR(4)], [0.01*COH2(2)  0.21*10 0 0.99*COH2(2)  0 0.79*10], [VAR(5) VAR(6) VAR(7) VAR(8) VAR(9) VAR(10)]);     % 10 sccm Air 40 sccm COH2
Conversionresults(10) = IndependentReactionModel_3reaction(Temps(3), Keq(3), [VAR(1) VAR(2)], [VAR(3) VAR(4)], [0.01*COH2(3)  0.21*10 0 0.99*COH2(3)  0 0.79*10], [VAR(5) VAR(6) VAR(7) VAR(8) VAR(9) VAR(10)]);     % 10 sccm Air 60 sccm COH2
Conversionresults(11) = IndependentReactionModel_3reaction(Temps(3), Keq(3), [VAR(1) VAR(2)], [VAR(3) VAR(4)], [0.01*COH2(4)  0.21*10 0 0.99*COH2(4)  0

0.79*10], [VAR(5) VAR(6) VAR(7) VAR(8) VAR(9) VAR(10)]);      % 10 sccm Air 80 sccm COH2

Conversionresults(12) = IndependentReactionModel_3reaction(Temps(3), Keq(3), [VAR(1) VAR(2)], [VAR(3) VAR(4)], [0.01*COH2(5)  0.21*10 0 0.99*COH2(5)  0 0.79*10], [VAR(5) VAR(6) VAR(7) VAR(8) VAR(9) VAR(10)]);      % 10 sccm Air 100 sccm COH2


Conversionresults(13) = IndependentReactionModel_3reaction(Temps(4), Keq(4), [VAR(1) VAR(2)], [VAR(3) VAR(4)], [0.01*COH2(1)  0.21*10 0 0.99*COH2(1)  0 0.79*10], [VAR(5) VAR(6) VAR(7) VAR(8) VAR(9) VAR(10)]);      % 10 sccm Air 20 sccm COH2

Conversionresults(14) = IndependentReactionModel_3reaction(Temps(4), Keq(4), [VAR(1) VAR(2)], [VAR(3) VAR(4)], [0.01*COH2(2)  0.21*10 0 0.99*COH2(2)  0 0.79*10], [VAR(5) VAR(6) VAR(7) VAR(8) VAR(9) VAR(10)]);      % 10 sccm Air 40 sccm COH2

Conversionresults(15) = IndependentReactionModel_3reaction(Temps(4), Keq(4), [VAR(1) VAR(2)], [VAR(3) VAR(4)], [0.01*COH2(3)  0.21*10 0 0.99*COH2(3)  0 0.79*10], [VAR(5) VAR(6) VAR(7) VAR(8) VAR(9) VAR(10)]);      % 10 sccm Air 60 sccm COH2

Conversionresults(16) = IndependentReactionModel_3reaction(Temps(4), Keq(4), [VAR(1) VAR(2)], [VAR(3) VAR(4)], [0.01*COH2(4)  0.21*10 0 0.99*COH2(4)  0 0.79*10], [VAR(5) VAR(6) VAR(7) VAR(8) VAR(9) VAR(10)]);      % 10 sccm Air 80 sccm COH2

Conversionresults(17) = IndependentReactionModel_3reaction(Temps(4), Keq(4), [VAR(1) VAR(2)], [VAR(3) VAR(4)], [0.01*COH2(5)  0.21*10 0 0.99*COH2(5)  0 0.79*10], [VAR(5) VAR(6) VAR(7) VAR(8) VAR(9) VAR(10)]);      % 10 sccm Air 100 sccm COH2


% Conversionresults(21) = IndependentReactionModel_3reaction(Temps(5), Keq(5), [VAR(1) VAR(2)], [VAR(3) VAR(4)], [0.01*COH2(1)  0.21*10 0 0.99*COH2(1)  0 0.79*10]);      % 10 sccm Air 20 sccm COH2

Conversionresults(18) = IndependentReactionModel_3reaction(Temps(5), Keq(5), [VAR(1) VAR(2)], [VAR(3) VAR(4)], [0.01*COH2(2)  0.21*10 0 0.99*COH2(2)  0 0.79*10], [VAR(5) VAR(6) VAR(7) VAR(8) VAR(9) VAR(10)]);      % 10 sccm Air 40 sccm COH2

Conversionresults(19) = IndependentReactionModel_3reaction(Temps(5), Keq(5), [VAR(1) VAR(2)], [VAR(3) VAR(4)], [0.01*COH2(3)  0.21*10 0 0.99*COH2(3)  0 0.79*10], [VAR(5) VAR(6) VAR(7) VAR(8) VAR(9) VAR(10)]);      % 10 sccm Air 60 sccm COH2

Conversionresults(20) = IndependentReactionModel_3reaction(Temps(5), Keq(5), [VAR(1) VAR(2)], [VAR(3) VAR(4)], [0.01*COH2(4)  0.21*10 0 0.99*COH2(4)  0 0.79*10], [VAR(5) VAR(6) VAR(7) VAR(8) VAR(9) VAR(10)]);      % 10 sccm Air 80 sccm COH2

Appendix A (Continued)

Conversionresults(21) = IndependentReactionModel_3reaction(Temps(5), Keq(5), [VAR(1) VAR(2)], [VAR(3) VAR(4)], [0.01*COH2(5)  0.21*10 0 0.99*COH2(5)  0 0.79*10], [VAR(5) VAR(6) VAR(7) VAR(8) VAR(9) VAR(10)]);     % 10 sccm Air 100 sccm COH2


A.7  General Independent Model

function ConversionresultsCO = IndependentReactionModel_3reaction(T, Keq, alpha, E, Flowrates, Exponents)

clc;

```
% CO + 1/2O2 = CO2          (1)
% CO2 + H2 = CO + H2O       (2)
% CO + H2O = CO2 + H2       (3)


T = T + 273.15;                    % Temperature (K)
R = 8.314;                         % R = J/mol*K
k(1) = alpha(1)*exp(-E(1)/(R*T));
k(2) = alpha(2)*exp(-E(2)/(R*T));
k(3) = k(2)*Keq;


% Fo = [CO, O2, CO2, H2, CO, H2O]';          % Initial Flowrates(sccm)
Fo = Flowrates./600;               % Initial Flowrates (L/s)
CTo = 1/(0.0821*T);                % CTo = Po/(R*To)   % mol/L  where R in this case
is (L*atm/mol K)
weight_int = 0;                    % Weight (g)
weight_final = 0.1;                % Weight (g)

[W, C_rk1] = RK(@funct, weight_int, weight_final, weight_final/1000, Fo, 4, k, CTo, Exponents);

% Conversionresults = (C_rk1(:,1) - C_rk1(:,end))./C_rk1(:,1);
Conversionresults = (C_rk1(1,1) - C_rk1(1,end))./C_rk1(1,1);  % Changed "all rows" to
one to speed up calculations Conversionresults = (C_rk1(:,1) - C_rk1(:,end))./C_rk1(:,1);
ConversionresultsCO = Conversionresults(1);

function dCs = funct(W, C, k, CTo, Exponents)

FCO  = C(1);
FO2  = C(2);
```

Appendix A (Continued)

```
FCO2 = C(3);
FH2  = C(4);
FH2O = C(5);
FN2  = C(6);

FT = FCO + FO2 + FCO2 + FH2 + FH2O + FN2;

CCO  = CTo*FCO/FT;
CO2  = CTo*FO2/FT;
CCO2 = CTo*FCO2/FT;
CH2  = CTo*FH2/FT;
CH2O = CTo*FH2O/FT;

r1CO = -k(1)*CCO^Exponents(1)*CO2^(Exponents(2));
r1O2 = 1/2*r1CO;
r1CO2 = -r1CO;

r2H2 = -k(2)*CCO2^Exponents(3)*CH2^Exponents(4);
r2CO2 = r2H2;
r2CO = -r2H2;
r2H2O = -r2H2;

r3CO = -k(3)*CCO^Exponents(5)*CH2O^Exponents(6);
r3H2O = r3CO;
r3CO2 = -r3CO;
r3H2 = -r3CO;

rCO  = r1CO  + r2CO  + r3CO;
rO2  = r1O2;
rCO2 = r1CO2 + r2CO2 + r3CO2;
rH2  = r2H2  + r3H2;
rH2O = r2H2O + r3H2O;

dFCO = rCO;
dFO2 = rO2;
dFCO2 = rCO2;
dFH2 = rH2;
dFH2O = rH2O;
dFN2 = 0;

dCs = [dFCO dFO2 dFCO2 dFH2 dFH2O dFN2]';
```

Appendix A (Continued)

A.8  Error Calculations for WGC Data

```
% clc; close all; clear all;
load FTIRdata_vars
clc; close all;

[Xrange, COrange, CO2range, H2Orange] = defineranges(background_3.data(:,1));
% Extra function defined elsewhere

% Full FTIR signal of flow rates

bypass_20rat1 = -(log10(bypass20_1.data(:,2)./background_1.data(:,2)));
% Determine absorbance
bypass_20rat2 = -(log10(bypass20_2.data(:,2)./background_1.data(:,2)));
% Determine absorbance
bypass_40rat1 = -(log10(bypass40_1.data(:,2)./background_1.data(:,2)));
bypass_40rat2 = -(log10(bypass40_2.data(:,2)./background_1.data(:,2)));
bypass_40rat3 = -(log10(bypass40_3.data(:,2)./background_1.data(:,2)));
bypass_40rat4 = -(log10(bypass40_4.data(:,2)./background_1.data(:,2)));
bypass_60rat1 = -(log10(bypass60_1.data(:,2)./background_1.data(:,2)));
bypass_60rat2 = -(log10(bypass60_2.data(:,2)./background_1.data(:,2)));
bypass_60rat3 = -(log10(bypass60_3.data(:,2)./background_1.data(:,2)));
bypass_60rat4 = -(log10(bypass60_4.data(:,2)./background_1.data(:,2)));
bypass_80rat1 = -(log10(bypass80_1.data(:,2)./background_1.data(:,2)));
bypass_80rat2 = -(log10(bypass80_2.data(:,2)./background_1.data(:,2)));
bypass_80rat3 = -(log10(bypass80_3.data(:,2)./background_1.data(:,2)));
bypass_80rat4 = -(log10(bypass80_4.data(:,2)./background_1.data(:,2)));
bypass_100rat1 = -(log10(bypass100_1.data(:,2)./background_1.data(:,2)));
bypass_100rat2 = -(log10(bypass100_2.data(:,2)./background_1.data(:,2)));
bypass_100rat3 = -(log10(bypass100_3.data(:,2)./background_1.data(:,2)));
bypass_100rat4 = -(log10(bypass100_4.data(:,2)./background_1.data(:,2)));

Integralbypass_201 = integratedata(bypass20_1.data(:,1), bypass_20rat1, COrange);
% Extra function defined elsewhere
Integralbypass_202 = integratedata(bypass20_2.data(:,1), bypass_20rat2, COrange);
% Extra function defined elsewhere
Integralbypass_401 = integratedata(bypass40_1.data(:,1), bypass_40rat1, COrange);
% Extra function defined elsewhere
Integralbypass_402 = integratedata(bypass40_2.data(:,1), bypass_40rat2, COrange);
% Extra function defined elsewhere
Integralbypass_403 = integratedata(bypass40_3.data(:,1), bypass_40rat3, COrange);
% Extra function defined elsewhere
```

104

Appendix A (Continued)

```
Integralbypass_404 = integratedata(bypass40_4.data(:,1), bypass_40rat4, COrange);
% Extra function defined elsewhere
Integralbypass_601 = integratedata(bypass60_1.data(:,1), bypass_60rat1, COrange);
% Extra function defined elsewhere
Integralbypass_602 = integratedata(bypass60_2.data(:,1), bypass_60rat2, COrange);
% Extra function defined elsewhere
Integralbypass_603 = integratedata(bypass60_3.data(:,1), bypass_60rat3, COrange);
% Extra function defined elsewhere
Integralbypass_604 = integratedata(bypass60_4.data(:,1), bypass_60rat4, COrange);
% Extra function defined elsewhere
Integralbypass_801 = integratedata(bypass80_1.data(:,1), bypass_80rat1, COrange);
% Extra function defined elsewhere
Integralbypass_802 = integratedata(bypass80_2.data(:,1), bypass_80rat2, COrange);
% Extra function defined elsewhere
Integralbypass_803 = integratedata(bypass80_3.data(:,1), bypass_80rat3, COrange);
% Extra function defined elsewhere
Integralbypass_804 = integratedata(bypass80_4.data(:,1), bypass_80rat4, COrange);
% Extra function defined elsewhere
Integralbypass_1001 = integratedata(bypass100_1.data(:,1), bypass_100rat1, COrange);
% Extra function defined elsewhere
Integralbypass_1002 = integratedata(bypass100_2.data(:,1), bypass_100rat2, COrange);
% Extra function defined elsewhere
Integralbypass_1003 = integratedata(bypass100_3.data(:,1), bypass_100rat3, COrange);
% Extra function defined elsewhere
Integralbypass_1004 = integratedata(bypass100_4.data(:,1), bypass_100rat4, COrange);
% Extra function defined elsewhere

bypass_20 = [Integralbypass_201 Integralbypass_202]
bypass_40 = [Integralbypass_401 Integralbypass_402 Integralbypass_403
Integralbypass_404]
bypass_60 = [Integralbypass_601 Integralbypass_602 Integralbypass_603
Integralbypass_604]
bypass_80 = [Integralbypass_801 Integralbypass_802 Integralbypass_803
Integralbypass_804]
bypass_100 = [Integralbypass_1001 Integralbypass_1002 Integralbypass_1003
Integralbypass_1004]

mean20 = mean(bypass_20)
mean40 = mean(bypass_40)
mean60 = mean(bypass_60)
mean80 = mean(bypass_80)
mean100 = mean(bypass_100)
```

Appendix A (Continued)

```
std20 = std(bypass_20)
std40 = std(bypass_40)
std60 = std(bypass_60)
std80 = std(bypass_80)
std100 = std(bypass_100)

% 25oC FTIR data
pr25oC_20rat1 = -(log10(pr25_20sccm1.data(:,2)./background_1.data(:,2)));
% Determine absorbance
pr25oC_20rat2 = -(log10(pr25_20sccm2.data(:,2)./background_1.data(:,2)));
% Determine absorbance
pr25oC_20rat3 = -(log10(pr25_20sccm3.data(:,2)./background_1.data(:,2)));
% Determine absorbance
pr25oC_40rat1 = -(log10(pr25_40sccm1.data(:,2)./background_1.data(:,2)));
pr25oC_40rat2 = -(log10(pr25_40sccm2.data(:,2)./background_1.data(:,2)));
pr25oC_40rat3 = -(log10(pr25_40sccm3.data(:,2)./background_1.data(:,2)));
pr25oC_60rat1 = -(log10(pr25_60sccm1.data(:,2)./background_1.data(:,2)));
pr25oC_60rat2 = -(log10(pr25_60sccm2.data(:,2)./background_1.data(:,2)));
pr25oC_60rat3 = -(log10(pr25_60sccm3.data(:,2)./background_1.data(:,2)));
pr25oC_80rat1 = -(log10(pr25_80sccm1.data(:,2)./background_1.data(:,2)));
pr25oC_80rat2 = -(log10(pr25_80sccm2.data(:,2)./background_1.data(:,2)));
pr25oC_80rat3 = -(log10(pr25_80sccm3.data(:,2)./background_1.data(:,2)));
pr25oC_100rat1 = -(log10(pr25_100sccm1.data(:,2)./background_1.data(:,2)));
pr25oC_100rat2 = -(log10(pr25_100sccm2.data(:,2)./background_1.data(:,2)));
pr25oC_100rat3 = -(log10(pr25_100sccm3.data(:,2)./background_1.data(:,2)));
pr25oC_100rat4 = -(log10(pr25_100sccm4.data(:,2)./background_1.data(:,2)));

Integral25oc_201 = integratedata(pr25_20sccm1.data(:,1), pr25oC_20rat1, COrange);
% Extra function defined elsewhere
Integral25oc_202 = integratedata(pr25_20sccm2.data(:,1), pr25oC_20rat2, COrange);
% Extra function defined elsewhere
Integral25oc_203 = integratedata(pr25_20sccm3.data(:,1), pr25oC_20rat3, COrange);
% Extra function defined elsewhere
Integral25oc_401 = integratedata(pr25_40sccm1.data(:,1), pr25oC_40rat1, COrange);
% Extra function defined elsewhere
Integral25oc_402 = integratedata(pr25_40sccm2.data(:,1), pr25oC_40rat2, COrange);
% Extra function defined elsewhere
Integral25oc_403 = integratedata(pr25_40sccm3.data(:,1), pr25oC_40rat3, COrange);
% Extra function defined elsewhere
Integral25oc_601 = integratedata(pr25_60sccm1.data(:,1), pr25oC_60rat1, COrange);
% Extra function defined elsewhere
Integral25oc_602 = integratedata(pr25_60sccm2.data(:,1), pr25oC_60rat2, COrange);
% Extra function defined elsewhere
```

Appendix A (Continued)

```
Integral25oc_603 = integratedata(pr25_60sccm3.data(:,1), pr25oC_60rat3, COrange);
% Extra function defined elsewhere
Integral25oc_801 = integratedata(pr25_80sccm1.data(:,1), pr25oC_80rat1, COrange);
% Extra function defined elsewhere
Integral25oc_802 = integratedata(pr25_80sccm2.data(:,1), pr25oC_80rat2, COrange);
% Extra function defined elsewhere
Integral25oc_803 = integratedata(pr25_80sccm3.data(:,1), pr25oC_80rat3, COrange);
% Extra function defined elsewhere
Integral25oc_1001 = integratedata(pr25_100sccm1.data(:,1), pr25oC_100rat1, COrange);
% Extra function defined elsewhere
Integral25oc_1002 = integratedata(pr25_100sccm2.data(:,1), pr25oC_100rat2, COrange);
% Extra function defined elsewhere
Integral25oc_1003 = integratedata(pr25_100sccm3.data(:,1), pr25oC_100rat3, COrange);
% Extra function defined elsewhere
Integral25oc_1004 = integratedata(pr25_100sccm4.data(:,1), pr25oC_100rat4, COrange);
% Extra function defined elsewhere

Data25_20 = [Integral25oc_201 Integral25oc_202 Integral25oc_203]
Data25_40 = [Integral25oc_401 Integral25oc_402 Integral25oc_403]
Data25_60 = [Integral25oc_601 Integral25oc_602 Integral25oc_603]
Data25_80 = [Integral25oc_801 Integral25oc_802 Integral25oc_803]
Data25_100 = [Integral25oc_1001 Integral25oc_1002 Integral25oc_1003
Integral25oc_1004]

mean25_20 = mean(Data25_20)
mean25_40 = mean(Data25_40)
mean25_60 = mean(Data25_60)
mean25_80 = mean(Data25_80)
mean25_100 = mean(Data25_100)

std25_20 = std(Data25_20)
std25_40 = std(Data25_40)
std25_60 = std(Data25_60)
std25_80 = std(Data25_80)
std25_100 = std(Data25_100)


% 50oC FTIR data
pr50oC_20rat1 = -(log10(pr50_20sccm1.data(:,2)./background_1.data(:,2)));
% Determine absorbance
pr50oC_20rat2 = -(log10(pr50_20sccm2.data(:,2)./background_1.data(:,2)));
% Determine absorbance
```

Appendix A (Continued)

```
pr50oC_20rat3 = -(log10(pr50_20sccm3.data(:,2)./background_1.data(:,2)));
% Determine absorbance
pr50oC_20rat4 = -(log10(pr50_20sccm4.data(:,2)./background_1.data(:,2)));
% Determine absorbance
pr50oC_40rat1 = -(log10(pr50_40sccm1.data(:,2)./background_1.data(:,2)));
pr50oC_40rat2 = -(log10(pr50_40sccm2.data(:,2)./background_1.data(:,2)));
pr50oC_40rat3 = -(log10(pr50_40sccm3.data(:,2)./background_1.data(:,2)));
pr50oC_40rat4 = -(log10(pr50_40sccm4.data(:,2)./background_1.data(:,2)));
pr50oC_60rat1 = -(log10(pr50_60sccm1.data(:,2)./background_1.data(:,2)));
pr50oC_60rat2 = -(log10(pr50_60sccm2.data(:,2)./background_1.data(:,2)));
pr50oC_60rat3 = -(log10(pr50_60sccm3.data(:,2)./background_1.data(:,2)));
pr50oC_60rat4 = -(log10(pr50_60sccm4.data(:,2)./background_1.data(:,2)));
pr50oC_80rat1 = -(log10(pr50_80sccm1.data(:,2)./background_1.data(:,2)));
pr50oC_80rat2 = -(log10(pr50_80sccm2.data(:,2)./background_1.data(:,2)));
pr50oC_80rat3 = -(log10(pr50_80sccm3.data(:,2)./background_1.data(:,2)));
pr50oC_80rat4 = -(log10(pr50_80sccm4.data(:,2)./background_1.data(:,2)));
pr50oC_80rat5 = -(log10(pr50_80sccm5.data(:,2)./background_1.data(:,2)));
pr50oC_100rat1 = -(log10(pr50_100sccm1.data(:,2)./background_1.data(:,2)));
pr50oC_100rat2 = -(log10(pr50_100sccm2.data(:,2)./background_1.data(:,2)));
pr50oC_100rat3 = -(log10(pr50_100sccm3.data(:,2)./background_1.data(:,2)));
pr50oC_100rat4 = -(log10(pr50_100sccm4.data(:,2)./background_1.data(:,2)));


Integral50oc_201 = integratedata(pr50_20sccm1.data(:,1), pr50oC_20rat1, COrange);
% Extra function defined elsewhere
Integral50oc_202 = integratedata(pr50_20sccm2.data(:,1), pr50oC_20rat2, COrange);
% Extra function defined elsewhere
Integral50oc_203 = integratedata(pr50_20sccm3.data(:,1), pr50oC_20rat3, COrange);
% Extra function defined elsewhere
Integral50oc_204 = integratedata(pr50_20sccm4.data(:,1), pr50oC_20rat4, COrange);
% Extra function defined elsewhere
Integral50oc_401 = integratedata(pr50_40sccm1.data(:,1), pr50oC_40rat1, COrange);
% Extra function defined elsewhere
Integral50oc_402 = integratedata(pr50_40sccm2.data(:,1), pr50oC_40rat2, COrange);
% Extra function defined elsewhere
Integral50oc_403 = integratedata(pr50_40sccm3.data(:,1), pr50oC_40rat3, COrange);
% Extra function defined elsewhere
Integral50oc_404 = integratedata(pr50_40sccm4.data(:,1), pr50oC_40rat4, COrange);
% Extra function defined elsewhere
Integral50oc_601 = integratedata(pr50_60sccm1.data(:,1), pr50oC_60rat1, COrange);
% Extra function defined elsewhere
Integral50oc_602 = integratedata(pr50_60sccm2.data(:,1), pr50oC_60rat2, COrange);
% Extra function defined elsewhere
```

Appendix A (Continued)

```
Integral50oc_603 = integratedata(pr50_60sccm3.data(:,1), pr50oC_60rat3, COrange);
% Extra function defined elsewhere
Integral50oc_604 = integratedata(pr50_60sccm4.data(:,1), pr50oC_60rat4, COrange);
% Extra function defined elsewhere
Integral50oc_801 = integratedata(pr50_80sccm1.data(:,1), pr50oC_80rat1, COrange);
% Extra function defined elsewhere
Integral50oc_802 = integratedata(pr50_80sccm2.data(:,1), pr50oC_80rat2, COrange);
% Extra function defined elsewhere
Integral50oc_803 = integratedata(pr50_80sccm3.data(:,1), pr50oC_80rat3, COrange);
% Extra function defined elsewhere
Integral50oc_804 = integratedata(pr50_80sccm4.data(:,1), pr50oC_80rat4, COrange);
% Extra function defined elsewhere
Integral50oc_805 = integratedata(pr50_80sccm5.data(:,1), pr50oC_80rat5, COrange);
% Extra function defined elsewhere
Integral50oc_1001 = integratedata(pr50_100sccm1.data(:,1), pr50oC_100rat1, COrange);
% Extra function defined elsewhere
Integral50oc_1002 = integratedata(pr50_100sccm2.data(:,1), pr50oC_100rat2, COrange);
% Extra function defined elsewhere
Integral50oc_1003 = integratedata(pr50_100sccm3.data(:,1), pr50oC_100rat3, COrange);
% Extra function defined elsewhere
Integral50oc_1004 = integratedata(pr50_100sccm4.data(:,1), pr50oC_100rat4, COrange);
% Extra function defined elsewhere


Data50_20 = [Integral50oc_201 Integral50oc_202 Integral50oc_203 Integral50oc_204]
Data50_40 = [Integral50oc_401 Integral50oc_402 Integral50oc_403 Integral50oc_404]
Data50_60 = [Integral50oc_601 Integral50oc_602 Integral50oc_603 Integral50oc_604]
Data50_80 = [Integral50oc_802 Integral50oc_804 Integral50oc_805]
Data50_100 = [Integral50oc_1001 Integral50oc_1002 Integral50oc_1003
Integral50oc_1004]

mean50_20 = mean(Data50_20)
mean50_40 = mean(Data50_40)
mean50_60 = mean(Data50_60)
mean50_80 = mean(Data50_80)
mean50_100 = mean(Data50_100)

std50_20 = std(Data50_20)
std50_40 = std(Data50_40)
std50_60 = std(Data50_60)
std50_80 = std(Data50_80)
std50_100 = std(Data50_100)
```

Appendix A (Continued)

```
% 75oC FTIR data
pr75oC_20rat1 = -(log10(pr75_20sccm1.data(:,2)./background_1.data(:,2)));
% Determine absorbance
pr75oC_20rat2 = -(log10(pr75_20sccm2.data(:,2)./background_1.data(:,2)));
% Determine absorbance
pr75oC_20rat3 = -(log10(pr75_20sccm3.data(:,2)./background_1.data(:,2)));
% Determine absorbance
pr75oC_20rat4 = -(log10(pr75_20sccm4.data(:,2)./background_1.data(:,2)));
% Determine absorbance
pr75oC_40rat1 = -(log10(pr75_40sccm1.data(:,2)./background_1.data(:,2)));
pr75oC_40rat2 = -(log10(pr75_40sccm2.data(:,2)./background_1.data(:,2)));
pr75oC_40rat3 = -(log10(pr75_40sccm3.data(:,2)./background_1.data(:,2)));
pr75oC_40rat4 = -(log10(pr75_40sccm4.data(:,2)./background_1.data(:,2)));
pr75oC_40rat5 = -(log10(pr75_40sccm5.data(:,2)./background_1.data(:,2)));
pr75oC_60rat1 = -(log10(pr75_60sccm1.data(:,2)./background_1.data(:,2)));
pr75oC_60rat2 = -(log10(pr75_60sccm2.data(:,2)./background_1.data(:,2)));
pr75oC_60rat3 = -(log10(pr75_60sccm3.data(:,2)./background_1.data(:,2)));
pr75oC_60rat4 = -(log10(pr75_60sccm4.data(:,2)./background_1.data(:,2)));
pr75oC_80rat1 = -(log10(pr75_80sccm1.data(:,2)./background_1.data(:,2)));
pr75oC_80rat2 = -(log10(pr75_80sccm2.data(:,2)./background_1.data(:,2)));
pr75oC_80rat3 = -(log10(pr75_80sccm3.data(:,2)./background_1.data(:,2)));
pr75oC_80rat4 = -(log10(pr75_80sccm4.data(:,2)./background_1.data(:,2)));
pr75oC_80rat5 = -(log10(pr75_80sccm5.data(:,2)./background_1.data(:,2)));
pr75oC_100rat1 = -(log10(pr75_100sccm1.data(:,2)./background_1.data(:,2)));
pr75oC_100rat2 = -(log10(pr75_100sccm2.data(:,2)./background_1.data(:,2)));
pr75oC_100rat3 = -(log10(pr75_100sccm3.data(:,2)./background_1.data(:,2)));
pr75oC_100rat4 = -(log10(pr75_100sccm4.data(:,2)./background_1.data(:,2)));
pr75oC_100rat5 = -(log10(pr75_100sccm5.data(:,2)./background_1.data(:,2)));
pr75oC_100rat6 = -(log10(pr75_100sccm6.data(:,2)./background_1.data(:,2)));

Integral75oc_201 = integratedata(pr75_20sccm1.data(:,1), pr75oC_20rat1, COrange);
% Extra function defined elsewhere
Integral75oc_202 = integratedata(pr75_20sccm2.data(:,1), pr75oC_20rat2, COrange);
% Extra function defined elsewhere
Integral75oc_203 = integratedata(pr75_20sccm3.data(:,1), pr75oC_20rat3, COrange);
% Extra function defined elsewhere
Integral75oc_204 = integratedata(pr75_20sccm4.data(:,1), pr75oC_20rat4, COrange);
% Extra function defined elsewhere
Integral75oc_401 = integratedata(pr75_40sccm1.data(:,1), pr75oC_40rat1, COrange);
% Extra function defined elsewhere
Integral75oc_402 = integratedata(pr75_40sccm2.data(:,1), pr75oC_40rat2, COrange);
% Extra function defined elsewhere
```

110

Appendix A (Continued)

Integral75oc_403 = integratedata(pr75_40sccm3.data(:,1), pr75oC_40rat3, COrange);
% Extra function defined elsewhere
Integral75oc_404 = integratedata(pr75_40sccm4.data(:,1), pr75oC_40rat4, COrange);
% Extra function defined elsewhere
Integral75oc_405 = integratedata(pr75_40sccm5.data(:,1), pr75oC_40rat5, COrange);
% Extra function defined elsewhere
Integral75oc_601 = integratedata(pr75_60sccm1.data(:,1), pr75oC_60rat1, COrange);
% Extra function defined elsewhere
Integral75oc_602 = integratedata(pr75_60sccm2.data(:,1), pr75oC_60rat2, COrange);
% Extra function defined elsewhere
Integral75oc_603 = integratedata(pr75_60sccm3.data(:,1), pr75oC_60rat3, COrange);
% Extra function defined elsewhere
Integral75oc_604 = integratedata(pr75_60sccm4.data(:,1), pr75oC_60rat4, COrange);
% Extra function defined elsewhere
Integral75oc_801 = integratedata(pr75_80sccm1.data(:,1), pr75oC_80rat1, COrange);
% Extra function defined elsewhere
Integral75oc_802 = integratedata(pr75_80sccm2.data(:,1), pr75oC_80rat2, COrange);
% Extra function defined elsewhere
Integral75oc_803 = integratedata(pr75_80sccm3.data(:,1), pr75oC_80rat3, COrange);
% Extra function defined elsewhere
Integral75oc_804 = integratedata(pr75_80sccm4.data(:,1), pr75oC_80rat4, COrange);
% Extra function defined elsewhere
Integral75oc_805 = integratedata(pr75_80sccm5.data(:,1), pr75oC_80rat5, COrange);
% Extra function defined elsewhere
Integral75oc_1001 = integratedata(pr75_100sccm1.data(:,1), pr75oC_100rat1, COrange);
% Extra function defined elsewhere
Integral75oc_1002 = integratedata(pr75_100sccm2.data(:,1), pr75oC_100rat2, COrange);
% Extra function defined elsewhere
Integral75oc_1003 = integratedata(pr75_100sccm3.data(:,1), pr75oC_100rat3, COrange);
% Extra function defined elsewhere
Integral75oc_1004 = integratedata(pr75_100sccm4.data(:,1), pr75oC_100rat4, COrange);
% Extra function defined elsewhere
Integral75oc_1005 = integratedata(pr75_100sccm5.data(:,1), pr75oC_100rat5, COrange);
% Extra function defined elsewhere
Integral75oc_1006 = integratedata(pr75_100sccm6.data(:,1), pr75oC_100rat6, COrange);
% Extra function defined elsewhere

Data75_20 = [Integral75oc_201 Integral75oc_202 Integral75oc_203 Integral75oc_204]
Data75_40 = [Integral75oc_401 Integral75oc_402 Integral75oc_403 Integral75oc_404
Integral75oc_405]
Data75_60 = [Integral75oc_601 Integral75oc_602 Integral75oc_603 Integral75oc_604]
Data75_80 = [Integral75oc_801 Integral75oc_802 Integral75oc_803 Integral75oc_804
Integral75oc_805]

111

Appendix A (Continued)

Data75_100 = [Integral75oc_1001 Integral75oc_1002 Integral75oc_1003
Integral75oc_1004 Integral75oc_1005 Integral75oc_1006]

mean75_20 = mean(Data75_20)
mean75_40 = mean(Data75_40)
mean75_60 = mean(Data75_60)
mean75_80 = mean(Data75_80)
mean75_100 = mean(Data75_100)

std75_20 = std(Data75_20)
std75_40 = std(Data75_40)
std75_60 = std(Data75_60)
std75_80 = std(Data75_80)
std75_100 = std(Data75_100)

% 100oC FTIR data
pr100oC_20rat1 = -(log10(pr100_20sccm1.data(:,2)./background_1.data(:,2)));
% Determine absorbance
pr100oC_20rat2 = -(log10(pr100_20sccm2.data(:,2)./background_1.data(:,2)));
% Determine absorbance
pr100oC_20rat3 = -(log10(pr100_20sccm3.data(:,2)./background_1.data(:,2)));
% Determine absorbance
pr100oC_20rat4 = -(log10(pr100_20sccm4.data(:,2)./background_1.data(:,2)));
% Determine absorbance
pr100oC_20rat5 = -(log10(pr100_20sccm5.data(:,2)./background_1.data(:,2)));
% Determine absorbance
pr100oC_20rat6 = -(log10(pr100_20sccm6.data(:,2)./background_1.data(:,2)));
% Determine absorbance
pr100oC_40rat1 = -(log10(pr100_40sccm1.data(:,2)./background_1.data(:,2)));
pr100oC_40rat2 = -(log10(pr100_40sccm2.data(:,2)./background_1.data(:,2)));
pr100oC_40rat3 = -(log10(pr100_40sccm3.data(:,2)./background_1.data(:,2)));
pr100oC_40rat4 = -(log10(pr100_40sccm4.data(:,2)./background_1.data(:,2)));
pr100oC_40rat5 = -(log10(pr100_40sccm5.data(:,2)./background_1.data(:,2)));
pr100oC_60rat1 = -(log10(pr100_60sccm1.data(:,2)./background_1.data(:,2)));
pr100oC_60rat2 = -(log10(pr100_60sccm2.data(:,2)./background_1.data(:,2)));
pr100oC_60rat3 = -(log10(pr100_60sccm3.data(:,2)./background_1.data(:,2)));
pr100oC_60rat4 = -(log10(pr100_60sccm4.data(:,2)./background_1.data(:,2)));
pr100oC_60rat5 = -(log10(pr100_60sccm5.data(:,2)./background_1.data(:,2)));
pr100oC_60rat6 = -(log10(pr100_60sccm6.data(:,2)./background_1.data(:,2)));
pr100oC_60rat7 = -(log10(pr100_60sccm7.data(:,2)./background_1.data(:,2)));
pr100oC_80rat1 = -(log10(pr100_80sccm1.data(:,2)./background_1.data(:,2)));
pr100oC_80rat2 = -(log10(pr100_80sccm2.data(:,2)./background_1.data(:,2)));
pr100oC_80rat3 = -(log10(pr100_80sccm3.data(:,2)./background_1.data(:,2)));

Appendix A (Continued)

```
pr100oC_80rat4 = -(log10(pr100_80sccm4.data(:,2)./background_1.data(:,2)));
pr100oC_80rat5 = -(log10(pr100_80sccm5.data(:,2)./background_1.data(:,2)));
pr100oC_100rat1 = -(log10(pr100_100sccm1.data(:,2)./background_1.data(:,2)));
pr100oC_100rat2 = -(log10(pr100_100sccm2.data(:,2)./background_1.data(:,2)));
pr100oC_100rat3 = -(log10(pr100_100sccm3.data(:,2)./background_1.data(:,2)));
pr100oC_100rat4 = -(log10(pr100_100sccm4.data(:,2)./background_1.data(:,2)));
pr100oC_100rat5 = -(log10(pr100_100sccm5.data(:,2)./background_1.data(:,2)));


Integral100oc_201 = integratedata(pr100_20sccm1.data(:,1), pr100oC_20rat1, COrange);
% Extra function defined elsewhere
Integral100oc_202 = integratedata(pr100_20sccm2.data(:,1), pr100oC_20rat2, COrange);
% Extra function defined elsewhere
Integral100oc_203 = integratedata(pr100_20sccm3.data(:,1), pr100oC_20rat3, COrange);
% Extra function defined elsewhere
Integral100oc_204 = integratedata(pr100_20sccm4.data(:,1), pr100oC_20rat4, COrange);
% Extra function defined elsewhere
Integral100oc_205 = integratedata(pr100_20sccm5.data(:,1), pr100oC_20rat5, COrange);
% Extra function defined elsewhere
Integral100oc_206 = integratedata(pr100_20sccm6.data(:,1), pr100oC_20rat6, COrange);
% Extra function defined elsewhere
Integral100oc_401 = integratedata(pr100_40sccm1.data(:,1), pr100oC_40rat1, COrange);
% Extra function defined elsewhere
Integral100oc_402 = integratedata(pr100_40sccm2.data(:,1), pr100oC_40rat2, COrange);
% Extra function defined elsewhere
Integral100oc_403 = integratedata(pr100_40sccm3.data(:,1), pr100oC_40rat3, COrange);
% Extra function defined elsewhere
Integral100oc_404 = integratedata(pr100_40sccm4.data(:,1), pr100oC_40rat4, COrange);
% Extra function defined elsewhere
Integral100oc_405 = integratedata(pr100_40sccm5.data(:,1), pr100oC_40rat5, COrange);
% Extra function defined elsewhere
Integral100oc_601 = integratedata(pr100_60sccm1.data(:,1), pr100oC_60rat1, COrange);
% Extra function defined elsewhere
Integral100oc_602 = integratedata(pr100_60sccm2.data(:,1), pr100oC_60rat2, COrange);
% Extra function defined elsewhere
Integral100oc_603 = integratedata(pr100_60sccm3.data(:,1), pr100oC_60rat3, COrange);
% Extra function defined elsewhere
Integral100oc_604 = integratedata(pr100_60sccm4.data(:,1), pr100oC_60rat4, COrange);
% Extra function defined elsewhere
Integral100oc_605 = integratedata(pr100_60sccm5.data(:,1), pr100oC_60rat5, COrange);
% Extra function defined elsewhere
Integral100oc_606 = integratedata(pr100_60sccm6.data(:,1), pr100oC_60rat6, COrange);
% Extra function defined elsewhere
```

Appendix A (Continued)

```
Integral100oc_607 = integratedata(pr100_60sccm7.data(:,1), pr100oC_60rat7, COrange);
% Extra function defined elsewhere
Integral100oc_801 = integratedata(pr100_80sccm1.data(:,1), pr100oC_80rat1, COrange);
% Extra function defined elsewhere
Integral100oc_802 = integratedata(pr100_80sccm2.data(:,1), pr100oC_80rat2, COrange);
% Extra function defined elsewhere
Integral100oc_803 = integratedata(pr100_80sccm3.data(:,1), pr100oC_80rat3, COrange);
% Extra function defined elsewhere
Integral100oc_804 = integratedata(pr100_80sccm4.data(:,1), pr100oC_80rat4, COrange);
% Extra function defined elsewhere
Integral100oc_805 = integratedata(pr100_80sccm5.data(:,1), pr100oC_80rat5, COrange);
% Extra function defined elsewhere
Integral100oc_1001 = integratedata(pr100_100sccm1.data(:,1), pr100oC_100rat1,
COrange);        % Extra function defined elsewhere
Integral100oc_1002 = integratedata(pr100_100sccm2.data(:,1), pr100oC_100rat2,
COrange);        % Extra function defined elsewhere
Integral100oc_1003 = integratedata(pr100_100sccm3.data(:,1), pr100oC_100rat3,
COrange);        % Extra function defined elsewhere
Integral100oc_1004 = integratedata(pr100_100sccm4.data(:,1), pr100oC_100rat4,
COrange);        % Extra function defined elsewhere
Integral100oc_1005 = integratedata(pr100_100sccm5.data(:,1), pr100oC_100rat5,
COrange);        % Extra function defined elsewhere

Data100_20 = [Integral100oc_201 Integral100oc_202 Integral100oc_203
Integral100oc_204 Integral100oc_205 Integral100oc_206]
Data100_40 = [Integral100oc_401 Integral100oc_402 Integral100oc_403
Integral100oc_404 Integral100oc_405]
Data100_60 = [Integral100oc_601 Integral100oc_602 Integral100oc_603
Integral100oc_604 Integral100oc_605 Integral100oc_606 Integral100oc_607]
Data100_80 = [Integral100oc_801 Integral100oc_802 Integral100oc_803
Integral100oc_804 Integral100oc_805]
Data100_100 = [Integral100oc_1001 Integral100oc_1002 Integral100oc_1003
Integral100oc_1004 Integral100oc_1005]

mean100_20 = mean(Data100_20)
mean100_40 = mean(Data100_40)
mean100_60 = mean(Data100_60)
mean100_80 = mean(Data100_80)
mean100_100 = mean(Data100_100)

std100_20 = std(Data100_20)
std100_40 = std(Data100_40)
std100_60 = std(Data100_60)
```

Appendix A (Continued)

```
std100_80 = std(Data100_80)
std100_100 = std(Data100_100)

% 125oC FTIR data
pr125oC_20rat1 = -(log10(pr125_20sccm1.data(:,2)./background_1.data(:,2)));
% Determine absorbance
pr125oC_20rat2 = -(log10(pr125_20sccm2.data(:,2)./background_1.data(:,2)));
% Determine absorbance
pr125oC_20rat3 = -(log10(pr125_20sccm3.data(:,2)./background_1.data(:,2)));
% Determine absorbance
pr125oC_20rat4 = -(log10(pr125_20sccm4.data(:,2)./background_1.data(:,2)));
% Determine absorbance
pr125oC_20rat5 = -(log10(pr125_20sccm5.data(:,2)./background_1.data(:,2)));
% Determine absorbance
pr125oC_20rat6 = -(log10(pr125_20sccm6.data(:,2)./background_1.data(:,2)));
pr125oC_40rat1 = -(log10(pr125_40sccm1.data(:,2)./background_1.data(:,2)));
pr125oC_40rat2 = -(log10(pr125_40sccm2.data(:,2)./background_1.data(:,2)));
pr125oC_40rat3 = -(log10(pr125_40sccm3.data(:,2)./background_1.data(:,2)));
pr125oC_40rat4 = -(log10(pr125_40sccm4.data(:,2)./background_1.data(:,2)));
pr125oC_40rat5 = -(log10(pr125_40sccm5.data(:,2)./background_1.data(:,2)));
pr125oC_60rat1 = -(log10(pr125_60sccm1.data(:,2)./background_1.data(:,2)));
pr125oC_60rat2 = -(log10(pr125_60sccm2.data(:,2)./background_1.data(:,2)));
pr125oC_60rat3 = -(log10(pr125_60sccm3.data(:,2)./background_1.data(:,2)));
pr125oC_60rat4 = -(log10(pr125_60sccm4.data(:,2)./background_1.data(:,2)));
pr125oC_60rat5 = -(log10(pr125_60sccm5.data(:,2)./background_1.data(:,2)));
pr125oC_80rat1 = -(log10(pr125_80sccm1.data(:,2)./background_1.data(:,2)));
pr125oC_80rat2 = -(log10(pr125_80sccm2.data(:,2)./background_1.data(:,2)));
pr125oC_80rat3 = -(log10(pr125_80sccm3.data(:,2)./background_1.data(:,2)));
pr125oC_80rat4 = -(log10(pr125_80sccm4.data(:,2)./background_1.data(:,2)));
pr125oC_80rat5 = -(log10(pr125_80sccm5.data(:,2)./background_1.data(:,2)));
pr125oC_100rat1 = -(log10(pr125_100sccm1.data(:,2)./background_1.data(:,2)));
pr125oC_100rat2 = -(log10(pr125_100sccm2.data(:,2)./background_1.data(:,2)));
pr125oC_100rat3 = -(log10(pr125_100sccm3.data(:,2)./background_1.data(:,2)));
pr125oC_100rat4 = -(log10(pr125_100sccm4.data(:,2)./background_1.data(:,2)));
pr125oC_100rat5 = -(log10(pr125_100sccm5.data(:,2)./background_1.data(:,2)));
pr125oC_100rat6 = -(log10(pr125_100sccm6.data(:,2)./background_1.data(:,2)));

Integral125oc_201 = integratedata(pr125_20sccm1.data(:,1), pr125oC_20rat1, COrange);
% Extra function defined elsewhere
Integral125oc_202 = integratedata(pr125_20sccm2.data(:,1), pr125oC_20rat2, COrange);
% Extra function defined elsewhere
Integral125oc_203 = integratedata(pr125_20sccm3.data(:,1), pr125oC_20rat3, COrange);
% Extra function defined elsewhere
```

Appendix A (Continued)

```
Integral125oc_204 = integratedata(pr125_20sccm4.data(:,1), pr125oC_20rat4, COrange);
% Extra function defined elsewhere
Integral125oc_205 = integratedata(pr125_20sccm5.data(:,1), pr125oC_20rat5, COrange);
% Extra function defined elsewhere
Integral125oc_206 = integratedata(pr125_20sccm6.data(:,1), pr125oC_20rat6, COrange);
% Extra function defined elsewhere
Integral125oc_401 = integratedata(pr125_40sccm1.data(:,1), pr125oC_40rat1, COrange);
% Extra function defined elsewhere
Integral125oc_402 = integratedata(pr125_40sccm2.data(:,1), pr125oC_40rat2, COrange);
% Extra function defined elsewhere
Integral125oc_403 = integratedata(pr125_40sccm3.data(:,1), pr125oC_40rat3, COrange);
% Extra function defined elsewhere
Integral125oc_404 = integratedata(pr125_40sccm4.data(:,1), pr125oC_40rat4, COrange);
% Extra function defined elsewhere
Integral125oc_405 = integratedata(pr125_40sccm5.data(:,1), pr125oC_40rat5, COrange);
% Extra function defined elsewhere
Integral125oc_601 = integratedata(pr125_60sccm1.data(:,1), pr125oC_60rat1, COrange);
% Extra function defined elsewhere
Integral125oc_602 = integratedata(pr125_60sccm2.data(:,1), pr125oC_60rat2, COrange);
% Extra function defined elsewhere
Integral125oc_603 = integratedata(pr125_60sccm3.data(:,1), pr125oC_60rat3, COrange);
% Extra function defined elsewhere
Integral125oc_604 = integratedata(pr125_60sccm4.data(:,1), pr125oC_60rat4, COrange);
% Extra function defined elsewhere
Integral125oc_605 = integratedata(pr125_60sccm5.data(:,1), pr125oC_60rat5, COrange);
% Extra function defined elsewhere
Integral125oc_801 = integratedata(pr125_80sccm1.data(:,1), pr125oC_80rat1, COrange);
% Extra function defined elsewhere
Integral125oc_802 = integratedata(pr125_80sccm2.data(:,1), pr125oC_80rat2, COrange);
% Extra function defined elsewhere
Integral125oc_803 = integratedata(pr125_80sccm3.data(:,1), pr125oC_80rat3, COrange);
% Extra function defined elsewhere
Integral125oc_804 = integratedata(pr125_80sccm4.data(:,1), pr125oC_80rat4, COrange);
% Extra function defined elsewhere
Integral125oc_805 = integratedata(pr125_80sccm5.data(:,1), pr125oC_80rat5, COrange);
% Extra function defined elsewhere
Integral125oc_1001 = integratedata(pr125_100sccm1.data(:,1), pr125oC_100rat1,
COrange);       % Extra function defined elsewhere
Integral125oc_1002 = integratedata(pr125_100sccm2.data(:,1), pr125oC_100rat2,
COrange);       % Extra function defined elsewhere
Integral125oc_1003 = integratedata(pr125_100sccm3.data(:,1), pr125oC_100rat3,
COrange);       % Extra function defined elsewhere
```

Appendix A (Continued)

```
Integral125oc_1004 = integratedata(pr125_100sccm4.data(:,1), pr125oC_100rat4,
COrange);        % Extra function defined elsewhere
Integral125oc_1005 = integratedata(pr125_100sccm5.data(:,1), pr125oC_100rat5,
COrange);        % Extra function defined elsewhere
Integral125oc_1006 = integratedata(pr125_100sccm6.data(:,1), pr125oC_100rat6,
COrange);        % Extra function defined elsewhere


Data125_20 = [Integral125oc_201 Integral125oc_202 Integral125oc_203
Integral125oc_204 Integral125oc_205 Integral125oc_206]
Data125_40 = [Integral125oc_401 Integral125oc_402 Integral125oc_403
Integral125oc_404 Integral125oc_405]
Data125_60 = [Integral125oc_601 Integral125oc_602 Integral125oc_603
Integral125oc_604 Integral125oc_605]
Data125_80 = [Integral125oc_801 Integral125oc_802 Integral125oc_803
Integral125oc_804 Integral125oc_805]
Data125_100 = [Integral125oc_1001 Integral125oc_1002 Integral125oc_1003
Integral125oc_1004 Integral125oc_1005 Integral125oc_1006]


mean125_20 = mean(Data125_20)
mean125_40 = mean(Data125_40)
mean125_60 = mean(Data125_60)
mean125_80 = mean(Data125_80)
mean125_100 = mean(Data125_100)


std125_20 = std(Data125_20)
std125_40 = std(Data125_40)
std125_60 = std(Data125_60)
std125_80 = std(Data125_80)
std125_100 = std(Data125_100)


% Error


Error25_20 = sqrt((mean20/mean25_20^2)^2*std20^2 + (1/mean20)^2*std25_20^2)
Error25_40 = sqrt((mean40/mean25_40^2)^2*std40^2 + (1/mean40)^2*std25_40^2)
Error25_60 = sqrt((mean60/mean25_60^2)^2*std60^2 + (1/mean60)^2*std25_60^2)
Error25_80 = sqrt((mean80/mean25_80^2)^2*std80^2 + (1/mean80)^2*std25_80^2)
Error25_100 = sqrt((mean100/mean25_100^2)^2*std100^2 +
(1/mean100)^2*std25_100^2)


Error50_20 = sqrt((mean20/mean50_20^2)^2*std20^2 + (1/mean20)^2*std50_20^2)
Error50_40 = sqrt((mean40/mean50_40^2)^2*std40^2 + (1/mean40)^2*std50_40^2)
Error50_60 = sqrt((mean60/mean50_60^2)^2*std60^2 + (1/mean60)^2*std50_60^2)
Error50_80 = sqrt((mean80/mean50_80^2)^2*std80^2 + (1/mean80)^2*std50_80^2)
```

Appendix A (Continued)

Error50_100 = sqrt((mean100/mean50_100^2)^2*std100^2 +
(1/mean100)^2*std50_100^2)

Error75_20 = sqrt((mean20/mean75_20^2)^2*std20^2 + (1/mean20)^2*std75_20^2)
Error75_40 = sqrt((mean40/mean75_40^2)^2*std40^2 + (1/mean40)^2*std75_40^2)
Error75_60 = sqrt((mean60/mean75_60^2)^2*std60^2 + (1/mean60)^2*std75_60^2)
Error75_80 = sqrt((mean80/mean75_80^2)^2*std80^2 + (1/mean80)^2*std75_80^2)
Error75_100 = sqrt((mean100/mean75_100^2)^2*std100^2 +
(1/mean100)^2*std75_100^2)

Error100_20 = sqrt((mean20/mean100_20^2)^2*std20^2 + (1/mean20)^2*std100_20^2)
Error100_40 = sqrt((mean40/mean100_40^2)^2*std40^2 + (1/mean40)^2*std100_40^2)
Error100_60 = sqrt((mean60/mean100_60^2)^2*std60^2 + (1/mean60)^2*std100_60^2)
Error100_80 = sqrt((mean80/mean100_80^2)^2*std80^2 + (1/mean80)^2*std100_80^2)
Error100_100 = sqrt((mean100/mean100_100^2)^2*std100^2 +
(1/mean100)^2*std100_100^2)

Error125_20 = sqrt((mean20/mean125_20^2)^2*std20^2 + (1/mean20)^2*std125_20^2)
Error125_40 = sqrt((mean40/mean125_40^2)^2*std40^2 + (1/mean40)^2*std125_40^2)
Error125_60 = sqrt((mean60/mean125_60^2)^2*std60^2 + (1/mean60)^2*std125_60^2)
Error125_80 = sqrt((mean80/mean125_80^2)^2*std80^2 + (1/mean80)^2*std125_80^2)
Error125_100 = sqrt((mean100/mean125_100^2)^2*std100^2 +
(1/mean100)^2*std125_100^2)

ABOUT THE AUTHOR

Benjamin Alan Grayson, a native of Mize, MS, was valedictorian of his 1995 high school graduating class. He began his undergraduate education at Jones County Junior College in Ellisville, MS before transferring to Mississippi State University to finish his B.S. in chemical engineering in May, 2000. Benjamin received his M.S.Ch.E. from the University of South Florida in December, 2002. He continued at USF to finish his Ph.D. in August, 2007.